Radio Emission from Cosmic Ray Air Showers

Dissertation

zur

Erlangung des Doktorgrades (Dr. rer. nat.)

der

Mathematisch-Naturwissenschaftlichen Fakultät

der

Rheinischen Friedrich-Wilhelms-Universität Bonn

vorgelegt von

Tim Huege

aus

Solingen

Bonn 2004

Angefertigt mit Genehmigung der Mathematisch-Naturwissenschaftlichen
Fakultät der Rheinischen Friedrich-Wilhelms-Universität Bonn

1. Referent: Prof. Dr. Heino Falcke
2. Referent: Prof. Dr. Peter Schneider

Tag der Promotion: 14.12.2004

Diese Dissertation ist auf dem Hochschulschriftenserver der ULB Bonn
http://hss.ulb.uni-bonn.de/diss_online elektronisch publiziert.

Summary

Charged particles with energies ranging from a few times 10^6 eV up to $\gtrsim 10^{20}$ eV continuously impinge on the earth as so-called "cosmic rays". Their study constitutes an important field of research in both astronomy and particle physics, and some cosmic ray related effects even have significance for the public's every-day life.

Radio emission from cosmic ray air showers offers the opportunity to use radio observations as an additional powerful observing technique in cosmic ray research, thereby building a bridge between astroparticle physics and radio astronomy. As a necessary prerequisite, a detailed theoretical analysis of the processes responsible for the radio emission has to be performed. In this thesis, we analyse the emission in the scheme of "coherent geosynchrotron radiation" emitted by electron-positron pairs created in the air shower cascade as they are deflected in the earth's magnetic field.

We first perform an analytic calculation of the emission based on realistic parametrisations of the particle distributions in the air shower. The analytic approach allows us to gain a solid understanding of general emission features and the coherence effects arising from the different physical scales present in the air shower. We compare our predictions with the available historical data and find that geosynchrotron radiation can indeed explain the emission.

Afterwards, we conceive and implement a sophisticated Monte Carlo code, performing the calculation with increased precision and taking into account a more realistic air shower model. We describe and test the concepts envisaged to allow a high-precision modelling of realistic air showers on standard computer hardware and compare the Monte Carlo results with the analytic calculations to ensure the correctness of our modelling efforts.

In a last step, we use our Monte Carlo code to simulate a large number of air showers in order to study the effect of important air shower parameters and geometries on the associated radio emission. Our main result is a parametrisation formula relating the radio emission characteristics directly to important air shower and observer parameters such as the air shower geometry, the primary particle energy, the depth of the shower maximum, the observer distance from the shower centre, and the observing frequency.

With this analysis, we build the foundation for the interpretation of experimental measurements of radio emission from extensive air showers and thus make a great step forward in the establishment of radio observations as an additional observing technique in cosmic ray research.

Contents

1

Introduction

Cosmic ray air showers have been known for almost 40 years to emit pulsed radio emission in the frequency range from a few to a few hundred MHz, an effect that offers great opportunities for the study of extensive air showers with upcoming fully digital “software radio telescopes” such as LOFAR and the enhancement of particle detector arrays such as KASCADE-Grande or the Pierre Auger Observatory. However, there are still a lot of open questions regarding the strength of the emission as well as the underlying emission mechanism.

Only with a detailed theoretical analysis of the processes leading to the emission, current and future experimental efforts such as the LOPES project can make use of their full potential. In this thesis, we build the necessary theoretical foundation for the use of radio emission from cosmic ray air showers as a powerful observing technique in cosmic ray research by modelling the radio emission from extensive air showers within the scenario of “coherent geosynchrotron radiation”.

To motivate the interest in this additional observing technique, which is largely complementary to the well-established particle detector and air fluorescence techniques, we first give a very short (and by no means complete) introduction into the field of cosmic ray physics in general before providing a quick overview over the merits of the radio technique as well as the historical and current activities in the field.

1.1 Cosmic Rays

The fact that energetic particle radiation continuously impinges on the earth was first discovered by Hess (1912) using an electrometer during balloon flights. He discovered that the rate with which a static charge on the electrometer diminishes grows as a function of increasing height and inferred that there had to be ionising radiation coming from space. In 1936, Viktor Hess was awarded the Nobel Prize for the discovery of these so-called "cosmic rays" (CRs).

Cosmic rays mainly consist of protons and ionised nuclei and constitute an important astronomical window. At the same time, the interaction processes they undergo fall into the realm of particle physics. Consequently, cosmic rays form one of the important links between the two fields and indeed are at the centre of "astroparticle physics". Interestingly, although cosmic ray research has been going on for almost 100 years now, many fundamental questions such as that of the nature of the CR sources are still unanswered.

Even the public is confronted with cosmic ray-related phenomena in their every-day life — a significant fraction of the natural radioactivity on earth is caused by the fragments of cosmic ray induced extensive air showers. Particle bursts from the sun can knock out important communication infrastructure. And some scientists even claim to have found evidence for a direct link between the cosmic ray flux reaching the earth and the global climate (Shaviv 2004).

To appreciate the importance of cosmic ray physics, we give a quick introduction in the following sections.

1.1.1 Observing techniques

Cosmic rays span many orders of magnitude in energy, from "low energies" of $\sim$ MeV up to "ultra-high energies" of $\sim 3 \times 10^{20}$ eV (Bird et al. 1995).

Particles at energies below $\sim 10^{14}$ eV can be measured directly with particle detectors mounted on balloons or satellites. Direct measurement of the primary particles allows detailed analyses, e.g. of the individual particles' energies, their chemical composition, and other properties.

Above this energy threshold, the particle fluxes become very low and a direct measurement with balloon or satellite-experiments is no longer economically feasible, as the effective collecting area is too low. Particles at these energies, however, can initiate so-called "extensive air showers" in the atmosphere (cf. section 1.1.2). The fragments of these air showers arrive at ground-level

and can be measured with ground-based particle detector arrays. One such experiment for the energy range of 5×10^{14}–2×10^{17} eV is the KASCADE experiment at the Forschungszentrum Karlsruhe in Germany, which has now been incorporated into KASCADE-Grande. Another example is the Akeno Giant Air Shower Array (AGASA) in Japan (The AGASA collaboration 2004), aimed at ultra-high-energy cosmic rays with energies up to $\gtrsim 10^{20}$ eV. While these ground-based arrays have the advantage of huge effective collecting areas and are thus able to measure even very low cosmic ray fluxes, the information gathered on the primary particles is of only very indirect nature. Reconstruction of the primary particles' energies, let alone their composition, is a very difficult process requiring state of the art computer simulations of the particle physics in the air shower development itself — at energies far beyond the regime that can be experimentally tested with particle accelerator experiments.

At yet higher energies of $\gtrsim 10^{18}$ eV, another technique for the observation of cosmic rays becomes important: the measurement of fluorescence light in the optical to ultra-violet emitted by atmospheric nitrogen molecules that were excited during the passage of the air shower. These fluorescence measurements have the advantage of yielding very direct information about the deposition of energy in the atmosphere and can therefore better reconstruct, e.g., the energy and composition of the primary particles. The main drawback of this technique, however, is that it can only be used in very good observing conditions, i.e., in clear, moonless nights far away from man-made light pollution. The overall duty cycle therefore is usually only around 10%. Additionally, this technique requires elaborate modelling of the atmospheric conditions. The most prominent example for this technique is the "High Resolution Fly's Eye" (HiRes) experiment in Utah, USA (see, e.g., Sokolsky 2003). Currently, this technique is adapted for satellite-based monitoring of large fractions of the earth's atmosphere. One such experiment is the EUSO instrument, planned to be mounted on the International Space Station ISS (Catalano et al. 2003).

The two techniques yield very much complementary information and a combination into a "hybrid" approach bears many advantages. Consequently, (the southern part of) the Pierre Auger Observatory (e.g., Matthews & Pierre Auger Observatory Collaboration 2004) currently being set up in the Pampa Amarilla in Argentina will combine a huge array of particle detectors (1600 covering an area of 3100 km^2) with 24 optical telescopes for fluorescence measurements in stereoscopic configuration. The Pierre Auger Observatory will provide the best statistics so far for ultra-high energy cosmic rays (UHECRs) $\gtrsim 10^{19}$ eV and will therefore provide the necessary information to address

some of the most important questions regarding UHECRs (cf. 1.1.4).

The radio technique bears many of the advantages of the fluorescence technique, e.g. a more direct and "integral" nature of the air shower measurements, but has the additional attractive ability to work 24 hours a day, seven days a week in almost any environment (Falcke & Gorham 2003). It is therefore much less demanding regarding the observing site. Additionally, a design such as that of the LOFAR-based LOPES experiment (Horneffer et al. 2004) will allow setups with a moderate cost per antenna.

1.1.2 Cosmic ray induced air showers

Auger et al. (1939) discovered that high-energy cosmic rays can initiate "extensive air showers" (EAS) in the atmosphere. After having traversed an energy- and composition-dependent atmospheric depth, the primary particle interacts with a nucleus in the atmosphere and initiates a cascade of particle reactions producing secondary particles which themselves initiate further sub-cascades. The overall cascade propagates through the atmosphere with almost the (vacuum) speed of light as it evolves to a maximum in particle number and then diminishes again. A fact important for the coherence of the radio emission is that the shower remains concentrated in a thin "pancake" of only a few metres thickness. The lateral extent of the pancake is mostly due to multiple scattering of the particles and varies for the different components in the air shower: muonic (about 5% of the particles), electromagnetic (electrons, positrons and photons, about 90% of the particles) and hadronic (pions, kaons, protons, neutrons and fragments of nuclei, about 1% of the particles). The cascade fragments arriving at the ground can then be measured by particle detector arrays with great effective collecting areas (cf. section 1.1.1). Figure 1.1 gives a schematic view of an extensive air shower.

To reconstruct information about the primary particle from the fragments measured on the ground, elaborate Monte Carlo simulation codes such as CORSIKA (Heck et al. 1998) are necessary. As these simulations use particle physics models operating in energy regimes far beyond the range experimentally tested with particle accelerators, considerable uncertainty remains. Also, shower-to-shower fluctuations make it very difficult to infer information about the primary particle of an individual air shower. Fluorescence measurements have an advantage in this respect as they can measure the energy deposit in different atmospheric depths directly and derive information about the energy and composition of the primary particle energy from the position and extent of the so-called "shower maximum".

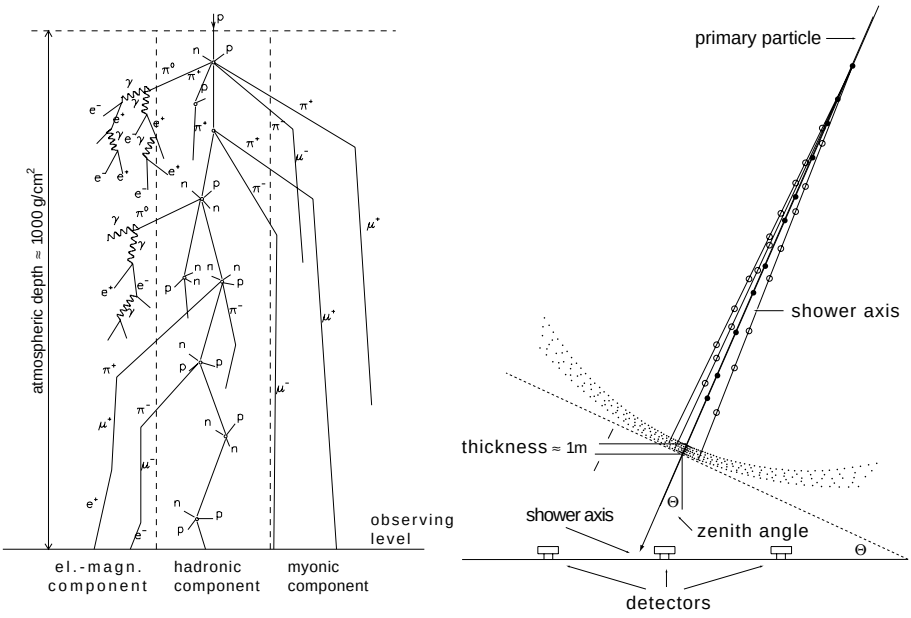

FIGURE 1.1—Schematic view of an extensive air shower (Alkhofer 1975).

For a modelling of the radio emission from cosmic ray air showers, detailed information about the distribution of electrons and positrons in the air shower is necessary.

1.1.3 Cosmic ray measurements

In the following, we present a (very minor) fraction of the most interesting measurements regarding cosmic rays.

As mentioned earlier, the spectrum of cosmic rays spans many orders of magnitude. Figure 1.2 shows a tentative differential spectrum of the cosmic ray flux from energies of $\sim 10^{11}$ eV up to $\gtrsim 10^{20}$ eV as contributed by direct as well as indirect measurements. The spectrum very closely follows a power-law of index ~ -2.75 over many decades. It, however, also shows some interesting features, the most prominent being the so-called "knee" around 3×10^{15} eV and the so-called "ankle" near 5×10^{18}–10^{19} eV. The origin of these features is the subject of ongoing scientific discussion, and we present some of the most popular theories in section 1.1.4.

From the direct measurements on satellites and balloons, the composition

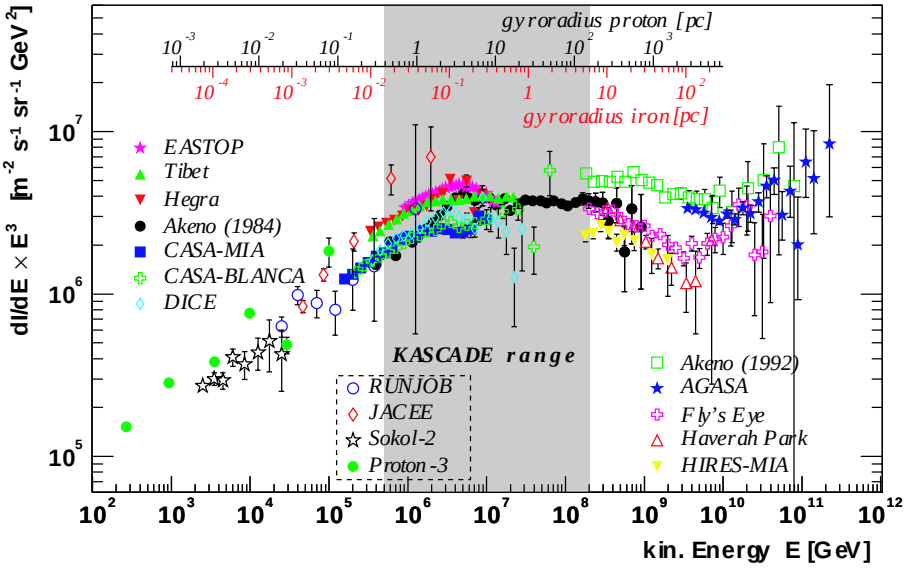

FIGURE 1.2—Spectrum of the cosmic ray flux, adapted from Maier (2003), for references to the underlying data see Ulrich (2003). To enhance the features visible in the spectrum, the flux has been multiplied by E^3. The gyration radii have been calculated for an interstellar magnetic field of 1.4 μG.

of cosmic rays at energies up to $\sim 10^{14}$ eV (i.e., of Galactic origin, cf. section 1.1.4) is known relatively well. It is very similar to the composition of elements in the solar system (cf. Fig. 1.3) with some deviations. The increased abundances for Li, Be and B as well as Sc to Mn in the CRs with regard to the solar system, e.g., can be explained by spallation of CNO and Fe cosmic rays.

Much attention is currently focused on the ultra-high energy cosmic rays. Specifically, their absolute flux is rather unclear to date. The theoretically motivated "GZK cutoff" (see section 1.1.4) predicts a diminishing of the cosmic ray flux at energies above $\sim 5 \times 10^{19}$ eV. While the HiRes data indeed seem to indicate a flux depression in this energy regime, the AGASA data show a continuation of the spectrum up to energies of $> 10^{20}$ eV, as shown in Fig. 1.4. The statistics, however, are far too bad at these energies to really decide whether there is a flux depression or not (at energies above 10^{20} eV, the estimated flux is of order one particle per km^2 per century). The Pierre Auger Observatory with its huge effective collecting area will, however, finally provide the necessary statistics to address this issue very soon.

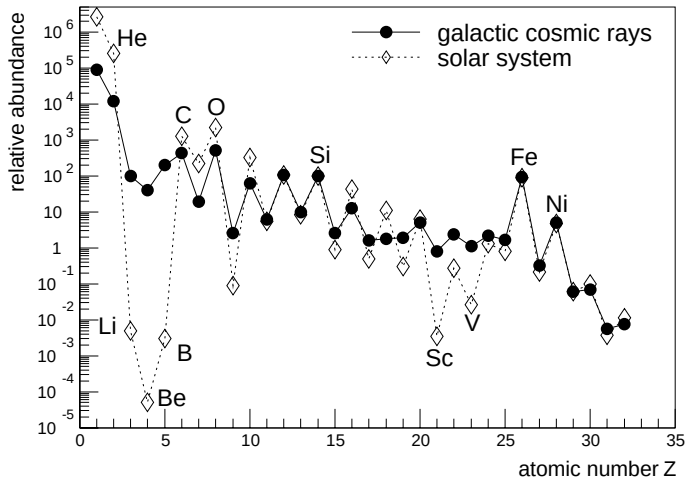

FIGURE 1.3—Composition of Galactic cosmic rays in comparison with element composition in the solar system (Wefel 1991). The abundances are normalised to 100 for Si.

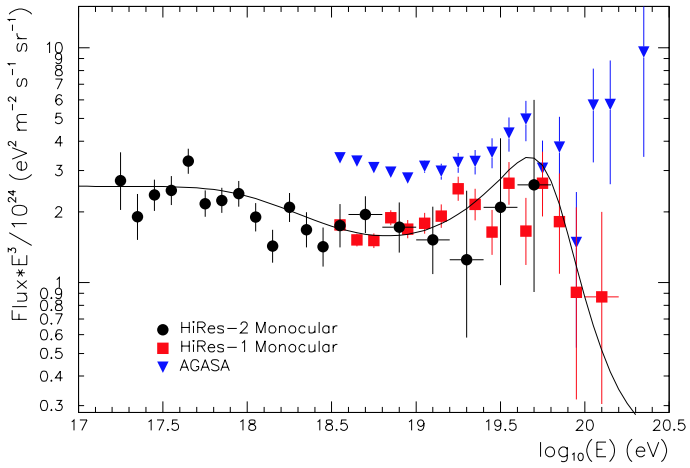

FIGURE 1.4—HiRes data versus AGASA data (Bergman, D.R. for the High Resolution Fly's Eye Collaboration 2003). The fi t to the HiRes spectra is done by a two-component model taking into account the GZK effect.

Another feature in the UHECR measurements that is subject to much debate is the presumed small-scale anisotropy of the arrival directions of UHE-

CRs (Takeda et al. 1999) (whereas the large-scale distribution is remarkably isotropic). There seem to be prominent doublets and triplets of cosmic ray events arriving from specific directions. These could point back to individual cosmic ray sources — but then again, the underlying propagation models for cosmic rays in the magnetic fields of the Galaxy themselves are very uncertain. At the highest energies, however, the cosmic rays could indeed point back directly to their sources, as the gyration radii in the cosmic magnetic fields become very large (cf. Fig. 1.2). One could therefore even do classical astronomy with these highest-energy particles. The main issue regarding the anisotropy models to date are, however, again the insufficient statistics available so far.

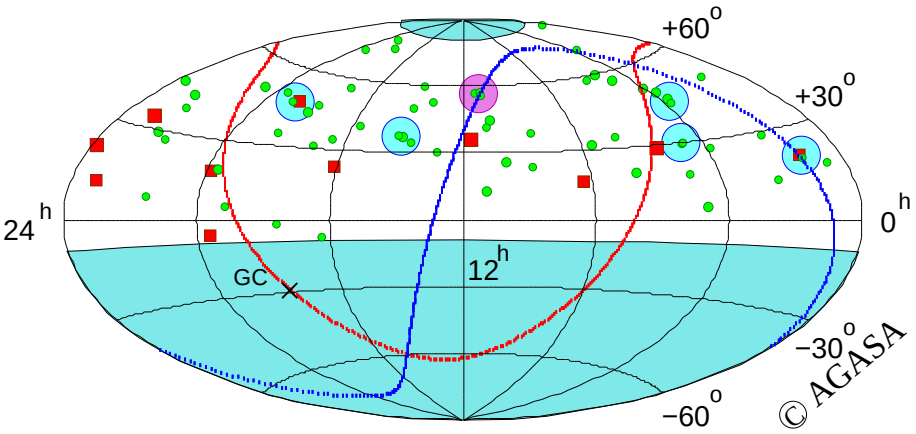

FIGURE 1.5—Anisotropy above 4×10^{19} eV as presented by The AGASA collaboration (2004). Red squares and green circles represent cosmic rays with energies of $> 10^{20}$ eV, and (4–10) $\times10^{19}$ eV, respectively. Epoch: Akeno 20 km^2 from Feb. 17, 1990 to Jul. 31, 2002. Zenith Angles: $< 45°$. Shaded circles indicate event clustering within 2.5°.

1.1.4 Cosmic ray sources

The sources of cosmic rays are still under much scientific debate. One can, however, identify different regimes in the cosmic ray spectrum: Particles with energies as low as MeV are of solar origin, and up to energies of $\sim 10^{10}$ eV, the particle flux is strongly modulated by the solar activity. At higher energies, the sources are presumed to be of Galactic origin, whereas at energies $\gtrsim 10^{18}$ eV the particles are no longer confined to the Galaxy by magnetic fields and a transition to an extragalactic cosmic ray component is suspected.

The "classic" theory proposes acceleration of charged particles through diffusive shocks in astronomical sources as the origin of cosmic rays (Fermi 1949). One of the most attractive scenarios is acceleration in shock fronts of supernova remnants (e.g., Lagage & Cesarsky 1983). It has recently gotten strong support by direct observation of high-energy photons originating from supernova remnant shells by the HESS γ-ray telescope (Aharonian et al. 2004). A number of models involve pulsars (e.g., Harding & Gaisser 1990), some of them proposing a direct particle acceleration in strong electromagnetic fields (Cheng et al. 1986).

Most of these models can explain the cosmic ray flux up to energies of $\sim 10^{15}$–10^{17} eV. This energy regime encompasses the "knee" feature visible in the spectrum at energies of $\sim 3\times 10^{15}$ eV. Although this feature was already discovered by Kulikov & Khristiansen (1959) over 40 years ago, its origin is not fully understood to date. Since it carries information about the possible sources of the cosmic rays, many theoretical works concentrate on its interpretation. One general class of models proposes the knee feature as the superposition of components differently accelerated in the source (e.g., Lagage & Cesarsky 1983), whereas other models explain the spectral changes as a consequence of diffusion effects during the cosmic ray propagation in the Galaxy (e.g., Ptuskin et al. 1993). Erlykin & Wolfendale (1987) propose a single nearby supernova-remnant as the origin of the knee feature. Furthermore, there is a whole class of "exotic" models postulating new particles or changed interaction properties, explaining the knee, e.g., by changes in the development of the extensive air showers rather than the cosmic ray flux itself (Nikolsky 1995). Recent results of the KASCADE experiment (Ulrich 2003; Kampert et al. 2004) favour the classes of models predicting a rigidity (momentum per unit charge) dependent scaling of the knee energy position, i.e., the models based on acceleration effects at the source or diffusion/drift effects during propagation in the Galaxy.

Special research effort is currently focused on the UHECRs. The apparent flux of cosmic rays with energies beyond the so-called "GZK cutoff" visible in the AGASA data (cf. section 1.1.3) constitutes a mystery. The prediction of this cutoff (which is actually not a hard flux cutoff but rather a flux suppression at the highest energies, the details of which critically depend on the underlying source distribution and particle propagation models) goes back to Greisen (1966) and Zatsepin & Kuzmin (1966): At energies $\gtrsim 5\times 10^{19}$ eV, protons can produce pions in interactions with the cosmic microwave background photons. This effectively limits the path length of UHECRs to $\lesssim$ 100 Mpc (Sigl et al. 1994). Although there are models for acceleration of particles to such high en-

ergies in “classical” astrophysical sources, e.g., in jets of active galactic nuclei (Biermann & Strittmatter 1987; Rachen & Biermann 1993), the nature of the potential UHECR sources remains unclear as there are no obvious candidate sources in the distance range permitted by the GZK cutoff (Elbert & Sommers 1995).

To circumvent the difficulties in explaining the presence of UHECRs at energies beyond the GZK cutoff by astronomical sources, a number of more “exotic” models have been envisaged. Contrary to the “bottom-up” scenario of astronomical sources accelerating the charged particles to ultra-high energies, these “top-down” models explain the UHECRs as decay products of supermassive “X” particles, which themselves are either emitted by topological defects such as magnetic monopoles created in the early universe or may have been created directly in the early universe and survived until today (for an overview see Sigl 2003). An important signature of these processes would be a specific ratio of cosmic rays to neutrinos as well as TeV γ-rays. We thus make a very short excursion to the closely related neutrino astronomy experiments.

1.1.5 Neutrino astronomy

Depending on their origin, the UHECR particles must be accompanied by certain fluxes of high-energy neutrinos and γ-rays. (We do not discuss the latter here for the sake of conciseness.) A measurement of the neutrino component could thus directly differentiate between the various models, specifically the top-down and bottom-up scenarios. Additionally, neutrinos can be used for direct astronomical observations, because they are uncharged and therefore not deflected in cosmic magnetic fields.

These are, among others, important motivations for many of the experiments trying to measure high-energy neutrinos. The main challenge in these experiments is a detection in spite of the extremely low cross-section for interaction of neutrinos with matter. Consequently, one needs gigantic detection volumes as provided, e.g., by the antarctic ice. The AMANDA experiment (e.g., Halzen 1999) at the south-pole uses photo-multipliers on strings deposited in the antarctic ice to look for electromagnetic showers and Čerenkov light from the leptons produced by neutrino-induced charged current reactions. Other experiments such as ANTARES (ANTARES collaboration 1999) and Baikal (Balkanov et al. 1999) use water as the detection volume.

One experiment very closely related to the measurement of radio emission from cosmic ray air showers is the RICE project (Kravchenko et al. 2003) also situated at the AMANDA site in the antarctic. Its goal is to measure ra-

dio Čerenkov radiation produced by electromagnetic cascades in the dense ice arising from the Askaryan-effect (cf. section 1.2.5). The RICE experiment is therefore the dense media equivalent to the experiments measuring radio emission from cosmic ray air showers. A related approach is the measurement of radio emission from the moon arising from neutrino-induced electromagnetic showers in the lunar regolith (Falcke & Gorham 2003).

In case of horizontal air showers, one can even use the atmosphere as detection volume for neutrinos. Huge air shower experiments such as the Pierre Auger Observatory can therefore also be used to put limits on the high-energy neutrino flux.

1.2 Radio emission from cosmic ray air showers

The initial discovery of pulsed radio emission accompanying extensive air showers was made in the mid-1960ies and triggered intensive research both on the experimental and the theoretical side. In the late 1970ies, however, these activities almost ceased completely due to ongoing problems with the interpretation of the experimental data, technical problems and also the great success of the alternative observing techniques.

Today, renewed interest in radio emission from cosmic ray air showers as an additional observing technique for cosmic ray research has arisen. In the following sections we provide a short overview over the historical as well as recent developments and motivate why this field currently experiences its renaissance. For a more detailed account of the history of radio emission from cosmic ray air showers, we refer the interested reader to the excellent review of Allan (1971).

1.2.1 Motivation

Radio measurements of EAS open an entirely new window for the observation of cosmic rays. The technique has a number of significant benefits. Similar to the optical fluorescence technique, it allows a much more direct view into the air shower cascade than particle measurements on the ground, yielding information greatly simplifying the reconstruction of air shower parameters from particle measurements. The fluorescence technique is able to measure the development of the air shower as it evolves. The radio technique, on the other hand, mainly measures quantities integrated over the full evolution of the air shower. (The radio signal thus correlates well with the muon number measured by particle detector arrays, as almost all muons generated in the

shower cascade reach ground-level.) A major benefit of the radio technique is that it is not hindered by the need for superb observing conditions (clear, dark, moonless nights far away from any light pollution) that limits the duty cycle of optical fluorescence detectors to typically less than 10%. For a purely radio-triggered array with a low number of antennas, radio detection of EAS should be feasible for energies $\gtrsim 10^{17}$ eV. With large arrays such as LOFAR or in combination with external triggering by particle detector arrays such as KASCADE-Grande (Antoni et al. 2003) or the Pierre Auger Observatory (The Pierre Auger Collaboration 1996), the study of EAS ranging from $\sim 10^{15}$ eV up to ultra-high energies would be possible (Falcke & Gorham 2003). Consequently, an instrumentation with radio antennas is part of the long-term goals for the northern hemisphere extension of the Pierre Auger Observatory.

To establish radio observations of cosmic ray air showers as an additional observing technique, two important prerequisites have to be fulfilled: First, an experiment has to demonstrate the feasibility and reliability of measuring radio emission from cosmic ray air showers in today's environment of high radio-frequency interference. Second, we need a good theoretical understanding of the underlying emission mechanisms and a detailed model of the dependences of the radio emission on the underlying air shower parameters. The former is one of the goals of the LOPES project (cf. section 1.2.4), while the work presented here addresses the latter question in the framework of the "coherent geosynchrotron emission" approach first proposed by Falcke & Gorham (2003).

1.2.2 Historical experiments

In the mid-1960s, Jelley et al. (1965) discovered that extensive air showers (EAS) initiated by high-energy cosmic rays produce strongly pulsed radio emission at frequencies around 44 MHz. Their measurements were motivated by the theoretical predictions of Askaryan (Askaryan 1962, 1965). The discovery triggered intensive research, and in the following years a number of experiments established the presence of radio emission from EAS over the frequency-range from a few to a few hundred MHz (see Prah 1971 for a very detailed overview).

The nature of these experiments was simplistic, yet effective. In the early Haverah Park installation, e.g., as little as two antennas per frequency and polarisation direction with a receiver system of only a few MHz bandwidth were connected to oscilloscopes continuously measuring the radio signals. The Haverah Park particle detector array provided a trigger once an air shower

was registered, causing a still camera to photograph the pulses visible on the oscilloscopes (Prah 1971). Such simplistic experiments would no longer be possible today, as the radio frequency interference has grown by orders of magnitude (in the 1960ies, e.g., the British broadcasting service BBC stopped its TV transmissions during the nights).

A number of experiments (see, e.g., Allan et al. 1967, 1969; Sun 1975) soon demonstrated that there is a dependence of the radio emission's polarisation on the geomagnetic field, giving emission models postulating a dominance of the geomagnetic emission mechanism additional weight.

Although a number of independent groups all measured the radio pulses, a major problem remained: The absolute emission level was very uncertain and remains unclear even today. While earlier Haverah Park experiments found emission strengths of order $\epsilon_\nu \sim 10\ \mu\mathrm{V\ m^{-1}\ MHz^{-1}}$ (Allan et al. 1971), consecutive works reported values of $\epsilon_\nu \sim 1\ \mu\mathrm{V\ m^{-1}\ MHz^{-1}}$ or even lower (Allan et al. 1973, 1975). Other groups inferred yet different absolute strengths (e.g., Atrashkevich et al. 1975). Some of these discrepancies could be explained by systematic deviations in the primary particle energy calibration used at that time. More probably, however, the calibration of the radio receiving systems themselves is responsible for the discrepancies, especially in case of the differences between the different groups (Atrashkevich et al. 1978). Another problem associated to the historical data is the sometimes insufficient documentation of details regarding the measured quantities, air shower selection criteria, and other experimental parameters.

While little doubt remains that radio emission from cosmic ray air showers has actually been measured in the past, the data on its strength and properties are still very scarce and uncertain. It is therefore imperative to gather reliable, well-calibrated data with a new generation of experiments.

1.2.3 Recent and current experimental efforts

Lately, interest in the measurement of radio emission from cosmic ray air showers has awakened once again. A major driver of this interest have been the recent advances in digital signal processing. In particular, the advent of digital radio-interferometers such as LOFAR with their capability to simultaneously monitor the full sky for transient radio signals promise an effective study of the radio emission even in today's environments of high radio-frequency interference. The development of a **LO**FAR **p**rototyp**e** **s**tation for the dedicated measurement of extensive air showers consequently constitutes the goal of the LOPES project described in section 1.2.4. Apart from the LOPES project,

there have been a few other experimental efforts in the recent past.

Green et al. (2003) posted an individual antenna near the CASA/MIA array in Utah (USA). Their setup, however, was limited by high levels of radio-frequency interference and was not able to measure radio pulses associated with cosmic ray air showers. As an upper limit for the emission strength they found $\epsilon_\nu = 31\text{–}34\ \mu\text{V m}^{-1}\ \text{MHz}^{-1}$.

An ongoing effort is the CODALEMA experiment situated in Nançay, France (Belletoile et al. 2004). This experiment uses the radio-astronomical Decametric Array (DAM) in the frequency range from 1–100 MHz in conjunction with high-speed digital oscilloscopes trying to detect radio pulses in coincidence between multiple antennas. While the CODALEMA experiment has the advantage of being situated in an extremely radio-quiet environment with very little radio-frequency interference, it does (at the moment) not have any independent information on the arrival of cosmic ray air showers. Furthermore, as the experiment only measures one circular polarisation component of the emission, statistics of the radio pulses alone cannot be used to infer if the measured radio pulses actually originate from air showers, as will be demonstrated in the course of this work from the predicted radio emission properties. The CODALEMA experiment is currently being equipped with particle detectors which will allow to relate the radio pulses to individual air showers. As the experiment is based on highly sophisticated, expensive, oscilloscope technology, it will, however, be very difficult to scale this concept up to great numbers of antennas for application in giant air shower arrays such as the Pierre Auger Observatory.

1.2.4 The LOPES project

The aim of the LOPES project (Horneffer et al. 2004) is to develop an experiment measuring radio emission from cosmic ray air showers in the framework of the digital radio-interferometer LOFAR. LOFAR, originally conceived as a pure radio-astronomical instrument for the low-frequency domain of 10–200 MHz (e.g., Röttgering et al. 2003), provides an ideal basis for observation of radio emission from extensive air showers as proposed by Falcke & Gorham (2003). On the one hand, it provides full sky coverage as with a "low-gain" antenna design. On the other hand, its signal processing capabilities allow a very efficient noise reduction as in a "high-gain" antenna design through digital beam-forming, and additionally facilitate the digital filtering of radio-frequency interference. The fully digital processing including temporary buffering of the measured radio signals makes it particularly suitable for the

otherwise difficult detection of transient events such as the pulses associated to air showers. The development of LOPES in the framework of LOFAR allows the use of many of the LOFAR designs for antennas, readout-electronics, and other components. As LOFAR itself will consist of tens of thousands of individual antennas, one of its major design goals is a low cost per antenna. Consequently, the experience gathered in the development of the LOPES project will be invaluable for the planned equipment of giant air shower arrays such as the Pierre Auger Observatory with radio capabilities.

The LOPES experiment currently consists of 30 antennas working as a phased array in conjunction with the particle detector array KASCADE-Grande situated at the Forschungszentrum Karlsruhe in Germany. While this environment suffers from high levels of radio-frequency interference — especially from the photo-multipliers of the KASCADE particle detectors themselves (Horneffer et al. 2004) —, operation in conjunction with a particle detector array allows an unambiguous matching of radio signals and air shower events. This is a fundamental necessity for the study of the radio signal properties as a function of the air shower parameters, especially in the current phase of uncertain knowledge of the radio emission's absolute strength.

LOPES has the capability to measure linearly polarised emission, which is especially useful for the verification of geomagnetic deflection of charged particles as the dominant emission mechanism. The experiment has been taking quality data since January 2004 and has so far found several dozen radio pulses that are unambiguously associated to cosmic ray air showers (Horneffer, private communication).

1.2.5 Historical theory

In the early 1960ies, Askaryan (1962; 1965) had already predicted the emission of radio Čerenkov radiation from electromagnetic cascades in particle showers. The underlying mechanism is the build-up of a net negative charge excess in the electromagnetic cascade which then propagates in the ambient medium at a velocity faster than the corresponding speed of light. These predictions were one of the motivations for the initial experiments by Jelley et al. (1965).

After the experimental proof for the existence of the radio pulses was made, a number of authors started working on the theoretical interpretation of the emission process. Kahn & Lerche (1966) developed an analytical model taking into account the charge excess as well as geomagnetic emission mechanisms. They found that the emission was dominated by a geomagnetic effect which they described as a continuous charge separation induced by the earth's

magnetic field leading to transverse currents propagating through the atmosphere. However, the air shower model at the basis of their calculations was severely over-simplified. A number of follow-up works tried to improve on the Kahn & Lerche model by incorporating more realistic air shower models. Castagnoli et al. (1969) developed an early Monte Carlo simulation of the emission in the Kahn & Lerche framework, whereas Fuji & Nishimura (1969) improved the description of the electromagnetic shower through the use of cascade equations. Other attempts to calculate the radio emission were made by Colgate (1967) and Allan (as described in Allan 1971).

All these works predicted the geomagnetic mechanism to dominate the radio emission. (The Askaryan-type charge-excess mechanism, however, still plays a major role in dense media such as ice and is used e.g. in the RICE experiment (cf. section 1.1.5) to measure neutrino-induced electromagnetic showers in ice. It has also been experimentally verified by Saltzberg et al. (2001) who directly measured the radio emission from electromagnetic cascades in a sand target.)

A major achievement of the historical works was the establishment of the geomagnetic emission as the dominant source of radio emission from cosmic ray air showers. None of the historical models, however, reached a level of sophistication allowing a detailed comparison of theoretical results to experimental data from concrete experiments such as LOPES. While Kahn & Lerche (1966), e.g., used extremely over-simplified air shower geometries, Castagnoli et al. (1969) only modelled air showers up to energies of 10^{14} eV and the treatment of Allan (1971) overall remained on a somewhat qualitative, phenomenological level.

Having reached only a limited understanding of the emission mechanism responsible for the radio emission to date, it is clear that any experimental effort for the observation of radio emission from cosmic rays must be accompanied by thorough theoretical modelling of the associated emission mechanism. As many of the details regarding the historical models have never been published, taking a fresh approach to this modelling effort seems most promising.

1.2.6 Recent theoretical works

Stimulated by the ideas presented in Falcke & Gorham (2003) and the renewed experimental activities, a number of authors have recently published theoretical works on the topic of radio emission from cosmic ray air showers. Apart from the modelling efforts presented in this thesis, there have been two other attempts at making predictions about the properties of the radio emission.

Suprun et al. (2003) have calculated the emission from the shower maximum of a vertical air shower in the geosynchrotron radiation scenario with Monte Carlo techniques. A drawback of this work, however, is its missing integration over the air shower evolution as a whole.

Gousset et al. (2004) have made some qualitative geometrical calculations to show that inclined air showers produce a much larger radio emission pattern on the ground than vertical showers due to the strongly increased spatial distance of the shower maximum from the ground.

None of these publications, however, draw a detailed picture of the radio emission and its dependence on the underlying air shower parameters.

1.2.7 This work

A detailed modelling of the radio emission from cosmic ray air showers as a function of the underlying air shower characteristics is the goal of this work. It is specifically aimed at providing a theoretical foundation for the interpretation of the experimental data collected by the LOPES project.

Since many of the historical experimental and theoretical results point to a geomagnetic process as the dominant emission mechanism for radio emission from cosmic ray air showers, we concentrate our effort on this effect. We take the new approach of "coherent geosynchrotron radiation" as proposed by Falcke & Gorham (2003), which we feel is an elegant and intuitive description of the underlying processes. It perceives the radiation as synchrotron pulses from highly relativistic electron-positron pairs gyrating in the earth's magnetic field. Radiation emitted at low frequencies is expected to be coherent, as the emission wavelength is larger than the extent of the air shower "pancake" (e.g., 30 metres wavelength vs. a few metres pancake thickness at 10 MHz). Other mechanisms such as the Askaryan-type Čerenkov emission can then be included in our model at a later time. We develop our model in a number of separate steps:

In chapter 2, published as Huege & Falcke (2003), we perform an analytic calculation of the geosynchrotron emission from a vertical air shower. The air shower properties are modelled realistically with analytic parametrisations of the important characteristics such as the lateral and longitudinal particle distributions, the particle energy distribution and the air shower evolution as a function of atmospheric depth. The emission from the individual particles itself is modelled with well-known synchrotron theory. While a number of necessary approximations limit its accuracy, this analytic analysis provides us with a solid understanding of the important coherence effects shaping the emission.

With this fundamental understanding of the relevant effects we conceive and implement a detailed Monte Carlo simulation of the air shower emission. To retain comparability with the analytic calculations, we model the air shower properties themselves with the same analytic parametrisations as in the analytic calculations. The individual particle emission, however, is calculated without the use of any approximations, retaining the full polarisation information. Chapter 3, published as Huege & Falcke (2004a), describes the detailed strategies used in the Monte Carlo approach and demonstrates the consistency and robustness of the simulations. It finishes with a direct comparison of the Monte Carlo and analytic results for a vertical air shower.

Having demonstrated the correctness of the Monte Carlo calculations, we use our Monte Carlo code for an elaborate analysis of the emission's dependence on specific air shower parameters in chapter 4, to be published as Huege & Falcke (2004b). We achieve this goal by performing detailed simulations of air showers with various configurations as well as geometries and analysing the corresponding emission characteristics. To facilitate the comparison of our simulation results with experimental data, we then parametrise the inferred dependences into a simple overall formula describing the dependences of the emission on the main air shower parameters.

The conclusions given in chapter 5 then summarise the achievements of our modelling efforts so far and give an outlook on the future evolution of our emission model.

2

Analytic Calculations

2.1 Introduction

In this chapter, we perform an analytical analysis of radio emission from cosmic ray air showers based on the new approach of interpreting the emission process as coherent synchrotron emission from electron-positron pairs deflected in the earth's magnetic field ("coherent geosynchrotron radiation"), as proposed by Falcke & Gorham (2003); see also Huege & Falcke (2002). Other than Suprun et al. (2003), who recently simulated geosynchrotron emission from EAS with Monte Carlo techniques, we pursue an analytical approach to get a solid understanding of the effects governing the emission. The development of a sophisticated Monte Carlo code will then be the second step in our modelling efforts.

We describe the basis of our approach in some detail in Sec. 2.2 and derive some observationally relevant quantities in Section 2.3. Sec. 2.4 summarises the characteristics of the air shower development that are needed for a realistic modelling of the emission process. In Sec. 2.5–2.8 we develop our model for the radio emission from EAS step by step with increasingly realistic geometries, which helps in understanding the coherence effects that play a role in shaping the emission spectrum and spatial distribution. After a short discussion of the results in Sec. 2.9 we conclude our work in Section 2.10.

2.2 The geosynchrotron approach

Two main emission mechanisms have been proposed in the past for radio emission from EAS: Čerenkov radiation from a charge excess moving with a ve-

locity higher than the speed of light in the traversed medium (the so-called "Askaryan" mechanism motivated by Askaryan 1962; Askaryan 1965) and acceleration of charged particles in the earth's magnetic field. While the former is dominant in case of dense media (Buniy & Ralston 2002; Zas et al. 1992; Alvarez-Muñiz et al. 2000), polarisation measurements in a number of experiments subsequently supported the dominance of the geomagnetic emission mechanism for radio emission from EAS in air (e.g., Allan et al. 1967, 1969). It also seems unavoidable in principle for highly relativistic charged particles moving in the earth's magnetic field.

Coherent geosynchrotron emission from highly relativistic electron-positron pairs gyrating in the earth's magnetic field represents an equivalent scenario to that of the transverse currents of Kahn & Lerche (1966) (and other geomagnetic mechanisms) but is particularly appealing because it has the advantage of being based on well-studied and well-understood synchrotron theory, an excellent starting point for the development of our emission model. In the case of radio emission from cosmic ray air showers, however, coherence effects as well as non-periodic trajectories that are usually not considered for synchrotron radiation have to be taken into account.

In order to assess the coherence effects arising from the intrinsic air shower structure, we first analyse the emission from a specific point during the air shower evolution, namely the point of maximum shower development. Only in the last step we integrate over the shower evolution as a whole, which is effectively "compressed" into the radio pulse that the observer receives since the particles have velocities $v \approx c$.

At this stage, we do not take into account the Askaryan-type Čerenkov radiation. In other words, we set the refractive index of the atmosphere to unity.

2.2.1 Synchrotron-theory: individual particles

We base our calculations on the formalism developed in Jackson (1975). Any acceleration of a charge gives rise to electromagnetic radiation. The emission due to acceleration in the direction of the instantaneous velocity vector is, however, insignificant compared to that caused by the perpendicular acceleration (Jackson 1975). As a consequence, any arbitrary particle motion, including the helical motion of a charged particle in a homogeneous magnetic field, can be approximated as an instantaneous circular trajectory with adequate curvature radius.

Retardation effects caused by the finite speed of light give rise to strong

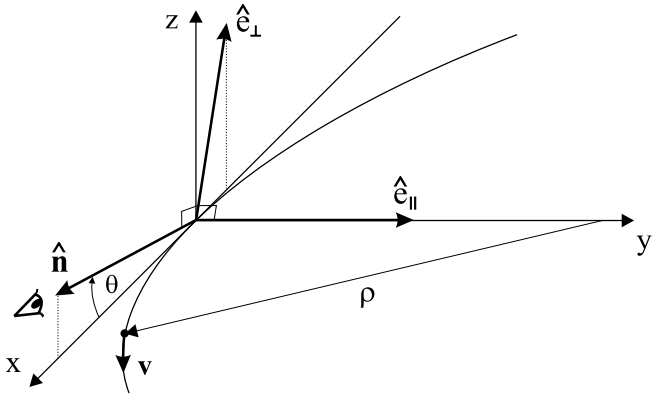

FIGURE 2.1—Geometry of single particle synchrotron radiation for an observer with line-of-sight vector $\hat{\boldsymbol{n}}$ enclosing a minimum angle θ to the instantaneous particle velocity vector $\boldsymbol{v}$. The equivalent curvature radius is given by ρ, and the emission can be conveniently divided into the components $\hat{\boldsymbol{e}}_\perp$ and $\hat{\boldsymbol{e}}_\parallel$. The particle trajectory lies in the x-y plane.

beaming effects for highly relativistic particles. For particles with Lorentz factor γ the original dipole emission pattern is beamed into a narrow emission cone of order γ^{-1} semi-opening angle which sweeps over the observer in a very short time, leading to strongly pulsed emission dominated by frequency components significantly higher than the particle gyration frequency.

The geometry of the problem corresponds to Fig. 2.1 if one chooses the origin of the coordinate system to lie in the point on the particle trajectory where the angle between instantaneous particle velocity vector $\boldsymbol{v}$ and line of sight vector $\hat{\boldsymbol{n}}$ reaches its minimum θ.

Calculation in the frequency domain circumvents problems arising from the retardation effects. Jackson defines the quantity $\boldsymbol{A}(\boldsymbol{R},\omega)$ as a measure of the frequency component ω of the electric field normalised to unit solid angle Ω. In the far-field limit (distance R to the observer large compared to the extent of the particle trajectory, i.e. use of Fraunhofer-approximation is possible), $\boldsymbol{A}(\boldsymbol{R},\omega)$ can be approximated and conveniently divided into the two perpendicular components $\hat{\boldsymbol{e}}_\perp$ and $\hat{\boldsymbol{e}}_\parallel$ defined in Figure 2.1. Retaining the phase information, $\boldsymbol{A}(\boldsymbol{R},\omega)$ can then be written as

$$\boldsymbol{A}(\boldsymbol{R},\omega) = \frac{\omega e}{\sqrt{8}c\pi} e^{i(\omega\frac{R}{c}-\frac{\pi}{2})} \left[-\hat{\boldsymbol{e}}_\parallel A_\parallel(\omega) \pm \hat{\boldsymbol{e}}_\perp A_\perp(\omega)\right], \tag{2.1}$$

where the plus-sign is to be used for electrons and the minus-sign for positrons, e denoting their unit charge. Furthermore

$$A_{\parallel}(\omega) = \mathrm{i}\frac{2\rho}{\sqrt{3}c}\left(\frac{1}{\gamma^2}+\theta^2\right)K_{2/3}(\xi), \tag{2.2}$$

$$A_{\perp}(\omega) = \theta\frac{2\rho}{\sqrt{3}c}\left(\frac{1}{\gamma^2}+\theta^2\right)^{1/2}K_{1/3}(\xi) \tag{2.3}$$

with

$$\xi = \frac{\omega\rho}{3c}\left(\frac{1}{\gamma^2}+\theta^2\right)^{3/2}, \tag{2.4}$$

where $\omega = 2\pi\nu$ denotes the angular frequency corresponding to the observing frequency ν, K_a denotes the modified Bessel-function of order a, and the curvature radius of the instantaneous circular orbit is given by

$$\rho = \frac{v\gamma m_e c}{eB\sin\alpha} \tag{2.5}$$

with magnetic field strength B and pitch angle α between the particle trajectory and the magnetic field direction.

Apart from the adopted far-field approximations, the derivation of this result incorporates an integration over a highly oscillatory integrand only part of which contributes significantly. This integration is usually conducted using the so-called “method of steepest descents” also known as “method of stationary phase” (Watson 1944). Jackson’s derivation, although somewhat simplified, is correct as long as the observing frequency ω is high compared to the gyration frequency of the particles in the magnetic field. As the latter is around a few kHz and we are only interested in observing frequencies > 10 MHz, the Jackson result is well suited as the basis for our calculations. It also correctly takes into account that the observer sees only one flash of radiation from each particle and not the periodic repetition that is associated with synchrotron radiation in the classical sense, since the mean free path length of the particles of ~ 450 m (at a height of 4 km) is very small compared with the length of a full gyration cycle of ~ 20 km.

The energy spectrum per unit solid angle of a single gyrating particle, correspondingly, is given by (Jackson 1975)

$$\frac{\mathrm{d}^2 I}{\mathrm{d}\omega\mathrm{d}\Omega} = 2\,|\boldsymbol{A}(\boldsymbol{R},\omega)|^2 = \frac{e^2}{3\pi^2 c}\left(\frac{\omega\rho}{c}\right)^2\left(\frac{1}{\gamma^2}+\theta^2\right)^2$$

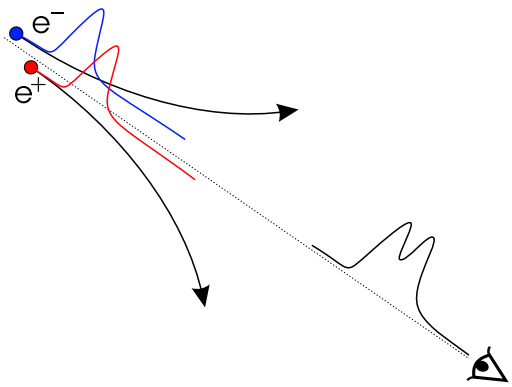

FIGURE 2.2—Misalignment between the electron and the positron in an electron-positron pair no longer allows coherent addition of the individual emissions.

$$\times \left[K_{2/3}^2(\xi) + \frac{\theta^2}{\gamma^{-2} + \theta^2} K_{1/3}^2(\xi) \right]. \tag{2.6}$$

Since the energy spectrum is $\propto |\boldsymbol{A}(\boldsymbol{R}, \omega)|^2$ it grows as N^2 with particle number N if one assumes fully coherent emission. Given a specific distance to the observer R the frequency component of the E-field can be calculated as

$$\boldsymbol{E}(\boldsymbol{R}, \omega) = \left(\frac{4\pi}{c} \right)^{1/2} \frac{1}{R} \, \boldsymbol{A}(\boldsymbol{R}, \omega). \tag{2.7}$$

For a given (observer-frame) distribution of gyrating particles, the corresponding $\boldsymbol{E}(\boldsymbol{R}, \omega)$ can then be superposed to calculate the total emission.

2.2.2 Synchrotron-theory: electron-positron pairs

In the air shower, electrons and positrons are created in pairs. The symmetry arising from the opposite curvature of electron and positron trajectories can lead to a significant simplification of the calculation: For an electron-positron pair with *perfectly* symmetric trajectories with regard to the observer, the $A_{\parallel}$ contributions from the two particles add up to $2A_{\parallel}$, whereas the $A_{\perp}$ contributions completely cancel each other.

This is, however, an overly special case which does not adequately represent the problem we are facing. Depending on the direction from which the

observer sees the particle pair, the cancellation of the $A_\perp$ contributions as well as the summation of the $A_\parallel$ contributions are only partial. Furthermore, as the pulses emitted by the relativistic particles are very short, there is an inherent coherence length associated to the emissions of the individual particles. If there is considerable misalignment between the particles, the resulting phase differences destroy the coherence as illustrated in Figure 2.2. Overall, one would therefore have to quantify the coherence losses and incomplete summation/cancellation arising from the pairing through a form factor.

A more detailed look at the numbers and characteristics of the particle distributions in the shower, however, reveals that we may indeed assume full summation and cancellation of $A_\parallel$ and $A_\perp$ for an "effective" electron-positron pair without introducing too large an error. This approximation works well if we no longer look at electron-positron pairs that actually form together but rather group pairs of positrons and electrons together such that their trajectories overlap symmetrically as seen by the observer — and if we can accomplish this pairing for the vast majority of particles.

For coherent addition of the positron and electron emission to be possible, a significant portion of those parts of the particle trajectories from which the observer actually receives radiation must overlap. (That part has a length of ~ 110 m for $\gamma = 60$, given by the length over which the instantaneous velocity vector encloses an angle $\lesssim \gamma$ with the observer's line of sight.) In a typical 10^{17} eV air shower the shower "pancake", even somewhat before and after the shower's maximum development, consists of $\sim 10^8$ particles at any time. Even if the particles were distributed homogeneously in the shower pancake, this would lead to a particle density of ~ 1000 m^{-3}. For the realistic distributions described in section 2.4, the densities in the dominating centre region are a lot higher. This illustrates that each particle (except in the unimportant outskirts of the shower pancake) will a priori have a high number of particles in its direct vicinity with which it can be paired. The probability that there is a significant overlap between the paired particles' trajectories is high because the particles' mean free path length of ~ 450 m is considerably larger than the aforementioned ~ 110 m of the trajectory from which the observer receives radiation.

Whether a consequent pairing with *symmetric trajectories* is possible, however, depends critically on the direction distribution of the particles' instantaneous velocity vectors. Throughout this work we assume a δ-distribution of the particle velocity directions at any given point in the shower shell, as we choose the initial velocity vectors to point radially away from the spherical

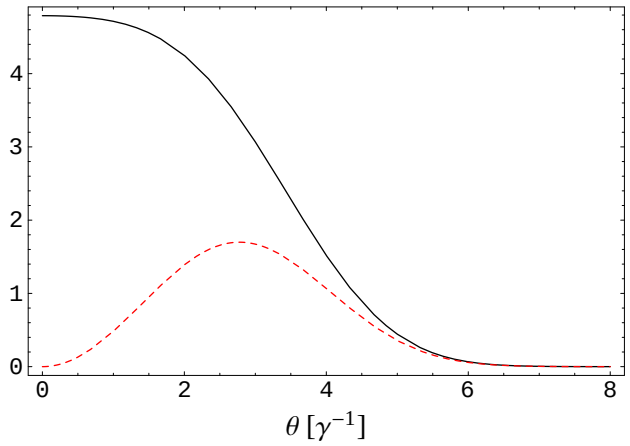

FIGURE 2.3—Comparison of $|A_{\parallel}|$ (solid) and $|A_{\perp}|$ (short-dashed) for $\nu = 100$ MHz, $\gamma = 60$ and $B = 0.3$ G. Absolute scale is arbitrary.

shower surface. In this situation, the pairing of particles with symmetric trajectories becomes simple as long as one allows pairing between positrons and electrons from generations of particles with a certain net offset in generation time.

In this scenario of high particle density and δ-distribution of velocity directions, the emission from an "effective" electron-positron pair can therefore be approximated as that from a pair with perfectly symmetric trajectories:

$$\boldsymbol{E}_{\mathrm{p}}(\boldsymbol{R},\omega) \approx \left(\frac{4\pi}{c}\right)^{1/2} \frac{1}{R}\, \frac{2\omega e}{\sqrt{8c\pi}} \mathrm{e}^{\mathrm{i}(\omega\frac{R}{c}-\frac{\pi}{2})}\, (-\hat{\boldsymbol{e}}_{\parallel})\, A_{\parallel}(\omega). \tag{2.8}$$

The fact that $|A_{\parallel}| > |A_{\perp}|$, especially for small θ where most of the radiation is emitted (Fig. 2.3), furthermore demonstrates that $A_{\perp}$ is not dominating the emission, anyway, and therefore gives further confidence in the approximation.

Effectively, this result allows us to drop the differentiation between positrons and electrons and to consider only generic "particles" hereafter. The spectrum emitted by such an individual particle then corresponds to:

$$\boldsymbol{E}(\boldsymbol{R},\omega) = \left(\frac{4\pi}{c}\right)^{1/2} \frac{1}{R}\, \frac{\omega e}{\sqrt{8c\pi}} \mathrm{e}^{\mathrm{i}(\omega\frac{R}{c}-\frac{\pi}{2})}\, (-\hat{\boldsymbol{e}}_{\parallel})\, A_{\parallel}(\omega). \tag{2.9}$$

Superposition of these spectra for all particles in the shower, correctly taking

into account the phase differences arising from their relative positions, then yields the emission from the air shower as a whole.

2.3 Observational quantities

We present a number of relations of the previous results to observational quantities:

2.3.1 Pulse reconstruction

The time-dependence of the electromagnetic pulse corresponding to a given spectrum $\boldsymbol{E}(\boldsymbol{R}, \omega)$ can easily be reconstructed for a specific receiver bandwidth by an inverse Fourier-transform of the remaining spectrum. Hence, if the frequency characteristic of the receiver is given by $b(\omega)$, the time-dependence of the electric field $\boldsymbol{E}(\boldsymbol{R}, t)$ can be calculated as

$$\boldsymbol{E}(\boldsymbol{R}, t) = \frac{1}{\sqrt{2\pi}} \int_{-\infty}^{\infty} b(\omega) \boldsymbol{E}(\boldsymbol{R}, \omega)\, \mathrm{e}^{-\mathrm{i}\omega t}\, \mathrm{d}\omega, \tag{2.10}$$

where $\boldsymbol{E}(\boldsymbol{R}, -\omega)$ is given by the complex conjugate of $\boldsymbol{E}(\boldsymbol{R}, \omega)$.

2.3.2 Conversion of $|\boldsymbol{E}(\boldsymbol{R}, \omega)|$ to ϵ_ν

In the works of the 1960ies and 1970ies, the strength of the measured radio emission was usually denoted with a quantity ϵ_ν in units of $\mu\mathrm{V\ m^{-1}\ MHz^{-1}}$, which was defined as the peak electric field strength during the pulse divided by the effective bandwidth of the receiver system $\Delta\nu$. In practice, the total pulse amplitude (in V) at a given observing frequency ν was derived from the photographed oscilloscope traces of the two polarisation directions and then converted to an electric field strength (in V/m) taking into account the receiver and antenna gain. This field strength, representing the projection of the electric field vector on the horizontal plane, was then "back-projected" to yield the field strength in the plane perpendicular to the shower axis and the magnetic field, in which the electric field vector lies (see Eq. (2.55) for $\vartheta = 0$). Division of the resulting field strength by the effective bandwidth $\Delta\nu$ of the receiver system then yielded ϵ_ν.

To compare our theoretical values of $|\boldsymbol{E}(\boldsymbol{R}, \omega)|$ to the experimental results for ϵ_ν, we analytically reconstruct the time-dependence of the electromagnetic field pulse $\boldsymbol{E}(t)$ for the case of an idealised rectangle filter of bandwidth $\Delta\nu$, over which $|\boldsymbol{E}(\boldsymbol{R}, \omega)|$ is assumed to be constant, and which is centred on the

observing frequency ν. After time-averaging over the high-frequency oscillations, ϵ_ν then directly follows from the peak field amplitude divided by $\Delta\nu$ and is given by

$$\epsilon_\nu = \sqrt{\frac{128}{\pi}}\,|\boldsymbol{E}(\boldsymbol{R},\omega)| \approx 6.4\,|\boldsymbol{E}(\boldsymbol{R},\omega)|\,. \tag{2.11}$$

2.3.3 LOPES signal-to-noise

In order to compare our predictions to the abilities of LOPES (or any other generic dipole array), we first estimate the expected signal-to-noise ratio (SNR) for a receiving system consisting of an individual inverted V shape dipole antenna with gain $G = 1.9$ and a receiver incorporating a filter with bandwidth $\Delta\nu$ centred on the observing frequency ν, a square-law detector (i.e., a detector measuring the received power) and an integrator which averages the signal over a time τ.

The noise level of the receiving system, in our case dominated by Galactic noise, can be characterised by the noise temperature $T_{\rm sys} \approx T_{\rm sky}(\nu)$. Comparison with the temperature increase ΔT corresponding to the power of the pulse intercepted by the antenna then yields

$$\mathrm{SNR} = \sqrt{2\,\Delta\nu\,\tau}\,\frac{\Delta T}{T_{\rm sys}}, \tag{2.12}$$

where the first factor takes into account the increase of the SNR due to the number of independent samples accumulated in case of bandwidth $\Delta\nu$ and averaging time τ as determined by the Nyquist theorem. The energy flux of an electromagnetic wave propagating through the (vacuum-like) atmosphere is given by the Poynting vector, *in SI-units* and omitting the argument $\boldsymbol{R}$ for the fields being defined as

$$\boldsymbol{S}(t) = \boldsymbol{E}(t) \times \boldsymbol{H}(t) = \frac{1}{\mu_0}\boldsymbol{E}(t) \times \boldsymbol{B}(t), \tag{2.13}$$

where $\mu_0 = 4\pi\ 10^{-7}$ Vs/Am. As $\boldsymbol{E} \perp \boldsymbol{B}$, it follows that

$$|\boldsymbol{S}(t)| = \frac{1}{c\mu_0}\,|\boldsymbol{E}(t)|^2 \approx \frac{1}{120\pi\,\Omega}\,|\boldsymbol{E}(t)|^2\,. \tag{2.14}$$

For a point-like source, the effective area of a dipole antenna is given by (Rohlfs & Wilson 1996) $A_{\rm eff} = G\lambda^2/4\pi = Gc^2/4\pi\nu^2$, so that it receives the

power

$$P(t) = \frac{1}{2} A_{\mathrm{eff}} \, |\boldsymbol{S}(t)| = \frac{Gc}{8\pi\nu^2\mu_0} \, |\boldsymbol{E}(t)|^2 \,, \tag{2.15}$$

where the factor 1/2 is introduced for an antenna measuring only one polarisation direction of unpolarised radiation. Averaging over the time τ then leads to

$$\begin{aligned} <P>_\tau &= \frac{Gc}{8\pi\nu^2\mu_0\tau} \int_0^\tau |\boldsymbol{E}(t)|^2 \, \mathrm{d}t \\ &\approx \frac{Gc}{8\pi\nu^2\mu_0\tau} \int_{\omega_l}^{\omega_h} \left|\boldsymbol{E}(\omega')\right|^2 \, \mathrm{d}\omega', \end{aligned} \tag{2.16}$$

where $\omega_{h/l} = 2\pi(\nu \pm 1/2\Delta\nu)$ and the last step follows from Parseval's theorem as long as the bulk of the pulse is sampled in the averaging time τ. Assuming that the spectrum is flat over the observing bandwidth $\Delta\nu$ with a value $|\boldsymbol{E}(\omega')| \equiv |\boldsymbol{E}(2\pi\nu)| = \text{const.}$ and using Eq. (2.11), we can write

$$\begin{aligned} <P>_\tau &\approx \frac{Gc}{8\pi\nu^2\mu_0\tau} \, |\boldsymbol{E}(2\pi\nu)|^2 \, 2\pi\Delta\nu \\ &= \frac{Gc}{4\nu^2\mu_0\tau} \frac{\pi}{128} \epsilon_\nu^2 \Delta\nu. \end{aligned} \tag{2.17}$$

This averaged power is then directly related to ΔT via the Boltzmann-constant k_B by

$$\Delta T = \frac{<P>_\tau}{k_\mathrm{B}\Delta\nu}, \tag{2.18}$$

so that from Eq. (2.12) follows

$$\mathrm{SNR} \approx \frac{\pi Gc}{256 \, \sqrt{2} \, \nu^2\mu_0 k_\mathrm{B}} \sqrt{\frac{\Delta\nu}{\tau}} \frac{|\epsilon_\nu|^2}{T_\mathrm{sys}}. \tag{2.19}$$

Setting τ to a sensible value of $2\Delta\nu^{-1}$, we get

$$\begin{aligned} \mathrm{SNR} &\approx 0.5 \left(\frac{G}{1.9}\right) \left(\frac{\nu}{60\ \mathrm{MHz}}\right)^{-2} \left(\frac{T_\mathrm{sky}(\nu)}{4000\ \mathrm{K}}\right)^{-1} \\ &\times \left(\frac{\Delta\nu}{35\ \mathrm{MHz}}\right) \left(\frac{\epsilon_\nu}{1\ \mu\mathrm{V\ m^{-1}\ MHz^{-1}}}\right)^2 \end{aligned} \tag{2.20}$$

for a typical LOPES antenna with an observing bandwidth of 35 MHz cen-

tred on the observing frequency 60 MHz and an estimate of $T_{\mathrm{sky}}(60\ \mathrm{MHz}) \approx 4,000$ K (Falcke & Gorham 2003).

For a complete LOPES array consisting of N_{ant} antennas, the SNR is then increased by an additional factor $\sqrt{1/2 N_{\mathrm{ant}}(N_{\mathrm{ant}}-1)} \approx \sqrt{1/2} N_{\mathrm{ant}}$ for large N_{ant}.

2.4 Extensive air shower properties

Extensive air showers can be initiated by primary particles with strongly differing energy and composition and at variable inclination angles. Consequently, their properties such as the position of their maximum development and the longitudinal and lateral distributions of secondary particles can vary significantly.

Additionally, the simulation of air showers consisting of $> 10^8$ particles with energies in the MeV range created in a cascade initiated by primary particles of energies as high as 10^{20} eV, is in itself a very difficult process. There are elaborate Monte Carlo simulations such as CORSIKA (Heck et al. 1998) and AIRES (Sciutto 1999) which themselves incorporate a number of different models for the underlying particle interactions. But although these codes are very sophisticated, uncertainties remain, especially at the very highest energies that are out of the reach of accelerator experiments (see, e.g., Knapp et al. 2003).

At this stage, however, we do not incorporate the results of elaborate air shower simulations. We rather revert to the widely used analytical parametrisations for the longitudinal development and lateral particle distributions dating back to Greisen (1956), Kamata & Nishimura (1958) and Greisen (1960) which are admittedly crude, but as a first step seem adequate to describe the properties relevant to our calculations that an "average" air shower would have in case of vertical inclination. (For an overview see, e.g., Gaisser 1990.)

2.4.1 Longitudinal air shower development

The longitudinal air shower development can be parametrised by the so-called "shower age" s as a function of atmospheric depth X:

$$s(X) = \frac{3X/X_0}{(X/X_0) + 2\ln(E_{\mathrm{p}}/E_{\mathrm{crit}})} = \frac{3X}{X + 2X_{\mathrm{m}}} \tag{2.21}$$

where $X_0 = 36.7$ g cm^{-2} denotes the electron "radiation length" in air, $E_{\mathrm{crit}} = 86$ MeV corresponds to the threshold energy where ionisation losses

equal radiation losses for electrons moving in air, and $X_\mathrm{m} = X_0 \ln(E_\mathrm{p}/E_\mathrm{crit})$ marks the theoretical value for the depth of the shower maximum in this parametrisation. The shower commences at $s = 0$, builds to its maximum development at $s = 1$ and then declines over the range $s = 1$–3. Although originally developed for purely electromagnetic showers, the formula is suitable to qualitatively describe the average development of the "clumpier" hadronic showers as well. The theoretical X_m value does then, however, not correspond to the actual position of the shower maximum. For purely electromagnetic showers, the development of the total number of charged particles (almost purely electrons and positrons) can be described by

$$N(s) = \frac{0.31 \exp\left[(X/X_0)(1 - \frac{3}{2}\ln s)\right]}{\sqrt{\ln(E_\mathrm{p}/E_\mathrm{crit})}} \tag{2.22}$$

as a function of shower age. The predicted value for N in the shower maximum ($s = 1$) is very close to the Allan (1971) "rule of thumb" $N_\mathrm{max} = E_\mathrm{p}/\mathrm{GeV} = 10^8$ for a 10^{17} eV shower. For the position of the shower maximum X_max we refer to the measurements and simulations presented in Knapp et al. (2003) that suggest a value of $X_\mathrm{max} \approx 630$ g cm^{-2} which corresponds to $R_0 \approx 4$ km for a 10^{17} eV air shower and to the works of Pryke (2001) as well as Abu-Zayyad et al. (2001).

2.4.2 Lateral particle distribution

The lateral particle density can be described with the NKG (Nishimura-Kamata-Greisen) parametrisation, which without normalisation corresponds to

$$\begin{aligned} \rho_\mathrm{NKG}(r) &= \frac{1}{r_\mathrm{M}^2} \frac{\Gamma(4.5 - s)}{2\pi\Gamma(s)\Gamma(4.5 - 2s)} \\ &\times \left(\frac{r}{r_\mathrm{M}}\right)^{s-2} \left(1 + \frac{r}{r_\mathrm{M}}\right)^{s-4.5} . \end{aligned} \tag{2.23}$$

To avoid the unphysical singularity of the NKG profile at the shower centre we cut off the distribution with a constant value at radii smaller than 0.1 m. The normalisation for the integration is chosen correspondingly (see Sec. 2.6.3).

The parameters relevant to the NKG distribution, shower age s and Molière radius r_M, show a high degree of degeneracy. The increase in s during the

shower propagation broadens the lateral distribution, but at the same time the decrease of r_M with increasing atmospheric density tends to narrow it. One can therefore often parametrise a given lateral particle distribution with a wide range of different values for s and r_M, where r_M in fact need not be close to the theoretical Molière radius at all (Antoni et al. 2001). We here stick to the theoretically motivated values of $s = 1$ for the shower maximum and set r_M to the Molière radius at the atmospheric height of the maximum derived from the atmospheric density as (Dova et al. 2003)

$$r_\mathrm{M}(h) = r_\mathrm{M}(h_0)\frac{\rho_\mathrm{atm}(h_0)}{\rho_\mathrm{atm}(h)} = 9.6\ \frac{\mathrm{g\ cm^{-2}}}{\rho_\mathrm{atm}(h)}. \tag{2.24}$$

According to the US standard atmosphere of 1977 as implemented in CORSIKA (Ulrich 1997) the atmospheric density at a height of 4 km corresponds to $\rho_\mathrm{atm} = 0.82\ \mathrm{mg\ cm^{-3}}$, which in turn yields a Molière radius of $r_\mathrm{M} \approx 117$ m.

2.4.3 Particle arrival time distribution

Knowledge of the arrival time distributions of particles in the air shower is necessary to parametrise the curvature and thickness of the shower front as a function of radial distance to the core. Unfortunately, the development of the particle arrival time distributions during the shower evolution is not well established. Agnetta et al. (1997) have analysed Haverah Park data of more than 450,000 air shower events. These lie in the adequate energy range of $\sim 10^{17}$ eV, but were measured at an altitude of 220 m and cannot differentiate between $\mathrm{e}^\pm$ and $\mu^\pm$. They, however, still trace the distribution of $\mathrm{e}^\pm$ correctly because the number of $\mathrm{e}^\pm$ by far exceeds the number of $\mu^\pm$. An earlier analysis of Volcano Ranch data by Linsley (1986) reflects the particle distribution at an altitude of 1,800 m, but is based on a very low number of events (especially at the radial distances up to a few hundred metres relevant to our model) and only determines the shower thickness and not the functional form of the arrival time distributions. We therefore base our model on the Agnetta et al. (1997) data and use the Linsley (1986) data only for comparison.

In Agnetta et al. (1997) the measured arrival time distribution at a given radial distance is fitted with a Γ-probability distribution function (Γ-pdf) defined as

$$f(t) = A\, t^B\ \exp(-Ct), \tag{2.25}$$

the form of which (cf. Fig. 2.4) arises from multiple scattering events during the shower propagation. While A only comprises a normalisation factor, the fit

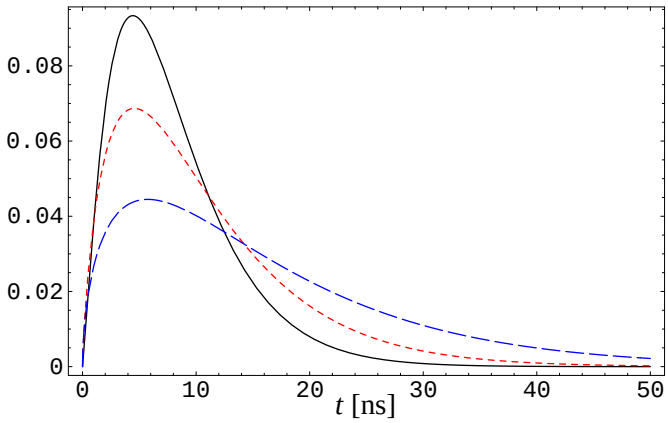

FIGURE 2.4—Γ-pdf determining the arrival time distribution of particles as measured by Agnetta et al. (1997). Solid: in the shower centre, short-dashed: 50 m from shower centre, long-dashed: 100 m from shower centre.

parameters B and C of the Γ-pdf are directly related to the mean arrival time $< t >$ and the standard deviation σ_t of the measured arrival time distributions (Bury 1975),

$$B = \left(\frac{< t >}{\sigma_t}\right)^2 - 1 \quad \text{and} \quad C = \frac{< t >}{\sigma_t^2}. \tag{2.26}$$

The dependence of $< t >$ and σ_t on the radial distance to the shower core is modeled by a generalised paraboloid of the form

$$< t > (r), \sigma_t(r) = F + G\ (r/r_0)^H \tag{2.27}$$

where r_0 is set to the Molière radius at ground level of 79 m. The parameter sets for $< t > (r)$ and $\sigma_t(r)$ are listed as

$$\begin{aligned} F_t &= (8.039 \pm 0.068)\ \text{ns} \\ G_t &= (5.508 \pm 0.095)\ \text{ns} \\ H_t &= 1.710 \pm 0.059 \end{aligned} \tag{2.28}$$

and

$$\begin{aligned} F_\sigma &= (5.386 \pm 0.025)\ \text{ns} \\ G_\sigma &= (5.307 \pm 0.032)\ \text{ns} \end{aligned} \tag{2.29}$$

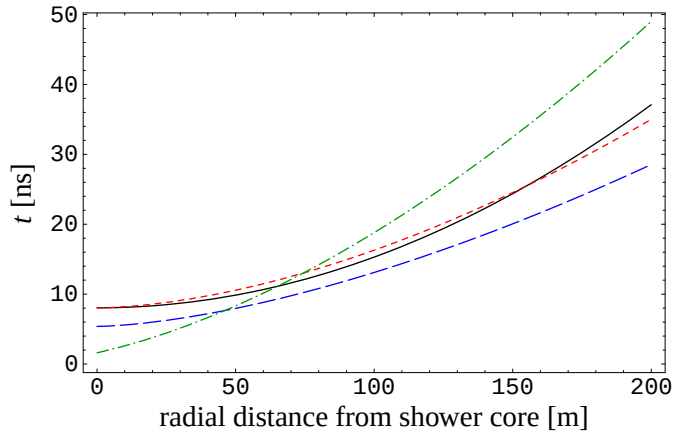

FIGURE 2.5—Radial dependence of the particle arrival time distribution. Solid: shower curvature as given by a spherical surface with $K = 2,300$ m, short-dashed: $< t > (r)$ as given by Agnetta et al. (1997), long-dashed: $\sigma_t(r)$ as given by Agnetta et al. (1997), dash-dotted: $\sigma_{t,\mathrm{L}}(r)$ as given by Linsley (1986).

$$H_\sigma \quad = \quad 1.586 \pm 0.020.$$

Fitting the arrival time distribution with a Γ-pdf partially cuts off the long tail of particles arriving with very high delay. Since the radio emission is, however, dominated by the bulk of the particles, the effect is negligible for our calculations.

The thickness of the shower "pancake" is directly determined by σ_t. The "effective curvature" of the shower front is governed by two factors. On the one hand, there is a delay of the *first* particles of the Γ-pdf arriving at distance r from the shower core with respect to the first particles arriving in the shower centre. This effect is not included in the Agnetta et al. (1997) data. Here we assume that the delay is negligible for the shower distances $\lesssim 100$ m that we are interested in (the first particles can, with good agreement, be assumed to lie on a flat surface). On the other hand, the *mean* particle delay rises as one goes to greater distances from the shower core, a fact represented by the increase of $<t>(r)$. The shower curvature determined by $<t>(r)$ can be expressed very well with a spherical surface of curvature radius $K = 2,300$ m, as can be seen in Figure 2.5.

For comparison, we also examine the Linsley (1986) parametrisation for

σ_t, which is defined as

$$\sigma_{t,L} = G_{\rm L}\,(1 + r/r_{\rm L})^{H_{\rm L}}, \tag{2.30}$$

where, for a 10^{17} eV vertical air shower, we have $G_{\rm L} = 1.6$ ns, $r_{\rm L} = 30$ m and $H_{\rm L} = 1.68 \pm 0.14$. As Linsley (1986) does not specify the functional form of the arrival time distribution, we assume that it also corresponds to a Γ-pdf. However, since $< t >$ and σ_t are not independent in this parametrisation, we have to assume a $< t >(r)$ that fits the $\sigma_t(r)$-distribution given by Linsley. From the fact that

$$< t >= \sqrt{1 + B}\,\sigma_t \tag{2.31}$$

and the relative constancy of $B(r)$ in the Agnetta et al. (1997) data, a natural choice for the distribution is given by

$$< t >_{\rm L}(r) = \frac{< t >_{\rm A}(r)}{\sigma_{t,{\rm A}}(r)}\,\sigma_{t,{\rm L}}(r), \tag{2.32}$$

where the index A refers to the Agnetta parametrisations and L refers to the Linsley parametrisations.

2.4.4 Particle energy distribution

The average energy of the electrons and positrons in an air shower corresponds to ~ 30 MeV, i.e. $\gamma \sim 60$ (Allan 1971). As a very crude approximation, one can therefore adopt a mono-energetic configuration of particles with $\gamma \equiv 60$. To illustrate the effects induced by a more realistic particle energy distribution, we compare this with a (spatially uniform) broken power-law distribution of particle energies where $\mathrm{d}N/\mathrm{d}\gamma$ rises linearly with γ, peaks at $\gamma_0 = 60$ and then declines as γ^{-2}:

$$p(\gamma) = \left(\frac{\gamma}{\gamma_1}\right)^u \left(1 - \mathrm{e}^{-(\gamma/\gamma_1)^{w-u}}\right), \tag{2.33}$$

where we set $u = 1$, $w = -2$ and $\gamma_1 = 74.2$ which corresponds to a peak of the distribution at $\gamma_0 = 60$. One can then calculate the emission of an "energy averaged" particle through

$$\boldsymbol{E}_\gamma(\boldsymbol{R}, \omega) = p_0 \int_{\gamma_{\rm min}}^{\gamma_{\rm max}} p(\gamma)\,\boldsymbol{E}(\boldsymbol{R}, \omega)\,\mathrm{d}\gamma, \tag{2.34}$$

where the normalisation constant p_0 is

$$p_0 = \frac{1}{\int_{\gamma_{\min}}^{\gamma_{\max}} p(\gamma)\,\mathrm{d}\gamma}. \tag{2.35}$$

This energy integration leaves the number of particles unchanged. Note, however, that the total amount of energy in the particles varies with changing $\gamma_{\min}$ and $\gamma_{\max}$. Additionally, $\gamma_{\min}$ must not be chosen too small as our derivations include approximations that are only valid in the ultra-relativistic case. In general, the presence of high-energy particles amplifies the emission near the shower centre, whereas low-energy particles enhance the radiation at high distances due to their wider beaming cone.

We will continue to compare results with both mono-energetic and broken power-law particle distributions and differentiate the two cases through the absence or presence of an additional index γ. Any result calculated for a broken power-law distribution, indicated through an index γ, also applies to the mono-energetic case if one substitutes the energy-averaged $\boldsymbol{E}_\gamma(\boldsymbol{R},\omega)$ by the original $\boldsymbol{E}(\boldsymbol{R},\omega)$.

2.5 Coherence: longitudinal effects

Having established the emission from individual particles and the spatial distribution of particles in the air shower, we can now calculate the emission from the shower maximum, taking into account the inherent (observer-frame) shower structure. The phase differences between the pulses from the individual particles lead to strong coherence effects that significantly change the spectrum of the received emission from that of a fully coherent synchrotron pulse. (For a general discussion of coherence effects regarding synchrotron radiation see also Aloisio & Blasi 2002.)

To get a better understanding of the spectral features, we start with a strongly simplified configuration that neglects any lateral structure: We reduce the shower to its core. In this approximation, the air shower "pancake" of thickness d is collapsed to a one-dimensional line of length d. The charges distributed along the line are adopted to move synchronously, i.e. the momentum distribution of the particles at a given time corresponds to a δ-function. The emission from a particle at distance $\boldsymbol{R} = \hat{\boldsymbol{n}}R$ from the observer is given by $\boldsymbol{E}(\boldsymbol{R},\omega)$ as defined in Eq. (2.9). For a particle offset by a distance x from the

line-centre (located at $\boldsymbol{R_0}$) along the shower core direction $\hat{\boldsymbol{l}}$, we therefore have

$$\begin{aligned}
\boldsymbol{E}(\boldsymbol{R_0} + x\hat{\boldsymbol{l}}, \omega) &\propto \frac{1}{|\boldsymbol{R_0} + x\hat{\boldsymbol{l}}|} \exp\left(\frac{\mathrm{i}\omega|\boldsymbol{R_0} + x\hat{\boldsymbol{l}}|}{c}\right) A_{\parallel}(\omega) \\
&\approx \frac{1}{|\boldsymbol{R}_0|} \exp\left(\frac{\mathrm{i}\omega|\boldsymbol{R_0} + x\hat{\boldsymbol{n}}|}{c}\right) A_{\parallel}(\omega) \\
&= \frac{1}{R_0} \exp\left(\frac{\mathrm{i}\omega(R_0 + x)}{c}\right) A_{\parallel}(\omega). \qquad (2.36)
\end{aligned}$$

Here we keep the distance of the particle at the constant value R_0 for the first factor, which only introduces negligible errors since $d \ll R_0$. The approximation of $\hat{\boldsymbol{l}} \approx \hat{\boldsymbol{n}}$ in the second factor is justified since $A_{\parallel}$ only gives significant contributions if the directions of $\hat{\boldsymbol{l}}$ and $\hat{\boldsymbol{n}}$ enclose angles of order γ^{-1} or smaller. In other words, projection effects do not play a significant role because only in the regime where they are very small, we have significant emission from the particles.

Defining the particle distribution function $f(x)$ such that $\int_{-\infty}^{+\infty} f(x)\,\mathrm{d}x = 1$, and taking into account the particle energy distribution, the integrated emission from N particles is then given by

$$\begin{aligned}
\boldsymbol{E}^N_{\gamma,l}(\boldsymbol{R}, \omega) &= \int_{-\infty}^{+\infty} N f(x)\, \boldsymbol{E}_{\gamma}(\boldsymbol{R_0} + x\hat{\boldsymbol{l}}, \omega)\,\mathrm{d}x \\
&\approx N\boldsymbol{E}_{\gamma}(\boldsymbol{R_0}, \omega) \int_{-\infty}^{+\infty} f(x)\, \mathrm{e}^{\mathrm{i}\omega\frac{x}{c}}\,\mathrm{d}x \\
&= N\boldsymbol{E}_{\gamma}(\boldsymbol{R}_0, \omega)\, S(\omega). \qquad (2.37)
\end{aligned}$$

Note that this basically corresponds to a Fourier transformation, i.e. the function $S(\omega)$ modulating the field strength spectrum is given by the Fourier transform of the particle distribution function, as in standard diffraction theory. (The energy spectrum is then modulated by $|S(\omega)|^2$.)

We will now compare a number of different distributions of particles along the line to better understand the coherence effects that arise from longitudinal distributions of particles.

2.5.1 Uniform line charge

The easiest case of a line charge is a uniform distribution of particles along a line of length d,

$$f(x) = \begin{cases} 1/d & \text{for} \quad |x| \le d/2 \\ 0 & \text{for} \quad |x| > d/2 \end{cases} . \tag{2.38}$$

Integration over x then leads to the well-known $(\sin z/z)^2$ modulation of the energy spectrum that corresponds to the diffraction pattern of a rectangular opening,

$$S(\omega) = \int_{-\frac{d}{2}}^{+\frac{d}{2}} \frac{1}{d}\, \mathrm{e}^{\mathrm{i}\omega\frac{x}{c}}\, \mathrm{d}x = \frac{\sin(d\omega/2c)}{d\omega/2c}. \tag{2.39}$$

2.5.2 Gaussian line charge

A more realistic case is that of a Gaussian distribution of particles along the line. The width of the distribution is set by the standard deviation of the Gaussian σ (the FWHM then corresponds to $\sqrt{4\,\ln 4}\,\sigma \approx 2.35\,\sigma$), with the distribution being defined as

$$f(x) = \frac{1}{\sigma\sqrt{2\pi}}\, \exp\left(-\frac{1}{2}\frac{x^2}{\sigma^2}\right). \tag{2.40}$$

The coherence function then equals

$$S(\omega) = \exp\left(-\frac{1}{2}\frac{\sigma^2}{c^2}\omega^2\right), \tag{2.41}$$

i.e. a Gaussian as well, which is clear from the fact that the Fourier transform of a Gaussian is again a Gaussian.

2.5.3 Asymmetrical Γ-distribution

A realistic longitudinal particle distribution is given by an arrival-time distribution as specified by Eq. (2.25) with the substitution $x = ct$,

$$f(x) = \begin{cases} A\left(\frac{x}{c}\right)^B \exp\left(-C\,\frac{x}{c}\right) & \text{for} \quad x > 0 \\ 0 & \text{for} \quad x \le 0 \end{cases} , \tag{2.42}$$

where from the normalisation of $f(x)$ follows

$$A = \left[C^{-(1+B)}\Gamma(1+B)\right]^{-1} . \tag{2.43}$$

The corresponding coherence function $S(\omega)$ is then given by

$$\begin{aligned} S(\omega) &= \left(1+\frac{\omega^2}{C^2}\right)^{-\frac{1}{2}(1+B)} \exp\left[\mathrm{i}(1+B)\arctan\left(\frac{\omega}{C}\right)\right] \\ &\times \exp\left(-\mathrm{i}\omega < t >_{\mathrm{A}}\right), \end{aligned} \tag{2.44}$$

where the last phase factor is needed to "centre" the asymmetrical distribution on the curved shower surface to make it comparable to the symmetrical uniform and Gaussian distribution for the later calculations taking into account lateral structure. (The origins of the Γ-pdfs then again lie on a flat surface as discussed in Section 2.4.3.)

2.5.4 Model calculations

The results derived so far allow us to perform a number of model calculations in order to analyse the effects of longitudinal particle distributions on the observed spectra as well as the dependence of the emission on the observer's radial distance from the shower core. Where no analytical result was presented, integrations and other calculations are done numerically. We model the maximum of a vertical air shower with primary particle energy $E_{\mathrm{p}} = 10^{17}$ eV and therefore $N = 10^8$ particles at a height of $R_0 = 4$ km. This is a realistic value as outlined in Section 2.4.1. The earth's magnetic field is adopted with a strength of $B = 0.3$ G and, for simplicity and symmetry reasons, assumed to be perpendicular to the shower core and thus parallel to the earth's surface (a realistic value for central Europe would be $B = 0.5$ G with declinations around 70°).

The thickness of the air shower "pancake" is determined by the standard deviation σ_t as parametrised in Sect. 2.4.3. To ensure an equivalent width of the Γ-pdf, the uniform line charge and the Gaussian line charge, we normalise the latter distributions such that they have a standard deviation of $c\sigma_t$. For the Gaussian distribution, this corresponds to $\sigma = c\sigma_t$. The uniform line charge must be set to a total length of $d = 2\sqrt{3}c\sigma_t$. Evaluated in the shower core, $c\sigma_t(0) = 1.61$ m, which results in $d = 5.6$ m.

Fig. 2.6 compares the spectral modulations arising from the different longitudinal particle distributions. If the particles radiated fully coherently — i.e. moved "as one particle" on the exact same trajectory — the field strength spectrum of the emission would simply be a synchrotron spectrum enhanced by a factor N. The coherence effects modulate this spectrum by the coherence function $S(\omega)$. In the case of the uniform line charge, we see the first coherence minimum at ≈ 54 MHz, which corresponds to c/d. The Gaussian line charge

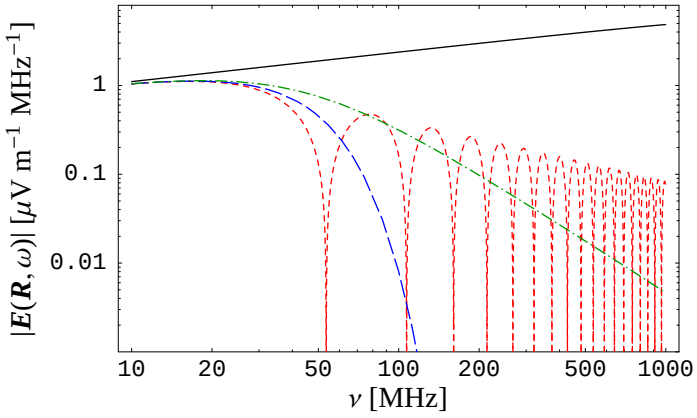

FIGURE 2.6— $|\boldsymbol{E}(\boldsymbol{R}, 2\pi\nu)|$-spectrum in the centre of the area illuminated by the maximum of a 10^{17} eV air shower with $R_0 = 4$ km and $\gamma \equiv 60$. Solid: full coherence, short-dashed: uniform 5.6 m line charge, long-dashed: Gaussian line charge with $\sigma = 1.61$ m, dash-dotted: asymmetrical Γ-distribution with $c\sigma_t = 1.61$ m

spectrum does not exhibit such a sharp minimum, but is strongly attenuated at higher frequencies. The asymmetrical Γ-pdf lies between these two simplified models.

Obviously the longitudinal effects very strongly modulate the emitted spectrum at high frequencies ($\gtrsim$ 50 MHz) and therefore are an important limiting factor for the choice of a suitable observing frequency. The thickness of the air shower "pancake" has a very profound and direct influence on the emitted radiation and could therefore be probed directly through observations of radio emission from EAS at frequencies > 50 MHz.

Another interesting characteristic of the radiation is its radial dependence at a given frequency as illustrated by Fig. 2.7 for the case of full coherence without any longitudinal distribution, i.e. for particles concentrated in a point source. In this case, the associated emission pattern is purely governed by the inherent emission pattern of the synchrotron pulses. The extent of the illuminated area on the ground is an important characteristic that ultimately limits the probability to detect very scarce ultra-high energy cosmic ray air showers with a given collecting area.

As expected, adoption of the broken power-law distribution of particle energies influences the radial emission pattern. Going from the mono-energetic case to the broken power-law energy distribution mainly amplifies the emission

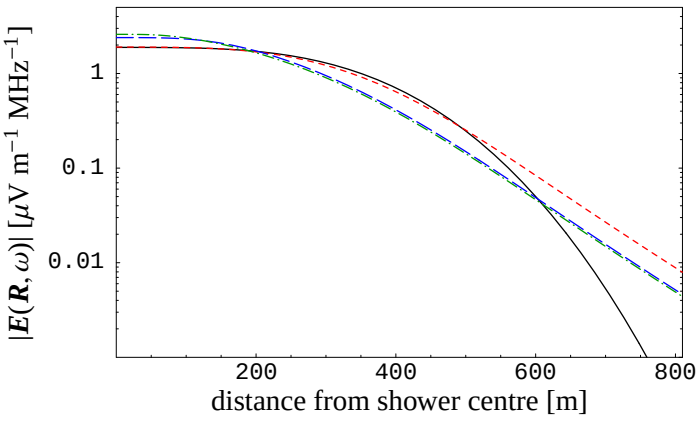

FIGURE 2.7—Radial dependence of $|\boldsymbol{E}(\boldsymbol{R}, 2\pi\ 50\ \text{MHz})|$ for the maximum of a 10^{17} eV point source shower with $R_0 = 4$ km for the $\gamma \equiv 60$ case (solid) and for broken power-law distributions from $\gamma = 5$–120 (short-dashed), $\gamma = 5$–1000 (long-dashed) and $\gamma = 5$–10000 (dash-dotted).

in the centre region due to the presence of high energy particles that radiate more strongly, but into a smaller beaming cone. At the same time, the low-energy particles amplify the emission at very high distances due to their wider emission pattern. The drop in the number of medium-energy particles is correspondingly reflected in a drop of the emission on medium scales. Obviously, there is only negligible difference when increasing the upper limit γ_{max} from a value of 1000 to higher values such as 10000. For the remaining calculations, we therefore adopt a distribution with γ in the range 5–1000 to minimise computation time.

2.6 Coherence: lateral effects

After having analysed coherence effects arising from longitudinal distributions of particles, we now take a look at the influence of the lateral structure of the air shower on the radio emission. This we accomplish by "smearing out" the line charge considered so far over a segment of a spherical surface with (for the moment) constant thickness d. Inside this "shell" we continue to consider the types of longitudinal particle distributions introduced in Section 2.5.4.

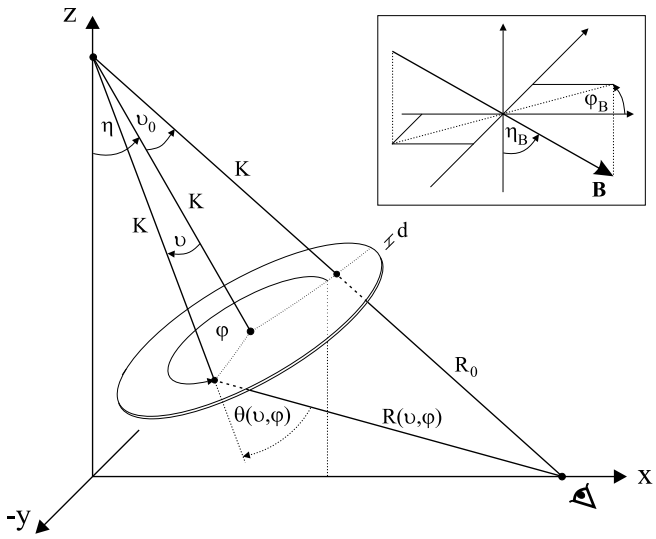

FIGURE 2.8—The geometry for the air shower maximum.

2.6.1 Geometry

The geometry of the air shower maximum is defined as in Fig. 2.8 and characterised by the curvature radius of the shower surface K, the shower shell thickness d and the shower inclination angle η. The observer is positioned on the x-axis at a minimum distance R_0 from the shower surface, with an inclination angle ϑ_0 to the shower core. The magnetic field strength B, inclination η_B and azimuthal direction φ_B determine the configuration of the earth's magnetic field.

To derive the total emission from the air shower maximum, we now have to integrate over the shell and hence must relate $\boldsymbol{E}(\boldsymbol{R},\omega)$ and consequently the quantities going into $\boldsymbol{E}(\boldsymbol{R},\omega)$ to the position on the surface as given by ϑ and φ. We refer the reader to the appendix for the details of these calculations.

2.6.2 Approximations

In order to facilitate the integration over the shower shell we apply a number of approximations. First, we sum the contributions from the different regions of the air shower maximum in a scalar way, i.e. we do not evaluate Eq. (2.55) but set $\hat{\mathbf{e}}_{\parallel}(\vartheta,\varphi) \equiv \hat{\mathbf{e}}_{\parallel}(0,0)$, which is justified due to the minute changes in

the direction of $\hat{\mathbf{e}}_{\parallel}(\vartheta, \varphi)$ over the shower surface. The general polarisation direction of the radiation then is perpendicular to both the shower axis and the magnetic field direction. Second, as pointed out in the appendix, we assume that the instantaneous velocity vectors of the particles in the shower shell are perpendicular to the shower surface at the moment corresponding to the origin of Figure 2.1. This again corresponds to a δ-function for the distribution of the particle momenta, and in this strict sense, the minimum angle to the line-of-sight $\theta(\vartheta, \varphi)$ is given by Eq. (2.54).

Adoption of this θ, however, yields a very conservative estimate for the emission. $\theta(\vartheta, \varphi)$ as calculated by Eq. (2.54) overestimates the minimum angle to the line-of-sight as defined in Fig. 2.1 in case of a particle trajectory bending towards or away from the observer, where a significantly reduced θ is reached during a later or earlier position on the particle trajectory. The amount of "compensation" in θ attainable by this effect is considerable since the ratio of mean free path length to curvature radius of $\gamma = 60$ electrons is $\sim 450\,\mathrm{m}/3400\,\mathrm{m} \approx 8\,\gamma^{-1}$. θ is therefore effectively reduced to its irreducible component given by

$$\sin\theta(\vartheta, \varphi) = \hat{\boldsymbol{B}} \cdot \hat{\boldsymbol{n}}(\vartheta, \varphi). \tag{2.45}$$

Adoption of this value for $\theta(\vartheta, \varphi)$ yields a more realistic estimate of the emission from the air shower shell, and at the same time takes into account the asymmetry of the emission pattern in φ that arises from the magnetic field configuration. Without a more precise criterion for the maximum compensation achievable, however, the radial dependence of the emission pattern at very high distances is obviously no longer valid. We therefore continue to work with both the conservative approach using Eq. (2.54) and the "reduced θ" definition in order to compare the two cases.

The change in R associated to the adoption of the "optimum position" on the particle trajectory is negligible because of the following reasons:

- the compensated angles are small, therefore the changes in R are small
- additional attenuation/amplification through the $1/R$-term is thus negligible
- there is no significant change of phase since the particle velocity $v \approx c$ and the trajectory is only mildly curved.

2.6.3 Integration

Using these geometrical relations, the integrated spectrum of the emission from the air shower maximum with N particles can be calculated as

$$\begin{aligned} \boldsymbol{E}^{N}_{\gamma,\mathrm{S}}(\omega) &= \rho_0 \int_0^{2\pi} \mathrm{d}\varphi \int_0^{r_\mathrm{M}/K} \mathrm{d}\vartheta \, K^2 \sin\vartheta \\ &\times \rho_\mathrm{NKG}(r(\vartheta,\varphi)) \, \boldsymbol{E}_\gamma(\boldsymbol{R}(\vartheta,\varphi),\omega) \end{aligned} \tag{2.46}$$

with the normalisation factor

$$\rho_0 = N \left[\int_0^{2\pi} \mathrm{d}\varphi \int_0^{r_\mathrm{M}/K} \mathrm{d}\vartheta \, K^2 \sin\vartheta \, \rho_\mathrm{NKG}(r(\vartheta,\varphi)) \right]^{-1}. \tag{2.47}$$

Cutting off the integration at $\vartheta = r_\mathrm{M}/K$ significantly reduces computation time while giving acceptable accuracy as $\gtrsim 80$ % of the particles are included in this region. The remaining particles are redistributed over the integration region by the normalisation according to the NKG-profile, which might lead to a slight overestimation of the emission strength near the shower centre.

2.6.4 Model Calculations

We again examine the frequency and radial dependence of the emission to study the effects introduced through the lateral particle distribution. The basic parameters adopted are the same as in Sec. 2.5.4, but we assume a broken power-law particle energy distribution from $\gamma = 5$–1000 for all calculations. The curvature radius of the shell is adopted as $K = 2,300$ m and the Molière radius set to $r_\mathrm{M} = 117$ m as discussed in Sects. 2.4.3 and 2.4.2, correspondingly.

In Fig. 2.9 we plot the spectrum received by an observer in the centre of the area illuminated by the air shower maximum, considering the same set of longitudinal particle distributions as before. The spectra look very similar to those of a line charge, but are attenuated additionally at high frequencies.

A more interesting result is illustrated by Fig. 2.10 which demonstrates the effect of a purely lateral particle distribution on the radial dependence of the emission in the "conservative θ" scenario, completely ignoring any longitudinal effects. The lateral structure introduces a modulation of the radial dependence, caused by interference of emission from opposite ends of the shower "disk". For higher frequencies and, correspondingly, shorter wavelengths, the interference minima move to smaller radial distances.

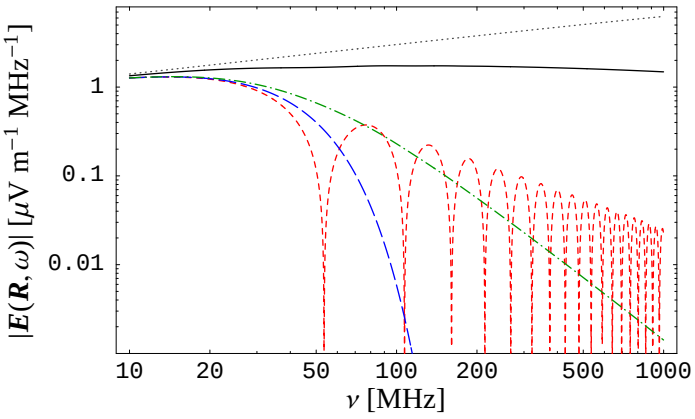

FIGURE 2.9— $|\boldsymbol{E}(\boldsymbol{R}, 2\pi\nu)|$-spectrum at the centre of the area illuminated by the maximum of a 10^{17} eV air shower with realistic lateral distribution, R_0 = 4 km and a broken power-law energy distribution from γ = 5–1000. Solid: full longitudinal coherence, short-dashed: uniform 5.6 m longitudinal distribution, long-dashed: Gaussian longitudinal distribution with σ = 1.61 m, dash-dotted: longitudinal Γ-distribution with $c\sigma_t$ = 1.61 m. For comparison: fully coherent case without lateral distribution (dotted)

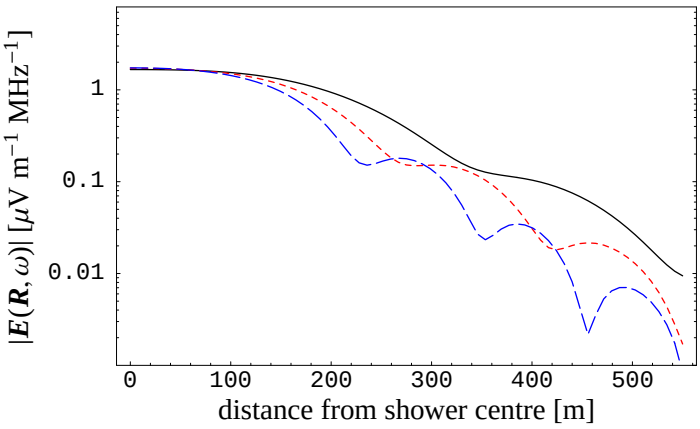

FIGURE 2.10—Radial dependence of $|\boldsymbol{E}(\boldsymbol{R}, 2\pi\nu)|$ for the maximum of a 10^{17} eV air shower with full longitudinal coherence, realistic lateral structure, "conservative θ" approach, R_0 = 4 km and a broken power-law energy distribution from γ = 5–1000. Solid: ν = 50 Mhz, short-dashed: ν = 75 Mhz, long-dashed: ν = 100 Mhz

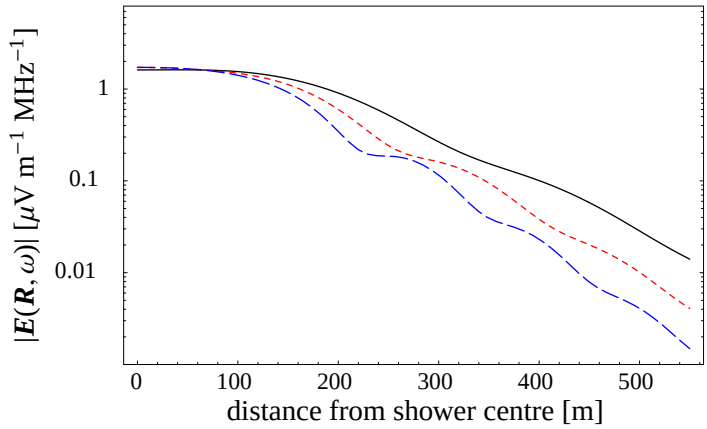

FIGURE 2.11—Same as Fig. 2.10 but with "reduced θ" and magnetic field parallel to the direction of the observer.

In comparison, Figs. 2.11 and 2.12 show the radial dependence in case of the "reduced θ" calculations. The interference effects are somewhat washed out and the overall emission level is higher. As expected, there is a drastic asymmetry between the emission pattern in the directions parallel and perpendicular to the magnetic field. In case of Fig. 2.12, where the observer is positioned in a direction perpendicular to the magnetic field, θ is basically reduced to zero even for distances of a few hundred metres ($\theta \lesssim 8\,\gamma^{-1}$ as explained in Section 2.6.2). Correspondingly, the emission pattern is only very slightly attenuated even at high distances.

2.7 Flaring disk

We now combine the results derived so far to obtain a more realistic model of the emission from the maximum of an extensive air shower: a "flaring" disk. In other words, we adopt the same geometry as specified in Sec. 2.6, but now vary the thickness of the disk as a function of position (ϑ, φ) on the shower surface in the form of the varying asymmetric Γ-pdfs parametrised as in Section 2.4.3. This geometry therefore correctly takes into account the curvature, the lateral and the longitudinal structure of the air shower maximum.

Fig. 2.13 again shows the spectrum emitted by the air shower maximum as a realistically flaring disk according to the Agnetta et al. (1997) and Linsley (1986) parametrisations. As expected, the spectrum emitted by the Linsley

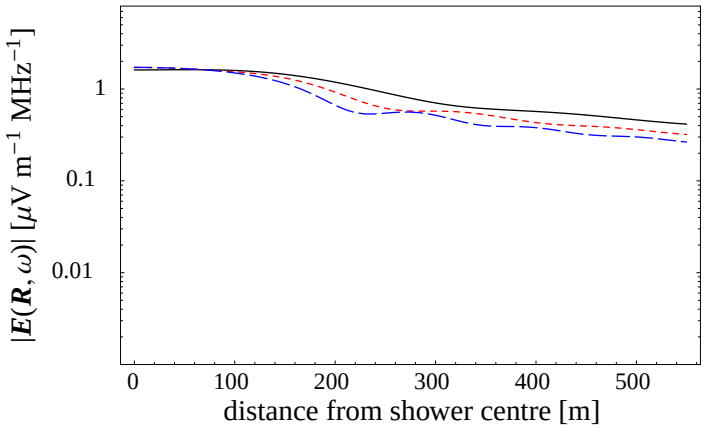

FIGURE 2.12—Same as Fig. 2.10 but with "reduced θ" and magnetic field perpendicular to the direction of the observer.

flaring disk extends to higher frequencies than the one generated by the Agnetta flaring disk because of the lower thickness in the shower centre where most of the particles reside (cf. Fig. 2.5).

The radial dependence at different frequencies is once again shown in Figure 2.14. Comparison with the corresponding diagrams for the purely lateral distribution shown in Figs. 2.10–2.12 shows that the overall emission level drops as the observing frequency is increased due to the dampening of higher frequencies by the longitudinal particle distribution. Additionally, one can again observe a "smearing out" of the interference minima. As a consequence, the "conservative θ" and the "reduced θ" with observer parallel to the magnetic field calculations yield almost identical results.

In Fig. 2.15 we have reconstructed the pulse generated by the flaring Agnetta disk as it would be measured by a receiver with a given bandwidth using Eq. (2.10). The pulse amplitude drops noticeably when the observer moves from the centre of the illuminated area on the ground to a distance of 100 m, and is already quite diminished at a distance of 250 m, as expected for the "conservative θ" approach. The pulse length of $\approx$ 8 ns is a result of the filter bandwidth of 120 MHz, i.e. the pulse is bandwidth-limited.

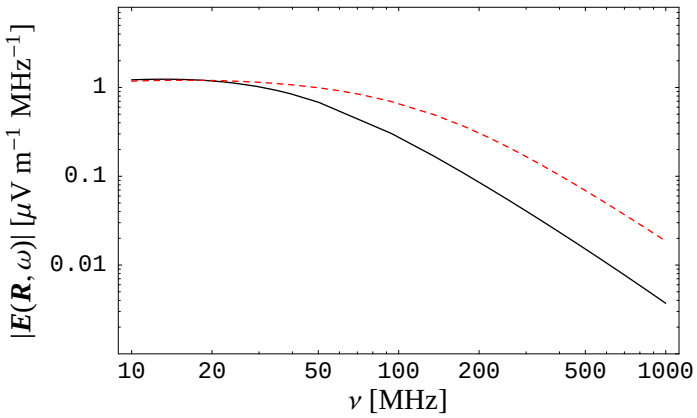

FIGURE 2.13— $|\boldsymbol{E}(\boldsymbol{R}, 2\pi\nu)|$-spectrum at the centre of the area illuminated by the maximum of a 10^{17} eV air shower with flaring Γ-pdf, $R_0 = 4$ km and a broken power-law energy distribution from $\gamma = 5$–1000. Solid: flaring Agnetta et al. (1997) lateral distribution, short-dashed: flaring Linsley (1986) lateral distribution

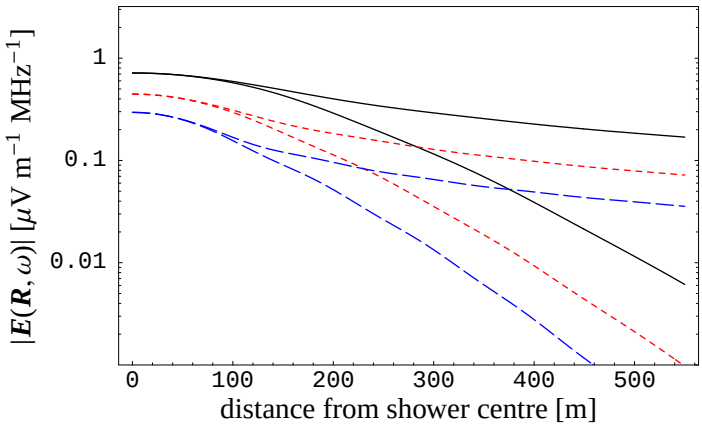

FIGURE 2.14—Radial dependence of $|\boldsymbol{E}(\boldsymbol{R}, 2\pi\nu)|$ for the maximum of a 10^{17} eV air shower with flaring Agnetta et al. (1997) Γ-pdf, $R_0 = 4$ km and a broken power-law energy distribution from $\gamma = 5$–1000. Solid: $\nu = 50$ Mhz, short-dashed: $\nu = 75$ Mhz, long-dashed: $\nu = 100$ Mhz, upper/lower curves for "reduced θ" perpendicular/parallel to magnetic field direction

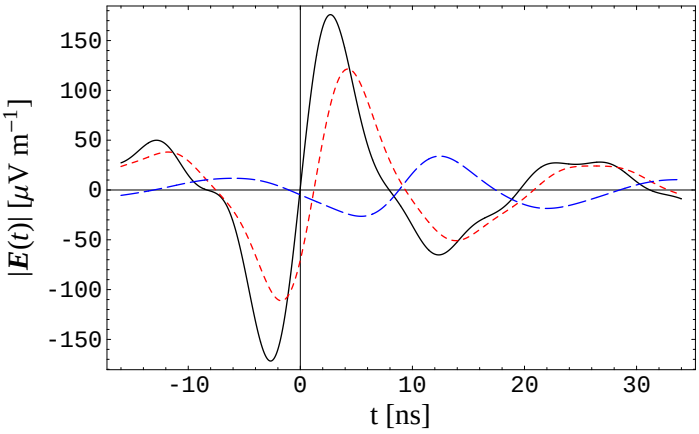

FIGURE 2.15—Reconstructed pulses emitted by the maximum of a 10^{17} eV shower with flaring Agnetta et al. (1997) Γ-pdf, broken power-law energy distribution from $\gamma = 5$–1000 and $R_0 = 4$ km, using an idealised rectangle filter spanning 40–160 MHz and "conservative θ" scenario. Solid: centre of illuminated area, short-dashed: 100 m from centre, dash-dotted: 250 m from centre

2.8 Integration over shower evolution

The last step in modelling the total air shower emission is to integrate over the shower evolution as a whole. This can be done in a very simplified fashion by approximating the shower evolution with a number of discrete steps. The characteristic scale for these steps is given by the "radiation length" of the electromagnetic cascades in air, $X_0 = 36.7$ g cm^{-2}, corresponding to ≈ 450 m at a height of 4 km. One can therefore discretise the shower evolution into "slices" of thickness X_0, assuming these contain independent generations of particles and therefore radiate independently.

The emission from each of these slices is calculated as that from a flaring disk, taking into account changes of s, R_0, ϑ_0, r_M and N correctly through the relations given in Section 2.4 and reverting to the "conservative θ" definition to be able to correctly calculate the emission at great angles. Superposition of the individual slice emissions, correctly taking into account the phases arising from arrival time differences, then leads to the total emission of the shower.

Slices far away from the observer are attenuated both due to the high distance and the decreasing number of particles N. The concrete number of far-away slices taken into account is therefore uncritical. The situation is different for the slices close to the observer. In their case, the attenuation through the

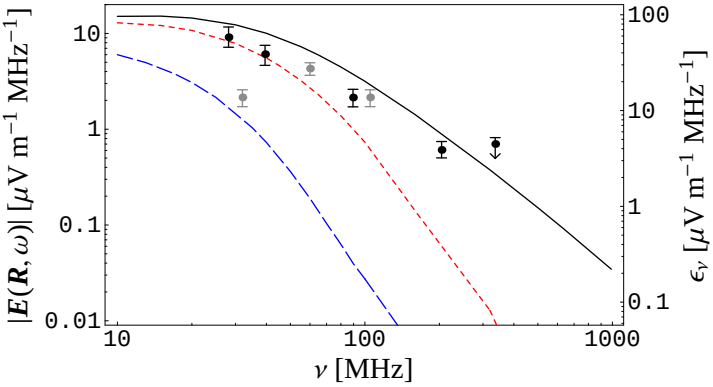

FIGURE 2.16— $|\boldsymbol{E}(\boldsymbol{R}, 2\pi\nu)|$-spectrum of a full 10^{17} eV air shower with fluctuating Agnetta et al. (1997) Γ-pdf, "conservative θ" approach, $R_0 = 4$ km and a broken power-law energy distribution from $\gamma = 5$–1000. Solid: centre of illuminated area, short-dashed: 100 m from centre, long-dashed: 250 m from centre, black points: *rescaled* Spencer (1969) data as presented by Allan (1971), grey points: *rescaled* Prah (1971) data

decreasing number of particles N is more than compensated by the decreasing distance to the observer. In fact, the slices closest to the observer yield the highest contributions of radiation, and the total result depends considerably on the number of nearby slices taken into account. However, at the same time, the illuminated area on the ground, governed by the intrinsic beaming cone, becomes very small for the slices very close to the observer, especially for the high frequencies where the radiation mainly originates from high-energy particles with even smaller beaming cones. Except for low frequency emission in the centre region of the illuminated area, the result for the total emission can therefore be considered robust.

For our vertical 10^{17} eV air shower at a height of $R_0 = 4$ km we add the emission from eight slices above and eight slices below the shower maximum to the emission from the maximum itself. The closest slice then lies at $R_0 = 950$ m from the observer, a distance we do not want to fall below because of approximations contained in our calculations that are only valid in the far-field.

The main effect of the integration over the shower evolution is a boosting of the total emission because of the increased total number of particles taken into account, as can be seen in the spectra shown in Fig. 2.16. For frequencies of ~ 40 MHz and radial distances of ~ 100 m, the amplification factor corre-

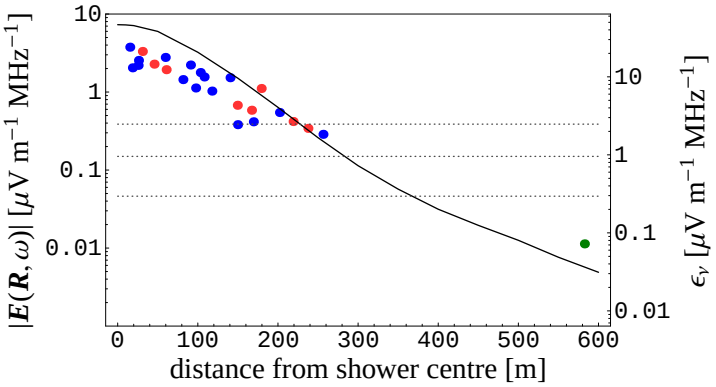

FIGURE 2.17—Radial dependence of $|\boldsymbol{E}(\boldsymbol{R}, 2\pi\,55\,\mathrm{MHz})|$ for a full 10^{17} eV air shower with flaring Agnetta et al. (1997) Γ-pdf, "conservative θ" approach, $R_0 = 4$ km and a broken power-law energy distribution from $\gamma = 5$–1000, data from Allan et al. (1970), horizontal lines from top to bottom: emission strength needed for a 3σ-detection with an individual LOPES antenna or an array of 10 or 100 LOPES antennas

sponds to ~ 10. Apart from the overall amplification, the radial dependence is significantly steepened because the important nearby slices only contribute at low radial distances as discussed earlier. This can be seen when comparing Fig. 2.17 with the earlier results for the "conservative θ" case.

2.9 Discussion

The calculations presented here represent only a few illustrative examples of possible configurations of EAS that could be calculated with our model. These examples, however, already demonstrate the most important dependences between shower structure and emission spectrum as well as radial emission pattern.

2.9.1 Theoretical results

As expected, the thickness of the air shower pancake, and correspondingly in our model the width of the longitudinal particle arrival time distributions, is the main factor determining the position of the high-frequency cut-off in the spectrum. Typical longitudinal scales of a few metres lead to frequency cut-offs in the 100 MHz regime, which supports a choice of observing frequency

well below 100 MHz. Due to the strong dependence of the spectral cut-off on the shower thickness, radio emission from EAS could be used very effectively to probe the longitudinal structure of air showers during their evolution, a quantity that is not well known at the moment.

The radial emission pattern is mainly governed by the inherent emission pattern of the synchrotron pulses and the superposition of the beamed emission from different parts of the air shower evolution as a whole. Additionally, the lateral extent of the air shower slightly influences the size of the illuminated area on the ground through the resulting coherence minima. A profound change in the radial emission pattern is visible when one adopts the "reduced θ" approach, which predicts significant radio emission up to higher distances depending on the relative orientation of observer and magnetic field. This is an important prerequisite for the detection of ultra-high energy EAS with an array of affordable collecting area in combination with particle detector arrays such as KASCADE Grande or the Pierre Auger Observatory and will be verifiable by LOPES.

The emitted total power in the coherent regime at low frequencies scales as the number of particles squared, which could therefore be probed directly by radio measurements of EAS, yielding information about the primary particle energy.

We have not explicitly presented how variations of other parameters influence the radio emission, but most of the associated effects are fairly straightforward to foresee: The emitted power scales linearly with B-field strength. The declination of the B-field in central Europe effectively decreases the value of B and introduces an asymmetric pattern to the radial dependence. An increase of the primary particle energy will boost the radiation because higher-energy showers will have their maximum closer to the observer. At the same time, the number of particles increases linearly with primary particle energy and the power emitted at low frequencies increases as number of particles squared, which more than compensates the shrinking of the illuminated area on the ground. Inclined air showers will cause an asymmetric emission pattern and an attenuation of the emitted power because they reach their development at higher altitudes. A stronger curvature of the shower front will shift the interference minima to smaller radial distances and thus slightly decrease the effective size of the illuminated area on the ground.

2.9.2 Comparison with experimental data

A number of experiments have clearly established the presence of radio emission from cosmic ray air showers in the past. A dependence of the polarisation of the emitted radiation on the earth's magnetic field direction was also confirmed by a number of experiments (e.g., Allan et al. 1967, 1969), supporting the case for the geomagnetic emission mechanism. The actual strength of the emission, however, is still largely unknown at present state. The analysis of Allan (1971) led to a widely used formula summarising the presumed dependences:

$$\begin{aligned} \epsilon_\nu &= 20\,\mu\mathrm{V\,m^{-1}\,MHz^{-1}} \left(\frac{E_\mathrm{p}}{10^{17}\ \mathrm{eV}}\right) \\ &\times \sin\alpha\ \cos\eta\ \exp\left(-\frac{r}{r_0(\nu,\eta)}\right), \end{aligned} \tag{2.48}$$

where the scale factor r_0 corresponds to (110±10) m at $\nu = 55$ MHz and for $\eta < 35°$. Later works (e.g., Sun 1975; Prah 1971 and references therein), however, yielded values as low as 1–5 μV m^{-1} MHz^{-1}. A recent experiment in conjunction with the CASA/MIA array conducted by Green et al. (2003) was only able to place upper limits of $\epsilon_\nu = 31$—$34\,\mu$V m^{-1} MHz^{-1} on the emission strength.

Part of these discrepancies could be explained by uncertainties in the primary particle energy calibration at the time the experiments were made. A number of authors involved in the past works suspect the calibration of the radio measurements to be the major source of uncertainty (Atrashkevich et al. 1978). Additionally, the documentation of the available data is not always totally precise regarding the included energy ranges of primary particles, the selection of allowed zenith angles, the radial distance to the shower axis or the back-projection of the electric field vector in the plane normal to the shower axis and earth's magnetic field, which further complicates the issue.

Extremely low values of ϵ_ν of only 1 μV m^{-1} MHz^{-1} or even lower are, however, disfavoured by the fact alone that air showers actually *have been measured* by experiments with only a few antennas (e.g., two per frequency and polarisation direction in case of Prah 1971) with receivers of only a few MHz bandwidth in the early experiments.

In this difficult situation, we choose to revert to the well documented data of Allan et al. (1970) as the basis of our analysis. A comparison of these data with our predicted radial dependence of the emission is shown in Figure

2.17. While we clearly overpredict the emission strength in the centre, the general radial dependence fits relatively well. Regarding the spectral dependence, we make use of the Spencer (1969) data as presented, converted and complemented in Allan (1971) as well as the Prah (1971) data. These data sets, again, yield considerably lower values of ϵ_ν, and we manually scale them up to make them consistent with the Allan et al. (1970) radial data. While the absolute values presented in Fig. 2.16 therefore are somewhat arbitrary, the trend in the dependence actually does correspond to the spectral dependence that we predict near the shower core.

All in all, we overpredict even the most optimistic past data by a factor ~ 2, which is, however, not too surprising considering the very simplified integration over the shower evolution as a whole and the problems involved especially in the centre region. Additionally, the cutoff of the spatial integration as stated in Sec. 2.6.3 redistributes further emission to the centre region.

We feel that having achieved a result which is consistent with past experimental data within a factor of "a few" using such approximate descriptions of the shower characteristics and a mainly analytical approach incorporating major approximations is a very encouraging outcome. In addition, our result further supports the geomagnetic emission mechanism as the dominant source of radio emission from EAS. A huge improvement of our model will be achieved once we revert to elaborate computer simulations that use fewer approximations and more realistic particle distributions. Consequently, this will be the next step in our modelling efforts.

2.10 Conclusions

We have analysed properties of radio emission from EAS in the scenario of coherent geosynchrotron emission. Our step-by-step analysis has helped to disentangle the coherence effects arising from the different physical scales present in the air shower and to get a good feeling for the relative importance of these effects. While the spectral cutoff is directly governed by the longitudinal extent of the air shower, the radial dependence arises from the intrinsic beaming of the synchrotron radiation and its superposition over the shower evolution as a whole.

The emitted radio power is of the expected order of magnitude, which is the strongest constraint we can make at the moment due to the large uncertainties associated with the available experimental data. Hence, in light of the data available to date, coherent geosynchrotron emission is able to explain the bulk of the radio emission from EAS.

Our calculations show that LOPES should be able to easily detect the radio emission from a typical 10^{17} eV air shower and will be a very useful tool for the study of EAS properties, especially the longitudinal structure of the particle distribution in the shower.

Having achieved a solid understanding of the important effects shaping the radio emission from cosmic ray air showers, our next step will be to conceive and implement an elaborate Monte Carlo simulation calculating the emission with increased precision.

Appendix: Geometry

We adopt the instantaneous velocity vectors of the generated particle pairs as radially pointing away from the centre of the sphere. For a particle at position (ϑ, φ) on the shell, its direction is therefore given by

$$\hat{\boldsymbol{v}}(\vartheta,\varphi) = \begin{pmatrix} \cos\eta\sin\vartheta\cos\varphi + \sin\eta\cos\vartheta \\ \sin\theta\sin\varphi \\ \sin\eta\sin\vartheta\cos\varphi - \cos\eta\cos\vartheta \end{pmatrix}, \tag{2.49}$$

whereas the direction of the B-field is given by

$$\hat{\boldsymbol{B}} = \begin{pmatrix} \sin\eta_B\cos\varphi_B \\ \sin\eta_B\sin\varphi_B \\ -\cos\eta_B \end{pmatrix}. \tag{2.50}$$

Furthermore, the line-of-sight vector $\boldsymbol{R}$ from the particle to the observer is given by

$$\boldsymbol{R}(\vartheta,\varphi) = (R_0 + K)\begin{pmatrix} \sin(\eta+\vartheta_0) \\ 0 \\ -\cos(\eta+\vartheta_0) \end{pmatrix} - K\hat{\boldsymbol{v}}(\vartheta,\varphi) \tag{2.51}$$

The direction of $\boldsymbol{R}$ is then calculated as

$$\hat{\boldsymbol{n}}(\vartheta,\varphi) = \frac{\boldsymbol{R}(\vartheta,\varphi)}{|\boldsymbol{R}(\vartheta,\varphi)|} \tag{2.52}$$

and the pitch angle and angle to the line-of-sight correspond to

$$\cos\alpha(\vartheta,\varphi) = \hat{\boldsymbol{v}}(\vartheta,\varphi)\cdot\hat{\boldsymbol{B}} \tag{2.53}$$

$$\cos\theta(\vartheta,\varphi) = \hat{\boldsymbol{v}}(\vartheta,\varphi)\cdot\hat{\boldsymbol{n}}(\vartheta,\varphi). \tag{2.54}$$

The direction of the dominating emission component then changes as follows with (ϑ, φ):

$$\hat{\mathbf{e}}_{\parallel}(\vartheta, \varphi) = \frac{\hat{\boldsymbol{B}} \times \hat{\boldsymbol{v}}(\vartheta, \varphi)}{|\sin \alpha(\vartheta, \varphi)|}. \tag{2.55}$$

These are all of the geometrical relations that are needed to execute the integration.

3

Monte Carlo simulations

3.1 Introduction

In chapter 2, we presented calculations of radio emission from extensive air showers within the scheme of "coherent geosynchrotron radiation" first proposed by Falcke & Gorham (2003). These calculations were based on an analytic approach and were specifically aimed at gaining a solid understanding of the coherence effects that shape the radiation emitted by an air shower. Building on this foundation, we now continue to develop and enhance our model with elaborate Monte Carlo (MC) simulations. The MC technique allows us to infer the emission characteristics with much higher precision by taking into account more realistic and complex shower properties and applying fewer approximations than in the analytic calculations. At the same time, it provides an independent means to verify our previous calculations due to the totally different technique employed. The approach we take is similar to the MC simulations done by Suprun et al. (2003), yet our simulation is developed to a much higher level of complexity.

The layout of this chapter is as follows: In sections 3.2 and 3.3 we motivate and explain the application of the MC technique and provide details about its implementation. In section 3.4, we explain the "intelligent" concepts that we have explored to make simulations with a high number of particles and observer bins feasible on standard personal computer hardware. After a short description of the raw output of our program and the associated data reduction in section 3.5, we demonstrate the robustness and consistency of the implemented algorithms in detail in section 3.6. Similar to our earlier theoretical

calculations, we then first concentrate on the emission from a single "slice" of particles in the air shower and compare the results with the analytical results in section 3.7. Next, we perform the integration over the shower evolution as a whole and present the results in comparison with our analytical work and historic data in section 3.8 before concluding with a discussion of the results and our conclusions in sections 3.9 and 3.10, respectively.

3.2 The Monte Carlo approach

After having established the general dependences of the radio emission on a number of air shower properties in chapter 2, a continuation of the calculations with MC techniques offers a number of advantages.

3.2.1 Motivation and objectives

First, MC techniques allow an independent verification of the analytic calculations by adopting the exact same shower properties (e.g., distributions of particles in space and energy, choice of magnetic field and shower geometry), but doing the calculations in a completely different way. In particular, the MC calculations are carried out by summing up the individual particles' pulses in the time-domain, whereas the analytic calculations were done in the frequency domain.

Second, it is relatively easy to include highly complex (and thus realistic) shower characteristics in the MC simulations, thereby increasing the model precision significantly over the previous results. Additionally, it is not necessary to make approximations such as adopting a far-field limit, which reduces the accuracy of the analytic calculations.

Overall, MC simulations therefore constitute the logical next step in the development of our model.

3.2.2 General approach

The general idea of a MC simulation of radio emission from cosmic ray air showers is simple:

1. model the radiation emitted by an individual particle as precisely as possible,

2. distribute particles randomly in a simulated shower according to the desired shower characteristics (e.g., spatial and energy distributions),

3. superpose the radiation received from the shower particles at the given observing positions, taking into account retardation effects.

In fact, the "microphysics" of an individual particle's geosynchrotron emission (step 1) can be described analytically without the need of any approximations as long as one does not simulate particle interactions explicitly but only takes them into account via statistically distributed track lengths. The strategy for the implementation of steps 2 and 3 then is as follows:

- generate shower particles according to the desired distributions,
- for each particle:
  - for each observing position (ground-bin):
    - establish an adequate sampling of the particle trajectory,
    - calculate and retard the emission contributions emanating from the sampled points on the trajectory, building up the electric field time-series that the observer sees,
    - incorporate the contributions into the ground-bin's pre-existing time-series data.

This strategy is fairly simple. What makes the problem difficult is the huge computational effort of a simulation with a large number of particles and ground-bins, as was already discussed by Dova et al. (1999) who considered a similar approach. A number of intelligent concepts has to be applied to actually develop a working simulation out of this simple "recipe". We discuss these concepts in depth in section 3.4.

3.3 Implementation details

In this section we describe a number of relevant implementation details of our MC code.

3.3.1 Technical information

We decided to program the MC simulation in C++. This modern, industry-standard programming language offers a number of advantages over others:

- it is highly portable, even among Windows and UNIX/Linux,
- its stringent typing mechanisms force the programmer to write "clean" code,

- the wide range of routines collected and standardised in the “standard template library” (STL) allows an efficient and less error-prone way of programming,
- object-orientation allows to create a modular, flexible and easy to maintain program,
- powerful compilers and debugging tools are freely available,
- the performance is adequate.

The program has been developed under Linux using gcc 2.9.5, gcc 3.3.1, and the Intel C++ compiler version 8.0.5 which produces much faster code. No third-party libraries were used in order to maximise portability and minimise dependency on external factors. The program source-code will be made available at a later time.

3.3.2 Particle creation and propagation

The particles in the shower are created with random properties distributed according to analytic parametrisations. If not explicitly stated otherwise, the parametrisations are chosen exactly as in chapter 2. While these parametrisations are admittedly crude and do not take into account some air shower properties such as a realistic particle pitch-angle distribution, this approach allows a direct comparison of the MC results with our analytic calculations. A more realistic modelling of the air shower will be achieved once our code is interfaced with the air shower simulation code CORSIKA. The particles are created with the following properties chosen randomly:

- the shower age at which a particle is created (longitudinal development according to Greisen (1960) function), which directly yields
  - the position along the shower axis
  - the creation time
- the lateral shift from the shower axis (NKG-distribution dating back to Kamata & Nishimura (1958) and Greisen (1960))
- the longitudinal shift along the shower axis as function of the lateral shift (asymmetrical Γ-PDF)
- the azimuth angle for the lateral shift (isotropic)

- the particle gamma factor (broken power-law distribution or fixed $\gamma \equiv 60$)
- the particle track length (exponential probability distribution or fixed $\lambda \equiv 40$ g cm^{-2})

To take into account the pair-wise creation of particles, one electron and one positron are always generated with the same properties. At the moment, no random spread in the particle pitch-angle is introduced, i.e., the initial particle momenta radially point away from a spherical surface with 2,300 m radius, exactly as in the analytical calculations, motivated by the data from Agnetta et al. (1997). The fact that the initial velocity direction is shared by both the electron and positron introduces only minor error as the transverse momentum arising from the pair production is minimal — a fact that is intuitively illustrated by the still very dense core of the lateral distribution function even after many generations of particle creation.

As each of the particles is created at a specific position at a given time with a given initial velocity, the trajectory $\boldsymbol{r}(t)$ resulting from the deflection in the geomagnetic field is a well-defined helix which can easily be described analytically by equations (3.27), (3.31) and (3.33) as derived in the appendix.

3.3.3 Calculating and collecting contributions

Once the trajectory (and its time-derivatives) are known analytically, the radiation an observer at position $\boldsymbol{x}$ receives at time t can be calculated (cf. Jackson 1975 equation 14.14) immediately by

$$\begin{aligned} \boldsymbol{E}(\boldsymbol{x},t) &= e\left[\frac{\boldsymbol{n}-\boldsymbol{\beta}}{\gamma^2(1-\boldsymbol{\beta}\cdot\boldsymbol{n})^3R^2}\right]_{\text{ret}} \\ &+ \frac{e}{c}\left[\frac{\boldsymbol{n}\times\{(\boldsymbol{n}-\boldsymbol{\beta})\times\dot{\boldsymbol{\beta}}\}}{(1-\boldsymbol{\beta}\cdot\boldsymbol{n})^3R}\right]_{\text{ret}}, \end{aligned} \tag{3.1}$$

where e denotes the particle charge, $\boldsymbol{\beta}(t) = \boldsymbol{v}(t)/c$ is directly given by the particle velocity, $\boldsymbol{R}(t)$ refers to the vector between particle and observer position, $R(t) = |\boldsymbol{R}(t)|$ and $\boldsymbol{n}(t) = \boldsymbol{R}(t)/R(t)$ denotes the line-of-sight direction between particle and observer.

The index "ret" points out that the quantities in the brackets have to be evaluated at the *retarded* time

$$t_{\text{ret}} = t - R(t_{\text{ret}})/c \tag{3.2}$$

rather than at the time t in order to accommodate the finite light-travel time. This "recursive" retardation relation imposes significant problems for an analytical calculation in the time-domain. In case of a MC simulation, on the other hand, it is absolutely straight forward to take the retardation into account by simply delaying the emitted signal appropriately before collecting it in the ground-bins.

The first term in equation (3.1) constitutes the "static" term that falls off with R^{-2} in field strength. It is usually neglected, and was not taken into account in the analytical calculations of chapter 2 either. While its contributions are indeed negligible, we still include it in our MC simulation as to not make any unnecessary approximations.

The second term is the usual "radiation" term which drops as R^{-1} in field strength and therefore dominates very quickly over the static term as one goes to higher distances. In analytic approaches, it is usually necessary to apply approximations such as the Fraunhofer-approximation for the far-field limit to this term, which naturally limits the precision of the results. Again, for a MC simulation, it is not necessary to make any approximation for the radiation formula.

Beaming effects are naturally taken into account in this formula through the $(1 - \boldsymbol{\beta} \cdot \boldsymbol{n})^3$ terms in the denominator that lead to very high field strengths for particle velocities close to c and small angles to the line-of-sight. As soon as one takes into account the refractive index of a medium rather than vacuum, the denominator actually becomes zero at the Čerenkov angle. The arising singularity, in combination with the modified retardation relation, then leads to Čerenkov radiation. The analysis of these effects, however, is beyond the scope of this work and will be carried out in a later paper.

For a given particle, the trajectory is then sampled in a sufficiently high number of points, and the retarded contribution emanating from each of these points is calculated for each of the observing ground-bins with the full precision of equation (3.1). Thus, the retarded electric field time-series produced by the particle is inferred for each of the ground-bins and can then be incorporated into their pre-existing time-series data. The details and subtleties of this procedure are explained in sections 3.4.2 and 3.4.3.

3.3.4 Atmosphere model

We use the US standard atmosphere of 1977 as implemented in CORSIKA (Ulrich 1997). It splits the atmosphere in a number of layers, in each of which the path depth in g cm^{-2} (as counted vertically from the outer edge of the

Layer	Height [km]	a_i [g cm^{-2}]	b_i [g cm^{-2}]	c_i [cm]
1	0 – 4	-186.56	1222.66	994186.38
2	4 – 10	-94.92	1144.91	878153.55
3	10 – 40	0.61	1305.59	636143.04
4	40 – 100	0.00	540.18	772170.16

TABLE 3.1—Parameters for the parametrisation of the atmospheric layers.

atmosphere) is parametrised by an exponential dependence on height

$$X(h) = a_i + b_i \exp\left(-\frac{h}{c_i}\right). \tag{3.3}$$

The layer boundaries and corresponding parameters a_i, b_i and c_i are given in table 3.1. (The outermost layer in the US standard atmosphere in which $X(h)$ scales linearly with height has been omitted as we are not interested in processes above 100 km height.)

For the sake of completeness, the height as a function of atmospheric depth is then given by

$$h(X) = -c_i \log \frac{X - a_i}{b_i}, \tag{3.4}$$

and the density at a given atmospheric depth is inferred as

$$\rho(X) = \frac{(X - a_i)}{c_i}. \tag{3.5}$$

Finally, the Molière radius r_M is parametrised as (Dova et al. 2003)

$$r_\mathrm{M}(X) = \frac{9.6}{(X - a_i)} c_i. \tag{3.6}$$

3.3.5 Random number generation

An important centre-piece of any MC simulation is the random number generator at its heart. We revert to the well-known "Mersenne-Twister" random-number generator of Matsumoto & Nishimura (1998) in the C++ implementation by Fog (2003). Only one instance of the random number generator is used throughout the whole program to prevent potential problems with interfering multiple instances of random number generators (see section 3.6.2 for details).

If possible, the generators for non-uniform probability distributions were

implemented using analytic inversions. If not, we reverted to rejection methods.

3.4 Intelligent concepts

As mentioned earlier, a "brute-force" approach as sketched in the "recipe" given in section 3.2.2 involves such a high computational effort (both regarding CPU time and memory) that it simply is not feasible on standard PCs. One therefore has to employ a number of intelligent concepts to minimise the computing effort. The main ideas that we have explored to reach this goal are described in the following subsections.

3.4.1 Cutting off γ^{-1}-cones

The radiation pattern emitted by an individual highly relativistic particle is heavily beamed in the forward direction (see, e.g., Jackson 1975). Most of the emission is radiated into a cone with opening angle of order $\sim \gamma^{-1}$. This directly leads to a very simple, but effective idea of how to cut down on computing time:

For an individual particle flying on its given trajectory, the γ^{-1} emission cone sweeps over a relatively small region on the ground. It is only in this ground-region of a few times γ^{-1} "width", which we call the "ground-trace" of the particle trajectory, that receives considerable contributions of radiation from that particle. Thus, we can select only the ground-bins inside the ground-trace of this specific particle for evaluation as sketched in figure 3.1, hugely cutting down on computing time.

It turns out, however, that the discrete cutting off after a certain angular distance introduces errors in the calculation, which are — although only at a percent-level — significant when one is interested in the emission strength at distances a few hundred metres from the shower core. We will discuss the details in section 3.6.5.

3.4.2 Smart trajectory-sampling

In general, there are two approaches of how to calculate the time-dependence of the emission that a specific ground-bin receives from a given particle:

The first approach is to take the trajectory of a given particle, sample it in a sufficient number of points and calculate the corresponding contributions for the given ground-bin using (3.1). If the particle trajectory is sampled in equidistant time-steps, the retardation effects involved lead to a *non-*

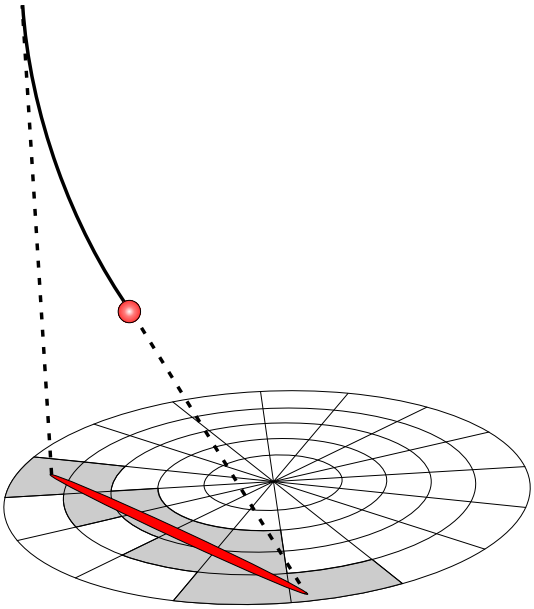

FIGURE 3.1—Cutting off γ^{-1}-cones: only bins in the "ground-trace" of a particle's trajectory are selected for evaluation.

equidistantly sampled time-series for the ground-bin. The heavily-peaked pulse shape is, however, *automatically* sampled with high precision in this approach.

As the time-series data collected by the ground-bin have to be gridded eventually, it would be easier if one could take another approach: taking the ground-bin's pre-defined equidistant time-grid and sampling the particle trajectory in the points corresponding to this grid. This, however, is not easily possible because of the "recursive" retardation relation (3.2). One would have to do an iterative search for the corresponding points on the particle trajectory, which would be at least as time-consuming as interpolating or binning a non-gridded time-series derived with the first approach to the ground-bin's time-grid. At the same time, this approach bears the risk of missing highly peaked contributions in case of a too widely spaced time-grid.

The first approach, therefore, is the better choice for our calculations. It is, however, possible to improve on the case of equidistant sampling of the particle trajectory by taking advantage of the strong beaming of the emission once again. The peaks in the time-series result when the denominator $(1-\boldsymbol{\beta}\cdot\boldsymbol{n})^3$ in (3.1) gets small as the angle between $\boldsymbol{\beta}$ and $\boldsymbol{n}$ gets small. It therefore makes sense to densely sample the region of small angle to the line-of-sight, and increase the distance between the sampled points (up to a maximum value) as the angle gets larger. This minimises the number of points used while it guarantees high-precision sampling of the pulse shape as can be seen in figure 3.2.

Our algorithm for the smart trajectory sampling is implemented as follows: The trajectory of length l (in g cm^{-2}) is mapped onto the interval $d \in [0,1]$ with user-defined equidistant step-size Δd, defaulting to $\Delta d = l^{-1}$ g cm^{-2}. The minimum and maximum step-sizes are set to $\Delta d_{\min} = (1/3)\Delta d$ and $\Delta d_{\max} = (20/3)\Delta d$, respectively. When $\theta(d)$ denotes the angle between line-of-sight vector $\boldsymbol{n}(d)$ and instantaneous particle velocity vector $\boldsymbol{v}(d)$, and the particle gamma factor is γ, the dynamic step-size $\delta d(d)$ is then set to

$$\delta d(d) = \theta(d)^2\gamma^2\Delta d_{\min}, \tag{3.7}$$

but no less than $\Delta d_{\min}$ and no more than $\Delta d_{\max}$.

3.4.3 Intelligent gridding strategy

The individual particles' pulses are very short, of order 10^{-11} s for $\gamma = 60$ particles. Usually, however, one is only interested in the result on scales of

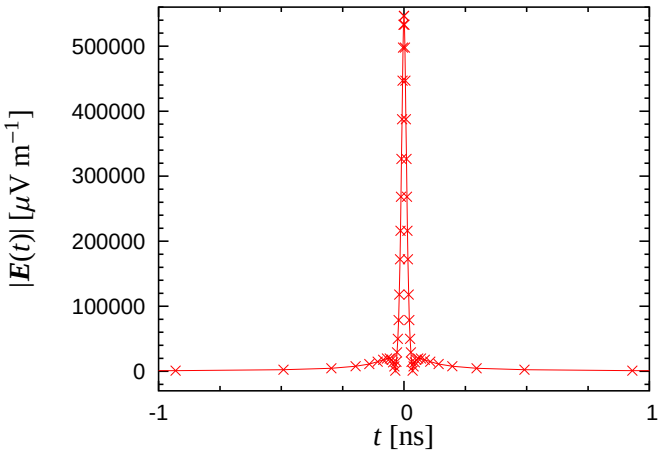

FIGURE 3.2—Smart trajectory sampling: the particle trajectory is sampled densely in the peak-region and only sparsely further outside.

several nanoseconds as defined by the interesting frequency range of tens to hundreds of MHz. On the other hand, it would be useful for diagnostic and verification purposes to have a means to record the events in the very high time-resolutions of the individual pulses. We have therefore implemented both possibilities into the simulation program. The different demands are met by the use of two very different gridding strategies.

The more efficient and thus favoured strategy for low time resolutions is the use of a "simple grid". It is based on an equidistant grid of user-defined resolution (typically ~ 1 ns). The contributions from a particle's time-series data are then binned and thus time-averaged onto the grid. The gridding is dynamic in the sense that data points are inserted automatically when needed. This saves memory in comparison with an ordinary equidistant grid. Still, this strategy does not scale well to high time-resolutions.

To counter the high memory demands for high time resolutions, we have implemented an "economic grid" which describes the pulse-shapes using only a minimum number of points. It is based on an underlying equidistant time-grid which limits the time-resolution to a pre-defined maximum value. The time-series of an individual particle is interpolated to the underlying grid positions and then incorporated into the pre-existing time-series, correctly interpolating any contributions that were already present. Points are, however, only

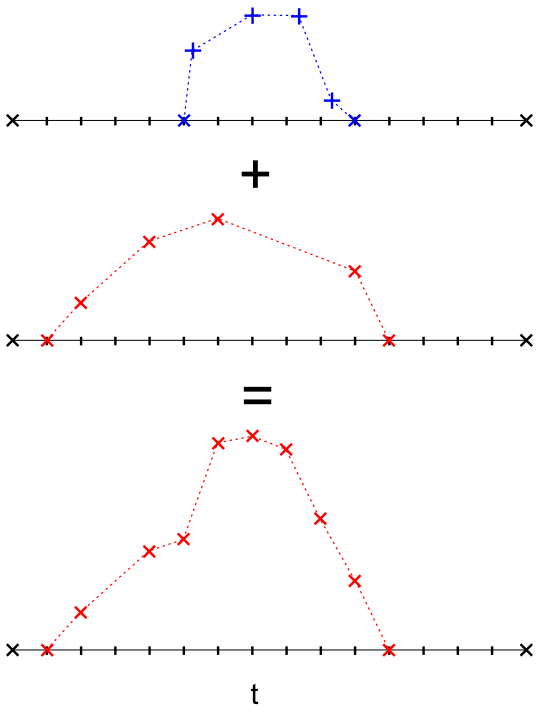

FIGURE 3.3—The economic gridding mechanism: when new contributions are registered onto existing contributions, points are inserted and interpolated only as needed.

inserted in the grid where necessary. See Fig. 3.3 for an illustration of the algorithm.

As another major advantage, the availability of these two very different gridding strategies allows an independent cross-check of their implementation.

3.4.4 Sequentialised and parallelised calculation

The program is designed such that calculations can easily be sequentialised or parallelised to cut down on memory requirements or take advantage of multiple computers, respectively.

Memory usage increases with the number of ground-bins to be calculated. To facilitate the use of low-memory machines, the calculation of ground-bins can be sequentialised: the emission from the complete shower is calculated for only a subgroup of ground-bins, and only after the calculation has finished and

the results have been written to disk, the next group of ground-bins is evaluated. This efficiently decreases the memory-usage as compared to concurrent evaluation of all ground-bins. The overhead introduced due to the necessary multiple creation of particle distributions is negligible for most combinations of parameters. Manually specifying the random seed value for the random number generator guarantees identical particle distributions in the different calculation segments. Allowing for different seed values in the calculations, on the other hand, provides a consistency check based on the underlying symmetries in the emission pattern as the different ground-bins are calculated based on independent sets of random numbers.

Similarly, different subgroups of the desired ground-area can be calculated in parallel on different computers, yielding up to a linear decrease of net computation time.

3.4.5 Automatic ground-bin inactivation

As the simple discrete cutting off of regions outside the $\sim \gamma^{-1}$ ground-trace region described in section 3.4.1 introduces errors that are too big if one is interested in regions of a few hundred metres distance to the shower core, we developed a more sophisticated means of cutting down on computation time.

Since most of the particles are distributed in the innermost centre-region of the shower, the ground-bins close to the centre-region receive a high number of strong contributions, whereas the far-away regions only receive a smaller number of not-so-strong contributions. While the centre-regions might already have reached sufficient precision after a certain number of particles, the outer regions might still not have reached the desired statistical precision, affording a calculation with an even higher number of particles.

The computing time can be distributed in a much more efficient way by an on-the-fly inactivation of ground-bins that have reached the desired precision. To accomplish this, the program evaluates the shower emission in steps of (typically) 10,000 particles at a time. After each of these steps it compares the (smoothed) time-series derived for a specific ground-bin up to that stage with the results for that ground-bin at the previous step. Once the relative changes fall under a pre-defined limit for a user-defined number of steps in a row, the corresponding ground-bin is marked as “inactive” and is not evaluated any further. The computing time is thus effectively redistributed to the outer bins.

The fact that the inactivation sequence should propagate from the inner to the outer regions is used as a consistency check for the procedure. Another advantage is that the user can directly specify a desired precision rather than

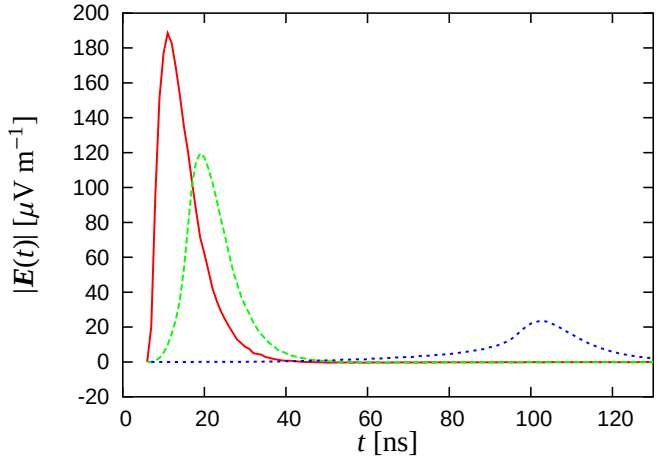

FIGURE 3.4—Time-dependence of the raw pulses originating from the shower maximum as observed by an observer at (from left to right) 20 m, 140 m and 460 m to the north from the shower centre.

having to estimate the number of particles needed to reach adequate results.

3.5 Data output and reduction

To facilitate the understanding of the following discussions, we give a short overview of the raw data that the simulations produce and the kind of data "reduction" that we apply to visualise the results.

3.5.1 Raw data

The Monte Carlo code tracks the individual particles and calculates the associated (vectorial) electromagnetic pulses a specific observer (i.e., a specific ground-bin) receives. The individual pulses are extremely short, of order a few 10^{-11} s (cf. Fig. 3.2). Superposition of all the individual pulses yields the raw output of the program: one data file per ground-bin stating the time-dependence of the north-south, east-west and vertical polarisation components of the electric field. Fig. 3.4 shows the total field strength of the raw pulses at different distances to the north from the centre of a shower slice consisting of 10^8 particles in the shower maximum. Due to the particle's spread in position and time, the pulses are considerably broader than the individual pulses, of order tens of nanoseconds. A helper application is then used to process these

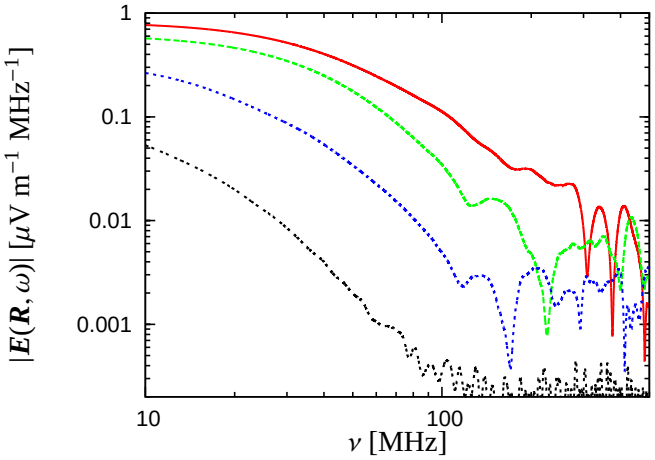

FIGURE 3.5—Spectra of pulses originating from the shower maximum for observers at (from top to bottom) 20 m, 140 m, 340 m and 740 m distance to the north of the shower centre.

raw data and reduce them to the desired physical quantities.

3.5.2 Spectral filtering

In a first step, the time-series data of the electric field vector is Fourier-transformed, yielding the associated spectrum depicted in Fig. 3.5. Due to coherence losses caused by interference effects, the spectra fall off steeply towards high frequencies. At a certain frequency, dependent on the distance from the shower centre, the field strength reaches a first interference minimum followed by a rapid series of alternating maxima and minima in the incoherent regime. Insufficient sampling of these extrema yields the unphysically seeming features seen here at high frequencies. In the emission from a real air shower such features are unlikely to exist as the inhomogeneities present in an air shower, but not taken into account in the analytic parametrisations, destroy the pronounced extrema. Calculation of the emission in this region therefore requires a more detailed air shower model, e.g. by interfacing of our code to CORSIKA.

Any concrete experiment will have a finite frequency bandwidth. Thus, we filter the spectra to infer the actual pulses that the experiment will register. As is obvious from the spectra, most of the power resides at the low frequencies. For this reason the amplitude drops significantly when filtering frequencies

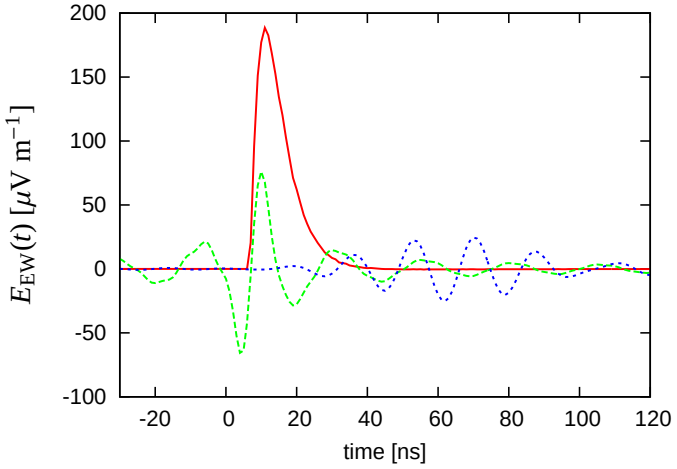

FIGURE 3.6—Comparison of the east-west component of a raw pulse (solid), a pulse smoothed with a 40–160 MHz idealised rectangle filter (long dashed) and a 42.5–77.5 MHz filter as used in LOPES (short dashed) for emission from the shower maximum.

below, e.g., 40 MHz as seen in Fig. 3.6.

Here we have used the same idealised 40–160 MHz filter that we applied in the theoretical calculations of chapter 2 as well as the actual 42.5–77.5 MHz filter that is used in LOPES. The acausality of the pulse filtered with the idealised rectangle filter illustrates that such a filter is an unphysical concept. A physical filter does not show acausal behaviour despite its steep edges as it delays the signal appropriately. This is well visible for the LOPES filter.

3.5.3 Further data processing

To analyse the radial dependence of the emission strength, we then determine the maximum amplitude of the filtered pulse in each ground-bin. The dependence of this "filtered pulse maximum amplitude" can then be visualised in a number of ways, e.g., as surface plots, contour plots or cuts in specific directions (see the following sections for examples). The absolute time associated to the maximum pulse amplitude additionally yields information about the curvature of the radio wave front.

One subtlety involved with this procedure is the noise levels present at high radial distances. As can be seen in Fig. 3.4, the pulses get significantly broader as one goes to higher distances. (This effect gets even stronger for fully in-

tegrated showers.) At distances of several hundred metres, the pulses are so broad that a filter clipping frequencies below ~ 40 MHz actually resolves the pulses out. Consequently, the pulse amplitude drops to very low values comparable to those introduced by the higher-frequency numerical noise associated with the very short individual particle pulses. Taking the maximum amplitude as a measure for the emission strength then might no longer constitute a useful procedure. Calculating the time-integral of the field strength or the received power would be a better approach in these cases. We are, however, mostly interested in the emission strengths up to radial distances of ~ 500 m, where the filtered pulse amplitude gives adequate results which are directly related to the experimentally relevant signal-to-noise levels.

For the diagnostics of the employed algorithms in section 3.6 and the analysis of track length effects in section 3.7.1 we therefore adopt 800 m as a cutoff distance. For the calculation of emission strengths from a shower slice and an integrated shower, we limit the plots to distances of ~ 550 m and ~ 400 m, respectively, to insure that the filtered pulse amplitudes give adequate results which are directly related to the experimentally relevant signal-to-noise levels.

3.6 Consistency checks

We have studied the output of our MC code very carefully to make sure that the calculations are correct. In particular, we have made the following consistency checks:

3.6.1 Individual particle pulses

Figure 3.7 shows the comparison between an analytical calculation and our MC code for a pulse created by a point-source consisting of 10^8 particles with $\gamma \equiv 60$ at 4 km height, comparable to a pulse that would originate from the maximum of a vertical 10^{17} eV air shower concentrated into a point, as seen from an observer in the shower centre. The magnetic field is adopted as horizontal with a strength of 0.3 Gauss. The good agreement between the MC and analytic results demonstrates that the calculation of the particle trajectories and emission contributions is implemented correctly.

It should be noted that the pulse length usually stated in textbooks such as Rybicki & Lightman (1979) (equation 6.10a)

$$\Delta t^A = \frac{2}{\gamma \omega_B \sin\alpha} \left(1 - \frac{v}{c}\right) \tag{3.8}$$

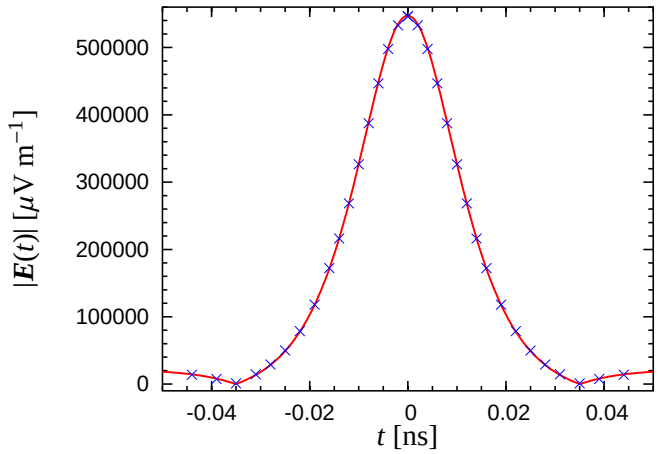

FIGURE 3.7—Total field strength of a pulse originating from a point source of 10^8 $\gamma = 60$ particles in 4 km height, observed in the shower centre. Solid: analytic calculation, points: calculated with MC code.

is in itself already an approximation which yields values that are significantly too low. This results from an implicit approximation $sin(\theta) \approx \theta$ in the derivation of the formula. The correct result is

$$\Delta t^A = \frac{2}{\gamma \omega_B \sin\alpha}\left(1 - \frac{v}{c}\gamma \sin\frac{1}{\gamma}\right). \tag{3.9}$$

Figures 3.8 and 3.9 demonstrate how the pulses from the same point-source change when the observer moves outwards from the shower centre to the north and east, respectively. While the pulse amplitude drops quickly when one goes to the north, it stays fairly constant as one goes to the east. This effect was already discussed under the term "reduced θ" in chapter 2: The particle trajectory bends towards an observer in the east or west, so that he or she still sees the particle with a very small angle to the line of sight — just during a different part of the trajectory. For the specific geometry chosen in this example, i.e. a particle pair starting off vertically downwards in the shower centre, the pulses even get broader as one goes outwards to the east, since one only sees an (asymmetric) half pulse in the centre and can see the full (symmetric) pulse only at considerable distance. All in all the behaviour is exactly as expected.

Another important consistency check is the dependence of the individual

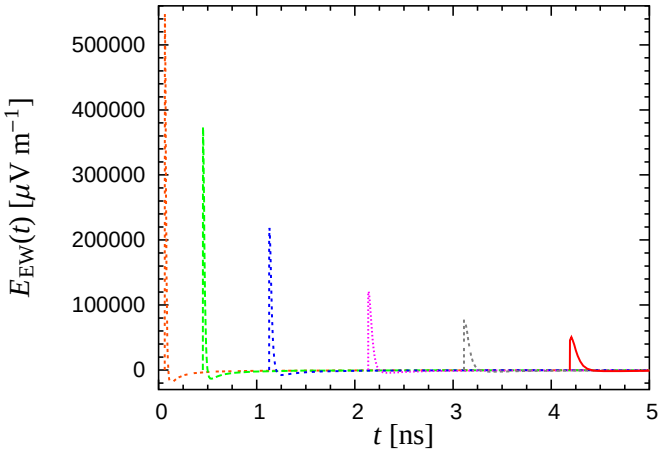

FIGURE 3.8—East-west polarisation component of a point-source with $\gamma = 60$ particles at 4 km height at increasing distance *to the north* from the shower axis. From left to right: 5 m, 305 m, 505 m, 705 m, 855 m and 995 m.

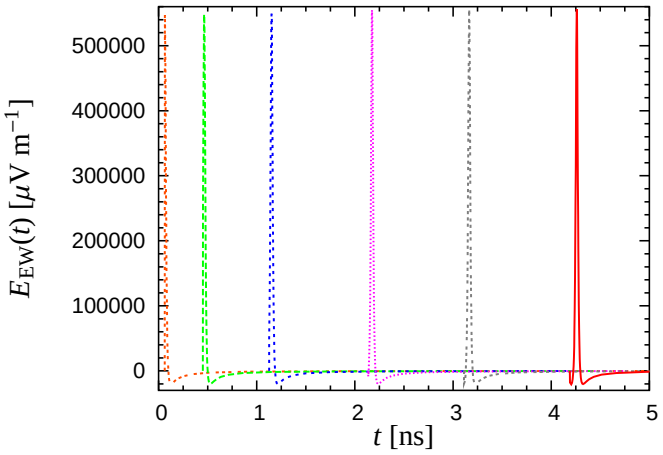

FIGURE 3.9—Same as fi gure 3.8 at increasing distance *to the east* from the shower axis.

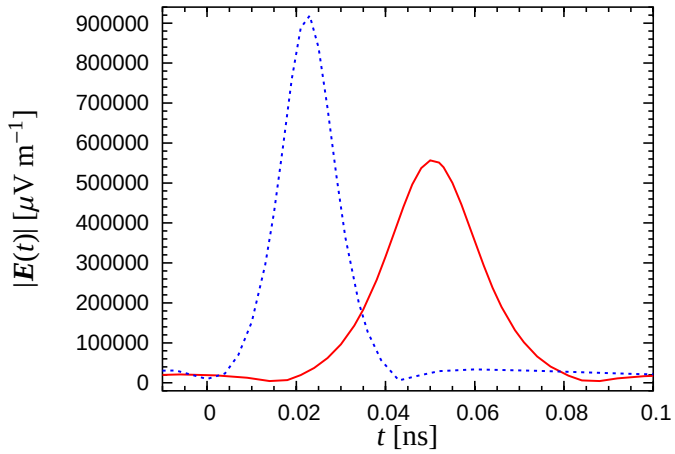

FIGURE 3.10—Individual particle pulses from a point-source shower as measured by an observer situated 995 m east of the shower centre. Solid: $B = 0.3$ Gauss, dashed: $B = 0.5$ Gauss. The time-integral over the pulses is constant.

pulses on the magnetic field strength. Figure 3.10 shows the changes arising when the magnetic field is enhanced from 0.3 Gauss to 0.5 Gauss (both with 0° inclination, i.e. horizontal). The pulse gets stronger, yet at the same time shorter so that the integral over $E\,\mathrm{d}t$ stays constant (while the power an observer receives from an individual particle, i.e. the integral over $E^2\,\mathrm{d}t$, thus scales linearly with B), exactly as inferred from analytic calculations. This directly leads to an important result: The overall radio emission from an air shower cannot depend strongly on the magnetic field strength, as it is the sum of a great number of individual pulses, the integral of each of which is independent of the value of B. Likewise, asymmetries between north and south that are introduced by a realistically inclined magnetic field cannot be very strong.

The fact that the 0.5 Gauss pulse arrives earlier than the 0.3 Gauss pulse for an observer 995 m to the east of the centre is explained by the stronger curvature of the particle trajectory.

3.6.2 Symmetry N-S and E-W

For a vertical air shower, the emitted radiation pattern must have a number of inherent symmetries. In particular, the east and west directions are completely equivalent (as long as particle track lengths for electrons and positrons are

adopted as identical), so that the emission pattern must be symmetric in east and west. For a horizontal magnetic field, north and south must also be equal.

Exploiting these fundamental symmetries, we discovered a subtle bug in an early version of the code. It turned out that the pulses in the east were actually different from the ones in the west, as well as north was different from south. This led us to the conclusion that the random number generation itself was flawed in the sense that it introduced an artificial correlation between the longitudinal and the azimuthal distribution. In fact, the seed values for the multiple instances of random number generators that were used at this stage in the code were chosen by an unsuitable routine that set all seeds to the same value (time in seconds since a given date). After having changed the program such that only one instance of the RNG is used for the entire simulation, the intrinsic symmetries were fulfilled as expected.

Needless to say that one can also use the intrinsic symmetries to save computation time by calculating only a half- or even quarter-plane on the ground and then mirroring the results accordingly.

3.6.3 Gridding algorithms

As explained in section 3.4.3, we have implemented a “simple grid” for low time-resolution calculations as well as an “economic grid” for cases in which the user is interested in the full time-resolution associated to the individual particle pulses.

The independence of the two algorithms allows a cross-check of the routines. Fig. 3.11 shows the raw pulse as calculated with the different gridding strategies at different time resolutions. The result is consistent between all three cases, which demonstrates that both algorithms work well. The “simple grid” proves to be very efficient at low time-resolutions (typically ~ 1 ns). It is especially robust in the sense that it remains stable regardless of the specific resolution used. The “economic grid” on the other hand has to be set to a time-resolution high enough to resolve the individual particle pulses. Especially when particle energy distributions are switched on, introducing very high-energy particles with up to $\gamma = 1000$, this strategy quickly becomes inefficient.

Additionally, low time-resolution “simple grid” data yields smoother pulses due to the time-averaging over the individual particle pulses, which allows precise calculations with fewer particles.

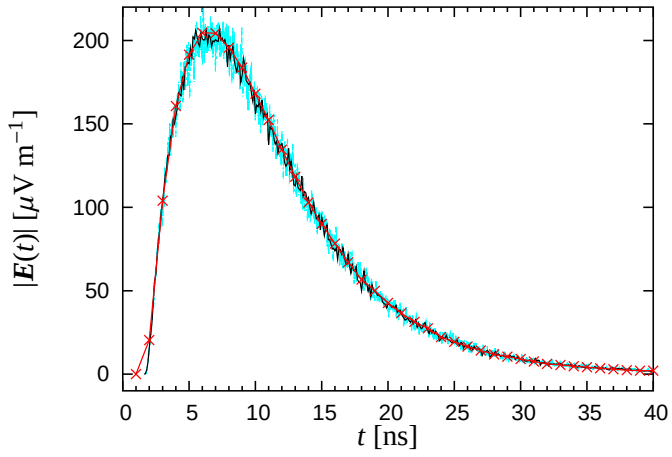

FIGURE 3.11—Raw pulse from a shower slice calculated with different gridding strategies and resolutions. Solid with points: simple grid 10^{-9} s, solid black: simple grid 10^{-10} s, light coloured: economic grid 10^{-12} s.

3.6.4 Smart trajectory-sampling

Figure 3.12 demonstrates that the errors introduced by the smart sampling algorithm are only slight. At the same time, the algorithm allows a huge cut-down on computation time. The algorithm can, however, optionally be switched off for a more precise calculation.

3.6.5 Cutting off γ^{-1}-cones

As mentioned earlier, the discrete cutting off of radiation contributions outside the ground-trace of a few γ^{-1}-cones width can decrease the computation time enormously. Figure 3.13, however, demonstrates that this strategy is not suitable if one needs precision at the percent-level to be able to describe the emission pattern out to distances of several hundred metres from the shower centre.

The discrete cutting introduces “breaks” in the radial emission pattern exactly at the positions corresponding to the cutoff, i.e. at $\approx$ 530 m in case of 8 γ^{-1}-cones and $\approx$ 270 m in case of 4 γ^{-1}-cones for $\gamma = 60$ particles at 4 km height. The effect is less strong in the east-west direction, but overall this strategy is disqualified for high-precision calculations.

The problems are resolved by the more sophisticated on-the-fly inactiva-

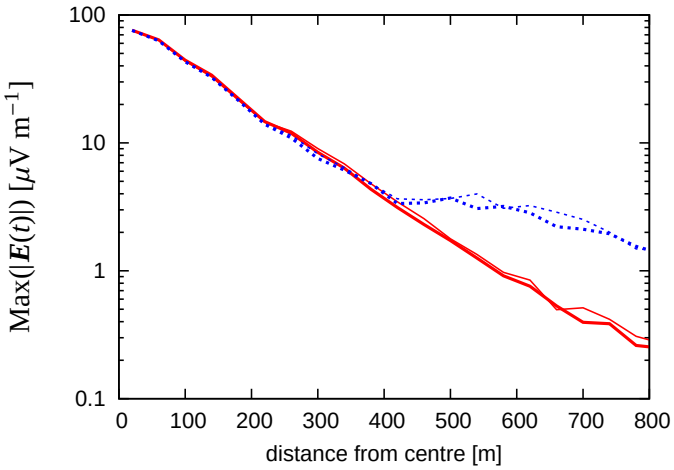

FIGURE 3.12—Changes introduced by the smart sampling algorithm in the radial emission pattern of the rectangle-filtered maximum pulse amplitude for emission from the shower maximum. Thin lines: dense equidistant sampling, thick lines: smart sampling; solid: to the north, dashed: to the west.

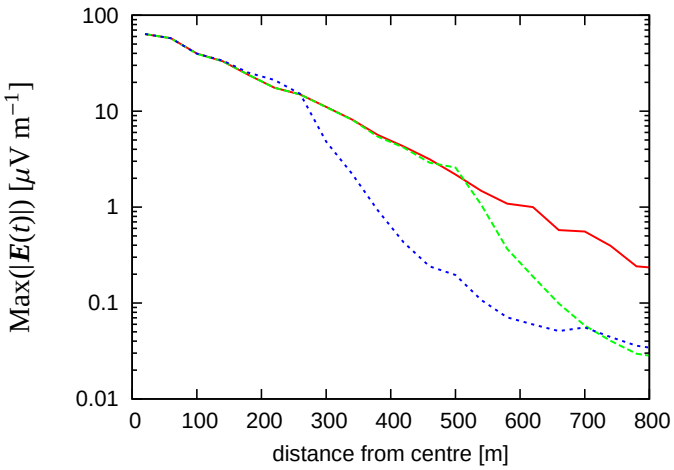

FIGURE 3.13—Changes introduced by the cutting off of regions outside a few γ^{-1}-cones in the radial emission pattern of the frequency-filtered maximum pulse amplitude for emission from the shower maximum. Distance from the shower centre is to the north. Solid: no cutting, long dashed: cutting after 8 γ^{-1}, short dashed: cutting after 4 γ^{-1}

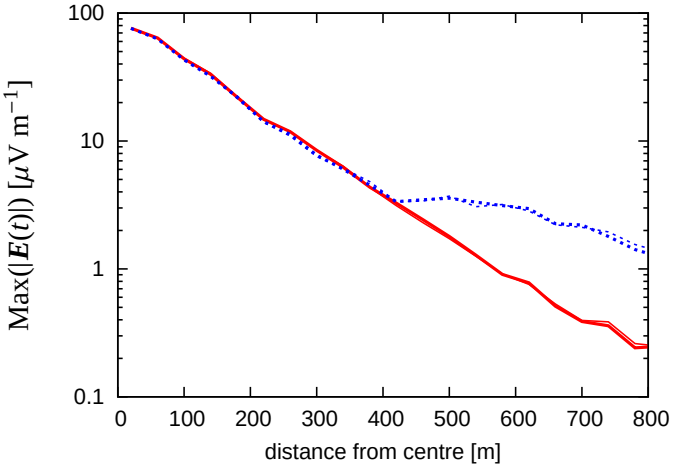

FIGURE 3.14—Changes introduced to the radial emission pattern of the frequency-filtered maximum pulse amplitude for emission from the shower maximum by the automatic bin inactivation algorithm. Thin lines: no automatic bin inactivation, thick lines: automatic bin inactivation; solid: to the north, dashed: to the west.

tion of ground-bins.

3.6.6 Automatic ground-bin inactivation

Fig. 3.14 demonstrates the stability of the automatic ground-bin inactivation algorithm. The calculations are as precise as those with a fixed high number of particles for all ground-bins, yet at the same time allow a much more efficient use of computing time and the definition of a user-specified precision goal. The deactivation sequence propagates from the inside to the outside as expected (see Fig. 3.15). It is also no surprise that the bins in the far east and west require the most computing time, as these are the regions that are influenced most by edge effects from trajectory cutoffs, different trajectory curvatures and the like. The automatic ground-bin inactivation strategy therefore turns out to be a very powerful and self-consistent technique to conduct extensive simulations with high precision.

3.7 Emission from a shower slice

Similar to the analytical calculations described in chapter 2, we first take a look at the emission from a single “slice” of the air shower. Throughout this section,

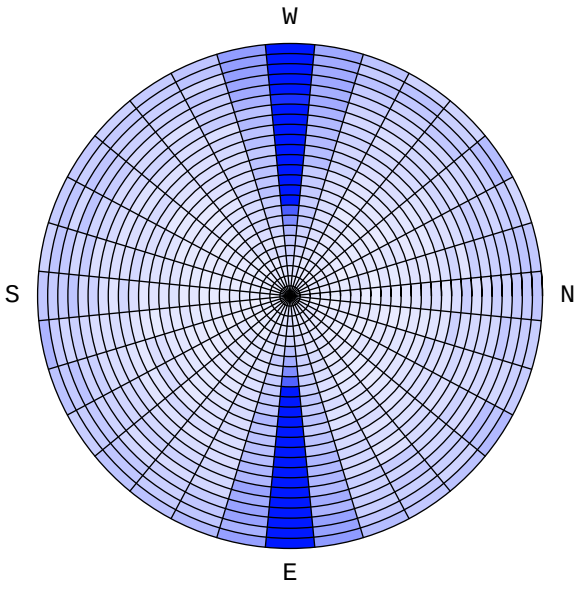

FIGURE 3.15—Automatic ground-bin inactivation sequence. Darker bins are set inactive later than lighter bins. The sequence propagates from the inside to the outside. The pattern is east-west and north-south symmetric as expected for a vertical shower and a horizontal magnetic field.

we consider only the maximum of a vertical air shower induced by a 10^{17} eV primary particle, consisting of 10^8 charged particles at a height of 4 km. In a step by step analysis, we increase the complexity of the particle distributions and evaluate the changes introduced in the simulation results.

3.7.1 Trajectory length effects

In a first step, we adopt the geomagnetic field parallel to the ground with a strength of 0.3 Gauss, as it is present at the equator. This is the same configuration that we used in the theoretical calculations. For the moment, we consider the simplified case of monoenergetic $\gamma \equiv 60$ particles.

The theoretical calculations carried out in chapter 2 were based on an analytical derivation of the spectra of individual particles on circular trajectories. This derivation makes the implicit assumption that the trajectory is always symmetric with respect to the point in which the minimum angle θ to the observer's line of sight is reached. In other words, edge effects arising from the cutting off of the finite trajectories are not taken into account.

These edge effects, however, turn out to significantly shape the radial emission pattern of the radiation. Let us first consider the case of trajectories which are long enough to not produce significant edge effects for observers far away from the shower centre by adopting a trajectory length of 100 g cm^{-2}. The result is depicted in Fig. 3.16. As expected, it is very similar to the theoretical prediction for the "reduced θ" case presented in Fig. 2.14. In this scenario, one would expect a significant asymmetry between the north-south and east-west direction, which would obviously be a very useful observable.

What happens, however, if one adopts more realistic particle track lengths? Let us first consider a constant trajectory length of 40 g cm^{-2}, which is approximately the free path length (equal to one radiation length) of electrons and positrons in air (Allan 1971). In this scenario, edge effects strongly shape the emission at high distances in the east-west direction as shown in Fig. 3.17. An unusual "kink" appears at $\sim$540 m. This is not a numerical glitch, but an interference effect arising when the observer stops to see the main (positive) peak of the individual particle pulses due to the edge effects. He then only receives the initial (negative) contribution of the electric field pulse. This effectively causes a polarity change in the raw pulses as shown in Fig. 3.18, accompanied by a temporary drop in the filtered pulse amplitude.

Finally, we change to a realistic exponential distribution of track lengths

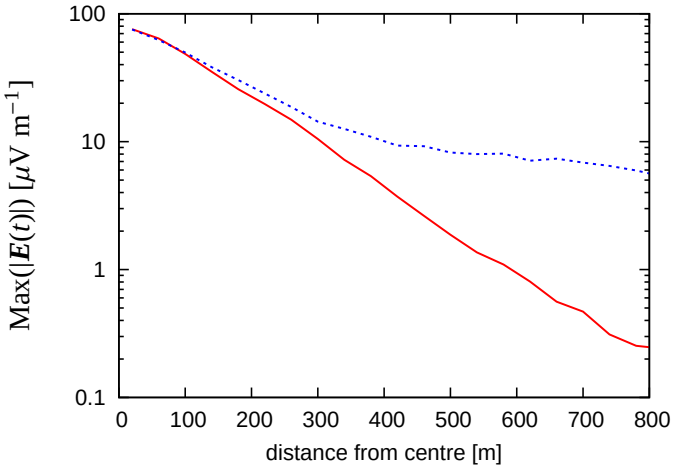

FIGURE 3.16—Radial dependence of the maximum rectangle-filtered pulse amplitude for emission from the shower maximum in the north (solid) and west (dashed) direction in case of constant and long particle trajectories ($\lambda \equiv 100$ g cm^{-2}, no edge effects at high distances from the shower centre).

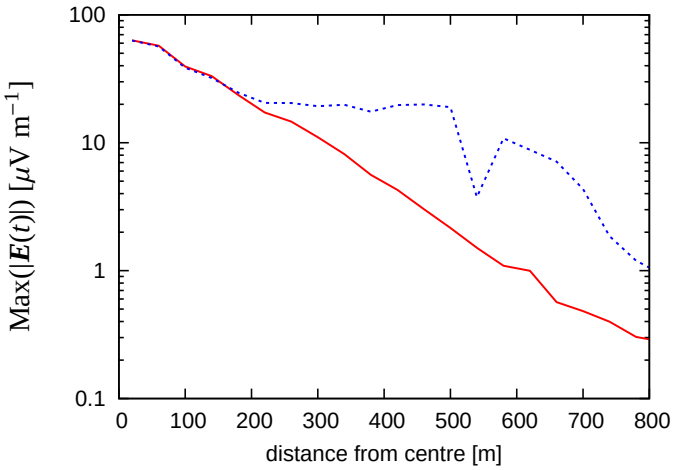

FIGURE 3.17—Same as Fig. 3.16 for $\lambda \equiv 40$ g cm $^{-2}$. See text for explanation of the "kink" at ~540 m.

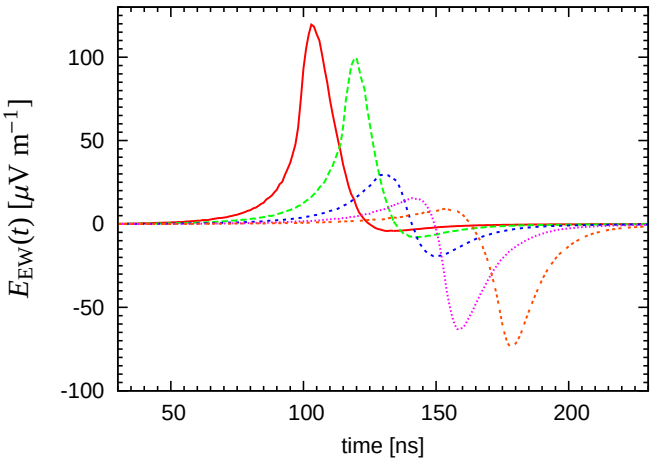

FIGURE 3.18—Time-dependence of the raw pulses originating from the shower maximum as observed by an observer at (from left to right) 460 m, 500 m, 540 m, 580 m and 620 m to the west from the shower centre. See text for explanation of the "polarity change".

with a mean of $\lambda = 40$ g cm^{-2},

$$p(X) = p_0 \ \exp\left(-\frac{X}{\lambda}\right). \tag{3.10}$$

As can be seen in Fig. 3.19, the asymmetry between north-south and east-west direction is now washed out up to high distances. (In fact, it will be washed out almost completely once the integration over the shower evolution is taken into account.)

Apart from the regions far from the shower centre, edge effects also occur in the centre region due to the instantaneous starting of the trajectories. These effect are discussed in section 3.7.4.

The significance of the trajectory length effects already illustrates the importance of adopting as realistic properties for the particle distributions as possible, a goal that could not be reached with analytic calculations alone. We retain the realistic statistical distribution of track lengths for the following discussions of the magnetic field and energy distribution effects.

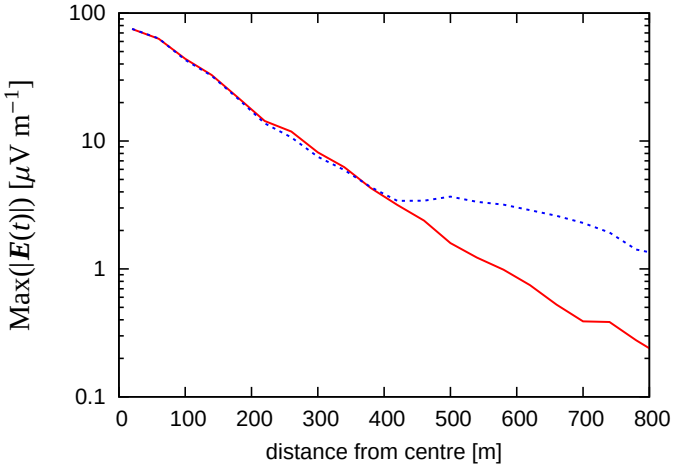

FIGURE 3.19—North (solid) vs. west (dashed) asymmetry in the maximum filtered pulse amplitude for emission from the shower maximum in case of statistically distributed track-lengths. The asymmetry is washed out up to high distances.

3.7.2 Magnetic field dependence

We now make the change from an equatorial 0.3 Gauss horizontal magnetic field to the 0.5 Gauss 70° inclined magnetic field present in central Europe. As explained in Sec. 3.6.1, the influence of the magnetic field on the integrated shower pulse should not be very significant. This is confirmed by Fig. 3.20. Although the projected magnetic field strength drops from 0.3 Gauss to 0.17 Gauss, the emission pattern only changes very slightly. In particular, the amplitude level stays almost constant. Interestingly, the north-south vs. east-west asymmetry is washed out even further.

On the other hand, the inclination of the magnetic field breaks the intrinsic north-south symmetry of the emission pattern. This is visible in the north-south and east-west polarisation components of the contour plots shown in Fig. 3.21. Similarly, the symmetry of the ground-bin inactivation sequence is broken as shown in Fig. 3.22. The effect is, however, only weak and there is still no asymmetry if one considers the total electric field strength rather than a specific polarisation direction.

Note that there is no significant emission in the centre region of the north-south polarisation component (second column of Fig. 3.21). This demonstrates that the numerical cancellation of north-south polarised radiation components

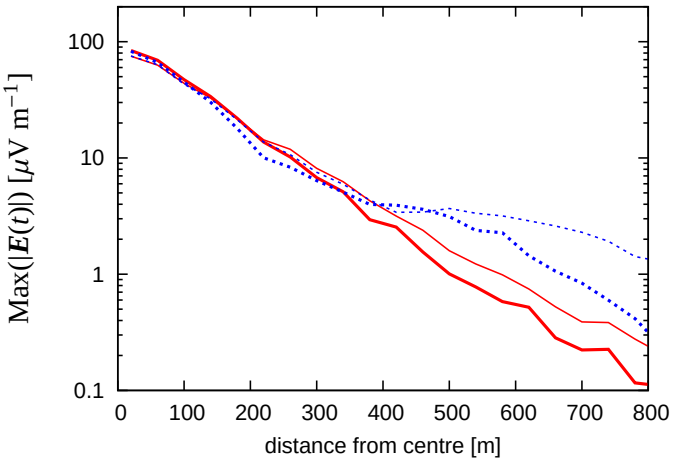

FIGURE 3.20—Changes to the north (solid) and west (dashed) radial emission patterns for emission from the shower maximum when going from a 0.3 Gauss horizontal magnetic field (thin lines) to a 70° inclined 0.5 Gauss magnetic field (thick lines).

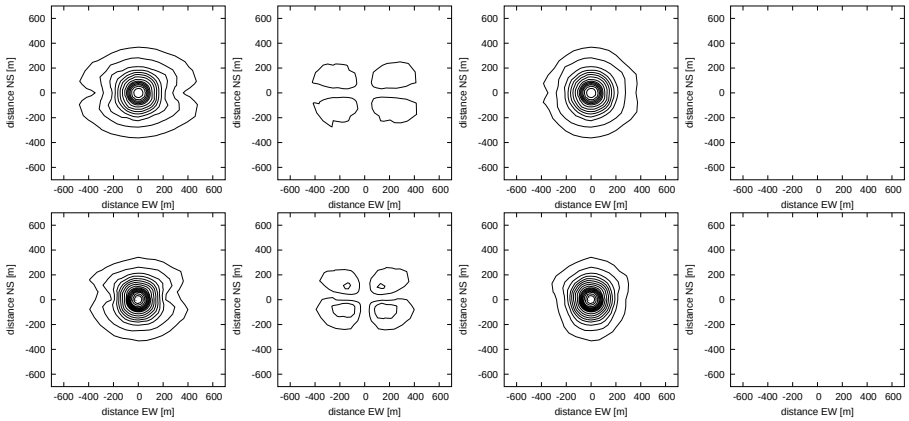

FIGURE 3.21—Contour plots of the 40–160 MHz rectangle-filtered maximum pulse amplitude for emission from the shower maximum in case of a horizontal 0.3 Gauss magnetic field (upper panel) and a 70° inclined 0.5 Gauss magnetic field (lower panel) and $\gamma \equiv 60$ particles. Contour levels are 5 μV m^{-1} apart. From left to right: total electric field strength, north-south polarisation component, east-west polarisation component, vertical polarisation component.

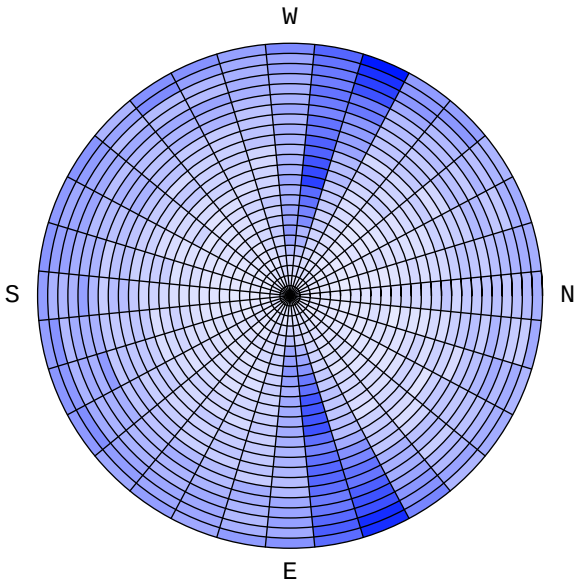

FIGURE 3.22—Automatic ground-bin inactivation sequence in case of 70 ° inclined 0.5 Gauss magnetic fi eld. The north-south symmetry is broken as expected, cf. Fig. 3.15.

from the electrons and positrons (labelled $A_\perp$ in chapter 2) indeed works correctly in the MC code and that it was justified to neglect this component in the earlier theoretical calculations at least for the primarily important centre region.

In summary, the magnetic field effects are weak, but non-trivial.

3.7.3 Energy distribution effects

In the theoretical calculations, a change from monoenergetic $\gamma \equiv 60$ electrons to a broken power-law peaking at $\gamma = 60$ introduced only minor changes, namely a slight redistribution of radiation from medium distances to the centre region (due to the high-energy particles) and high distances (due to the low-energy particles). The changes introduced by the energy distribution are bound to be more complex in the MC simulations, as they are heavily intertwined with the edge effects discussed before. Nonetheless, a similar redistribution of radiation from the medium scales to the innermost centre region is observable in the MC simulations as shown in Fig. 3.23.

The drop visible in the west direction at $\sim$ 200 m arises due to a tran-

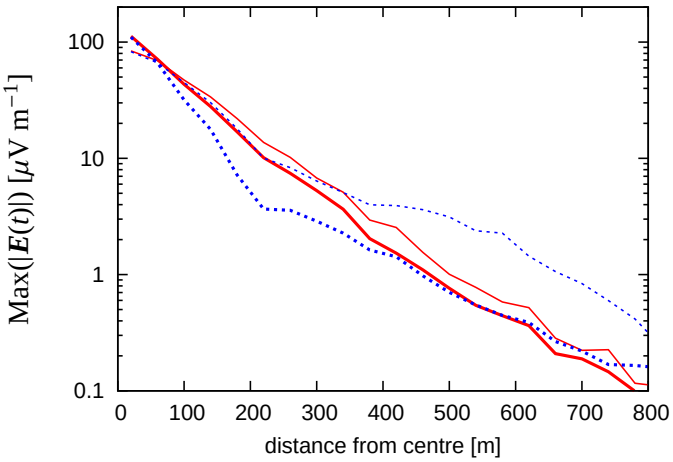

FIGURE 3.23—Changes introduced when switching from monoenergetic $\gamma \equiv 60$ particles (thin lines) to a broken power-law peaking at $\gamma = 60$ (thick lines) for emission from the shower maximum. Solid: to the north, dashed: to the west. See text for explanation of the drop at ~ 200 m.

sition from a dominating east-west polarisation component to a dominating north-south polarisation component in combination with some resolving out of pulses due to the filter bandwidth used. (Fig. 3.21 demonstrates that the north-south and east-west polarisation components become comparable at these distances.)

It should be pointed out, however, that the strength of the effects introduced by the choice of a specific energy distribution seem misleadingly strong when one considers the emission from a single shower slice alone. Once the integration over the shower evolution as a whole is performed, most effects (including the drop at ~ 200 m) are again washed out almost completely and the influence of the specific choice of energy distribution becomes very weak. For the moment, we therefore continue to use the broken power-law distribution that we adopted in the theoretical calculations rather than implementing a more realistic distribution such as the one given by Nerling et al. (2003).

The result that we have reached so far is the emission from the maximum of a 10^{17} eV air shower consisting of 10^8 electrons and positrons at a height of 4 km, taking into account adequate spatial, energy and trajectory length distributions and a magnetic field as present in central Europe. It is illustrated once more as a surface plot in Fig. 3.24.

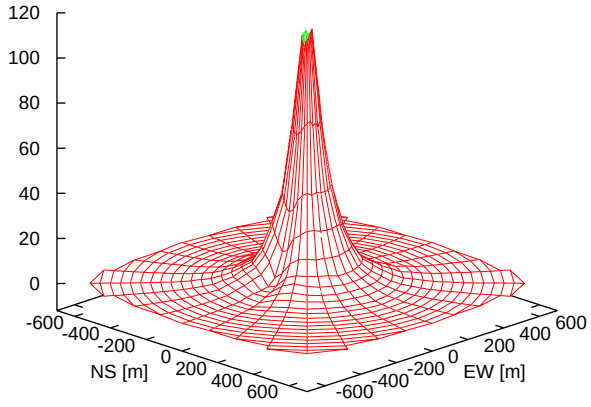

FIGURE 3.24—Pattern of the maximum filtered electric field amplitude (in μV m^{-1}) emitted by the maximum of a 10^{17} eV air shower consisting of 10^8 particles at a height of 4 km for a 0.5 Gauss 70° inclined magnetic field, a broken power-law particle energy distribution and a statistical distribution of track lengths.

3.7.4 Comparison with theoretical calculations

As shown in Fig. 3.7 the individual particle pulses calculated with our MC code are consistent with the results of the analytic calculations. The analytic pulses are symmetric because the particle trajectories are implicitly adopted symmetric to the point of smallest angle to the line of sight — the analytic calculations do not consider edge effects associated with the finite lengths of the trajectories. When one takes into account the cutting off of the trajectories correctly in the MC calculations, an observer in the centre region only sees half of the symmetric pulse for each individual particle (cf. Fig. 3.9).

In section 3.6.1 we discussed that the time integral over the individual particle pulses is the quantity relevant for the overall pulse as integrated over the shower as a whole. For simple geometries such as a point source or a line charge, the change from the symmetric to the half pulses should therefore produce a drop in the overall pulse amplitude (and the overall pulse spectrum) by a factor ~ 2. (For more complex shower geometries or at higher distances from the shower centre the changes introduced by the edge effects are non-trivial but still important as already discussed in section 3.7.1.)

Fig. 3.25 shows the direct comparison between the analytic and MC sim-

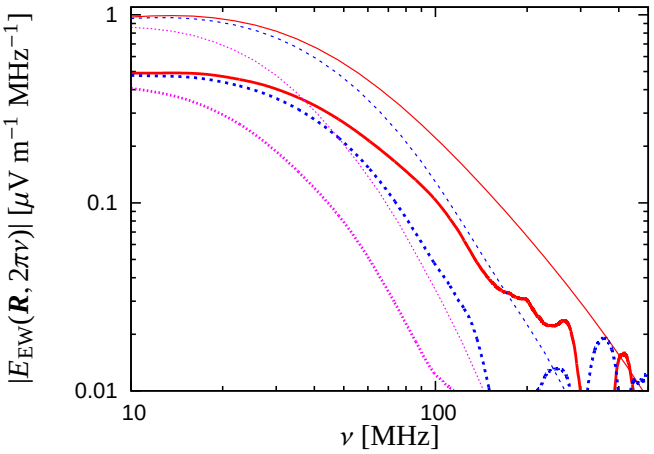

FIGURE 3.25—Spectra emitted by the maximum of a 10 ^{17} eV vertical air shower consisting of 10^8 particles with $\gamma \equiv 60$ at a height of 4 km, long (constant 100 g cm^{-2}), but not symmetric, particle trajectories and horizontal 0.3 Gauss magnetic field. Thin lines: analytic calculations from chapter 2, thick lines: these MC simulations. Solid: 20 m, dashed: 100 m, dotted: 260 m to north from shower centre.

ulated spectra emitted by a slice of monoenergetic $\gamma \equiv 60$ particles for the case of a horizontal 0.3 Gauss magnetic field and long (constant 100 g cm^{-2}), but not symmetric, particle trajectories. (Because the north-south polarisation component was neglected in the analytic calculations, we hereafter directly compare the east-west polarisation component.) This scenario allows a very direct comparison between the analytic and MC calculations, the only major difference being the edge effects introduced due to the non-symmetric trajectories. Consequently, the analytic spectra lie a factor ~ 2 above the MC results. Scaling down the analytic results by a factor of two shows indeed a very good agreement between the analytic and MC results as seen in Fig. 3.26. The radial dependence of the emission pattern, shown in Fig. 3.27, also shows good agreement between the MC and analytic calculations when one accounts for the systematic factor of two.

In a next step, we switch on the statistical distribution of trajectory lengths with a realistic mean free path length of 40 g cm^{-2}, adopt again a broken power-law distribution of particle energies and change to the realistic 70° inclined 0.5 Gauss magnetic field present in central Europe. In the analytic calculations, we switch on the broken power-law distribution, but cannot take into

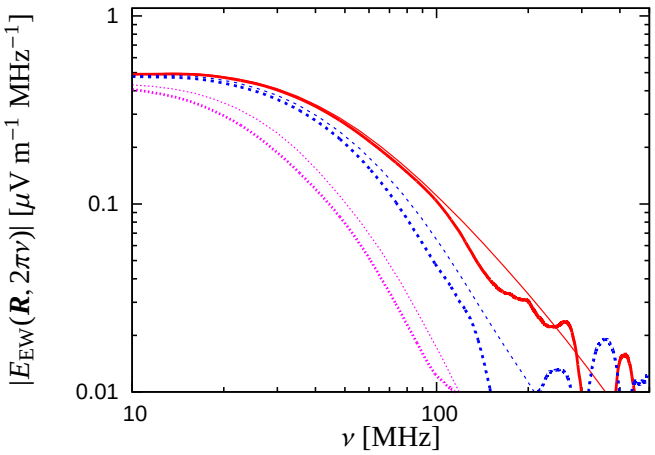

FIGURE 3.26—Same as Fig. 3.25 but scaling down the analytic results by a factor of two.

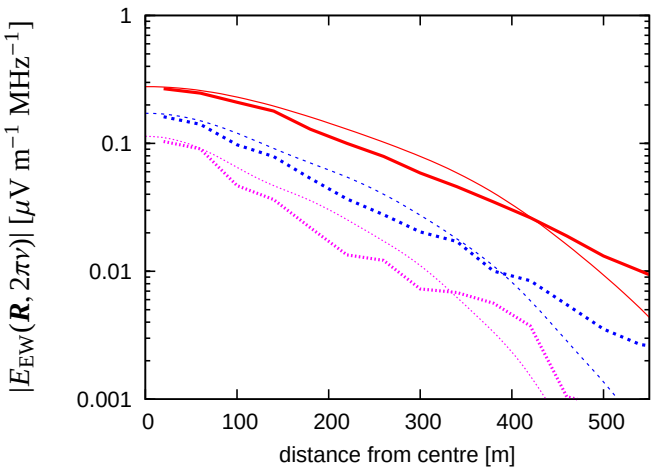

FIGURE 3.27—Radial dependence of the emission for the same scenario as in Fig. 3.25. Thin lines: analytic calculations from chapter 2 scaled down by a factor of two, thick lines: these MC simulations. Solid: ν = 50 MHz, dashed: ν = 75 MHz, dotted: ν = 100 MHz. Distance is to north from shower centre.

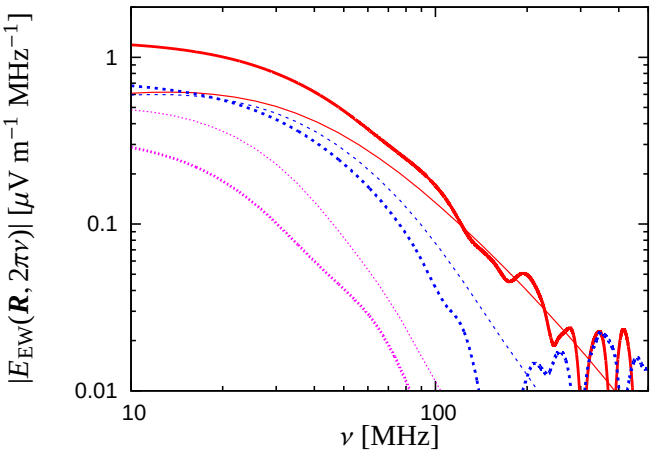

FIGURE 3.28—Spectra emitted by the maximum of a 10^{17} eV vertical air shower consisting of 10^8 particles with broken power-law energy distribution at a height of 4 km, statistically distributed particle trajectories with 40 g cm^{-2} mean path length and 70° inclined 0.5 Gauss magnetic field. Thin lines: analytic calculations from chapter 2 scaled down by a factor of two, thick lines: these MC simulations. Solid: 20 m, dashed: 100 m, dotted: 260 m to north from shower centre.

account the track length effects or the inclined magnetic field. Obviously, the results produced by the MC simulations in this scenario therefore cannot be expected to reproduce the analytic results equally well.

A direct comparison between the spectral dependences predicted by the analytic and MC calculations is shown in Fig. 3.28, keeping the down-scaling of the analytic results by a factor of two to compensate for the symmetric trajectories. As discussed earlier, switching on the energy distribution redistributes flux from medium scales to the centre region. Correspondingly, the spectrum at 20 m distance shifts to higher amplitudes. The effect is stronger in the MC calculations than in the analytics. The MC 100 m spectrum fits well with the analytic results, whereas the MC 260 m spectrum lies at lower amplitudes than in the analytics: The radial dependence now falls off much steeper in the MC as compared to the analytic results, as is also visible in Fig. 3.29. Overall, the radial dependence follows a very much exponential decay. (We will carry out a detailed analysis of the functional form of different properties of the radio emission in a later paper.) It does not exhibit the prominent plateaus visible in the centre regions of the analytic calculations. Considering the much higher

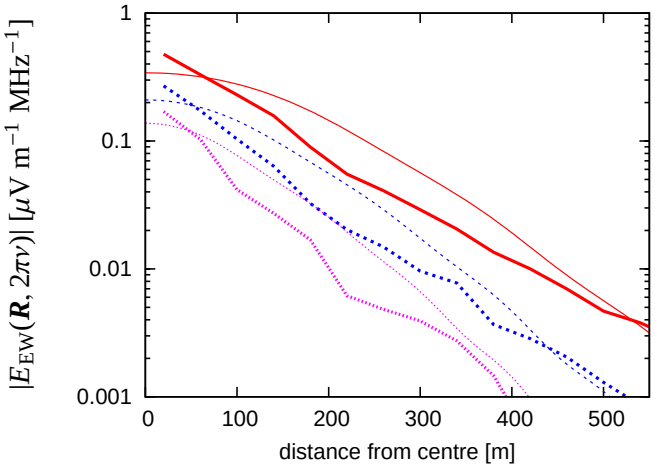

FIGURE 3.29—Radial dependence of the emission for the same scenario as in Fig. 3.28. Thin lines: analytic calculations from chapter 2 scaled down by a factor of two, thick lines: these MC simulations. Solid: ν = 50 MHz, dashed: ν = 75 MHz, dotted: ν = 100 MHz. Distance is to north from shower centre.

precision of the MC simulations and the neglect of edge effects and statistical trajectory lengths in the analytic calculations, however, we consider the agreement quite acceptable.

3.8 Emission from an integrated shower

After having analysed the emission from a shower slice, the next step in our analysis now is to perform the integration over the air shower as a whole.

3.8.1 Integration over shower evolution

In the theoretical calculations we performed in chapter 2, the integration over the shower evolution was carried out in a somewhat simplified way: The shower evolution was discretised into slices of independent generations of particles, spaced apart by one radiation length each. The overall emission was then superposed as the sum of the radiation from all these slices. Although this strategy should allow a good estimate of the emission from the complete shower, it has at least two problems: First, the total number of particles in the shower — and thus the total field amplitude — is directly influenced by the scale introduced through the spacing of the slices. A denser or wider spacing

directly leads to higher or lower emission levels, respectively. Although the radiation length is the logical choice for this scale, a "scale-free" approach would be a better choice. Second, our theoretical calculations, strictly speaking, are only valid in the far-field. Consequently, the emission from slices close to the ground, especially for high-energy showers, cannot be taken into account with the desired precision.

Both these pitfalls no longer pose a problem in the MC simulations: No far-field approximations at all were applied in the MC calculations, and the continuous evolution of the shower is correctly taken into account in the creation of particles according to the corresponding probability distribution function.

For the shower profile we use the Greisen parametrisation (Greisen 1960) that we already adopted in chapter 2:

$$N(s) = \frac{0.31 \exp\left[\frac{X_\mathrm{m}}{X_0} \frac{2-3\ln s}{3/s-1}\right]}{\sqrt{X_\mathrm{m}/X_0}}, \tag{3.11}$$

where the (theoretical) position of the shower maximum X_m is given by

$$X_\mathrm{m} = X_0 \ln\left(E_\mathrm{p}/E_\mathrm{crit}\right), \tag{3.12}$$

$X_0 = 36.7$ g cm^{-2} denotes the electron radiation length in air, $E_\mathrm{crit} = 86$ MeV corresponds to the threshold energy where ionisation losses equal radiation losses for electrons moving in air, and E_p specifies the primary particle energy. Equation (3.12) predicts the position of the shower maximum for a purely electromagnetic cascade, in which the shower age as a function of atmospheric depth then corresponds to

$$s(X) = \frac{3X}{X + 2X_\mathrm{m}}. \tag{3.13}$$

Obviously, this parametrisation of the shower age has to be modified to adequately describe the evolution of the hadronic air showers in our MC simulations. We choose to manually set the depth of the shower maximum to an empirical value $X_\mathrm{m,e}$ as a function of primary particle energy and shower inclination, e.g. $X_\mathrm{m,e} \sim 630$ g cm^{-2} for our typical 10^{17} eV vertical air shower. The shower age is then adopted as

$$s(X) = \frac{3X}{X + 2X_\mathrm{m,e}}, \tag{3.14}$$

whereas eq. (3.11) is left unchanged, i.e. retaining the theoretically motivated value for X_m.[1]

Eq. (3.11) denotes the integrated number of electronic particles that a detector positioned at atmospheric depth X measures as the shower sweeps through it. This number is *not* equal to the number of particles $I(X)$ that are "injected" at that atmospheric depth, the quantity we need to describe the probability distribution function for the creation of particles. The two quantities are directly related via the path length distribution of the particles. For an exponential path length distribution with mean free path length λ as given in eq. (3.10), the injection function is given by

$$I(X) = \frac{\mathrm{d}N}{\mathrm{d}X} + \frac{N}{\lambda}. \tag{3.15}$$

As demonstrated in Fig. 3.30, $I(X)$ closely follows the form of $N(X)$ with an offset of $\sim\lambda$ to lower X values, i.e.

$$I(X) \approx N(X + \lambda)/\lambda. \tag{3.16}$$

The shower evolution is thus taken into account in a continuous and consistent way by random creation of particles with probabilities according to eq. (3.15). Fig. 3.31 illustrates the shower evolution through the particle trajectories that are followed during the simulation of our 10^{17} eV vertical air shower.

3.8.2 Integrated shower results

As in the theoretical calculations, the integration over the shower evolution has two main effects, visible in Fig. 3.32: First, the emission level is boosted significantly. This directly shows that the emission is not described sufficiently by just taking into account the shower maximum. The second major effect is a steepening of the radial emission pattern due to the amplification of coherence losses. It is mainly the centre region which receives significant additional radiation. The steepness of the radial dependence is also illustrated by the strong drop in the maximum amplitude of the filtered pulses when one goes to even moderate distances of 260 m as shown in Fig. 3.33.

Another important effect is the further fading away of sharp features and

[1] A more realistic set of parameters for application of the Greisen function to hadronic showers in the energy range between 10^{17} and 10^{18} eV was established in Abu-Zayyad et al. (2001). For the moment, however, we retain the parametrisation as stated above to allow a better comparison with our earlier theoretical calculations.

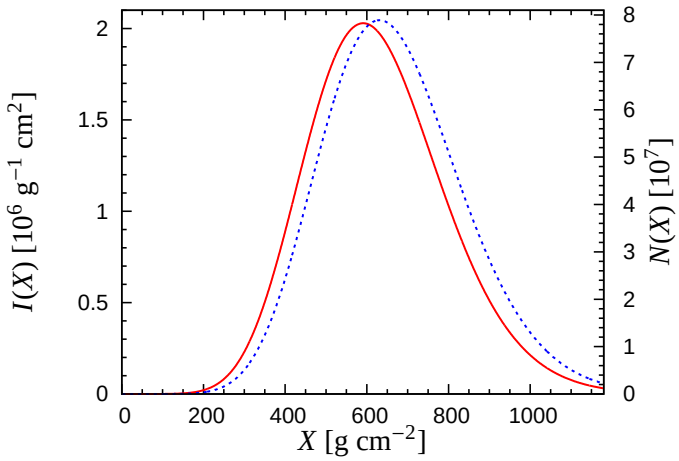

FIGURE 3.30—Comparison of $I(X)$ (solid) and $N(X)$ (dashed) as a function of atmospheric depth X for a vertical 10^{17} eV shower with $X_{\mathrm{m,e}} = 631$ g cm^{-2} and $\lambda = 40$ g cm^{-2}.

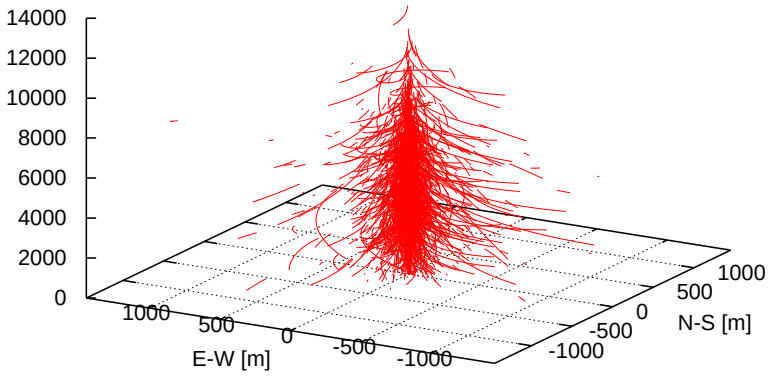

FIGURE 3.31—Trace of the trajectories in a complete 10 ^{17} eV air shower.

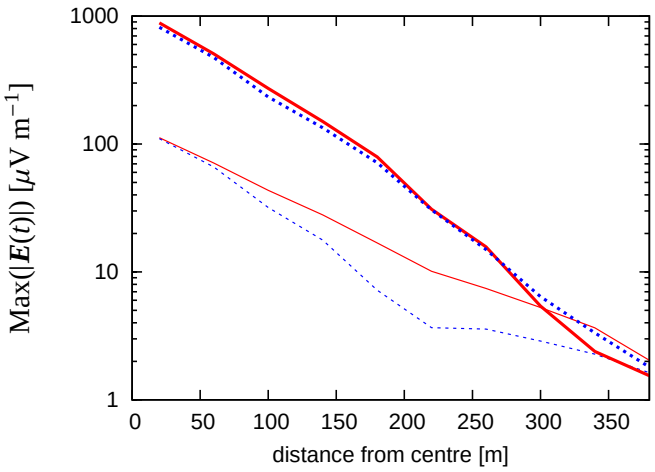

FIGURE 3.32—Effects introduced in the radial dependence of the 40–160 MHz rectangle-filtered pulse amplitude by the integration over the shower evolution. Thick lines: integrated 10^{17} eV vertical shower with broken power-law particle energy distribution, statistical track length distribution with $\lambda = 40$ g cm^{-2} and 70° inclined 0.5 Gauss magnetic field, thin lines: only shower maximum in same scenario. Solid: to the north, dashed: to the west.

the asymmetries associated with the geomagnetic field in the emission pattern, as illustrated by Fig. 3.34. While some of these features were still quite prominent in the emission from a single shower slice, they more or less vanish completely as soon as the integration is performed. Similarly, the effects of individual changes to the particle distributions, such as the specific choice of an energy distribution, are therefore much weaker than they are in case of a single shower slice.

The polarisation characteristics of the integrated shower are very similar to those of an individual slice. Again, the emission is highly polarised in the east-west direction, except for some regions at medium distances of ∼ 200–400 m as illustrated in Fig. 3.34 and, in a more quantitative way, Fig. 3.35.

Figure 3.36 shows a direct comparison of the radial profiles of the particle density (as given by the NKG-parametrisation) and the filtered radio pulse amplitude. The particle density falls off much more steeply than the radio signal in the central ∼ 200–250 metres. Further out, the slope becomes comparable for radio amplitude and particle density.

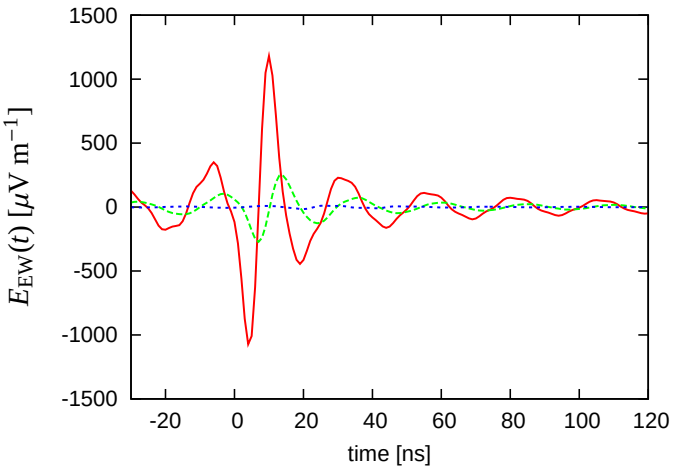

FIGURE 3.33—Pulses in the east-west polarisation component after 40–160 MHz rectangle-filtering for an integrated shower as described in Fig. 3.32. Solid: in the shower centre, long dashed: 100 m to north of centre, short dashed: 260 m to north of centre.

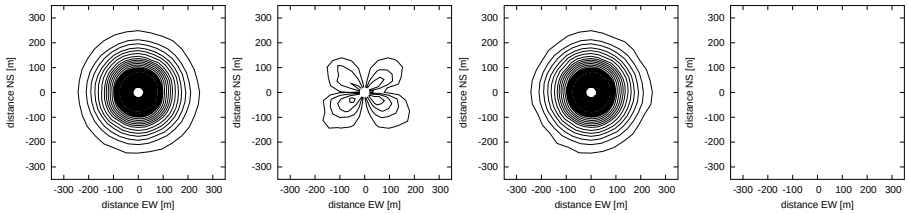

FIGURE 3.34—Contour plots of the 40–160 MHz rectangle-filtered pulse amplitude for the full shower described in Fig. 3.32. Contour levels are 20 μV m^{-1} apart. From left to right: total electric field strength, north-south polarisation component, east-west polarisation component, vertical polarisation component.

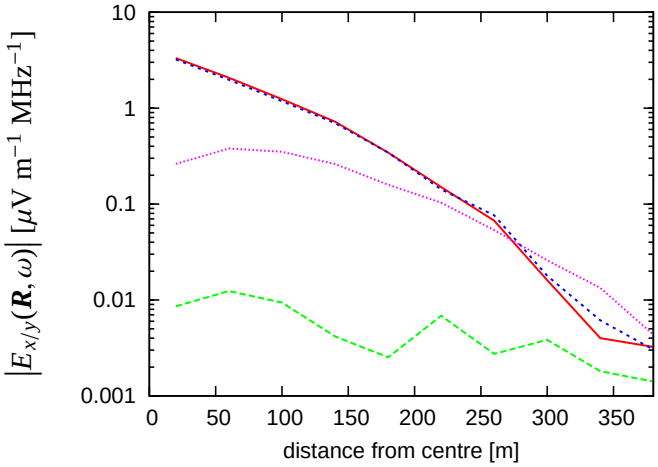

FIGURE 3.35—Radial dependence of $E(\boldsymbol{R},\omega)$ for different polarisation components at ν = 55 MHz for the same scenario as in Fig. 3.32. Solid: east-west polarisation to the north from centre, long-dashed: north-south polarisation to the north from centre, short-dashed: east-west polarisation to the north-west from centre, dotted: north-south polarisation to the north-west from centre.

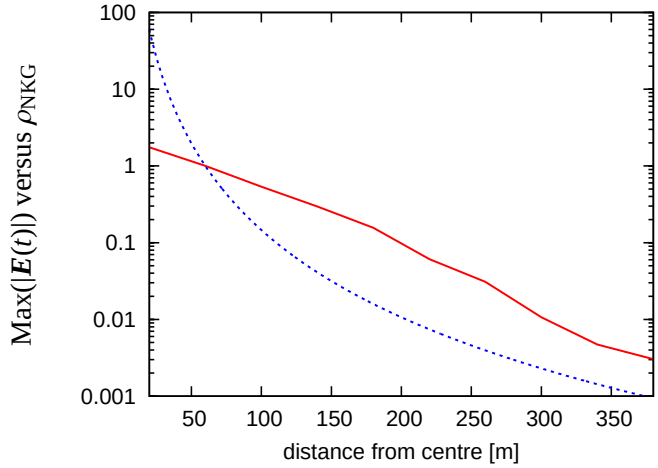

FIGURE 3.36—Comparison of the filtered radio pulse amplitude (solid) and the particle density as given by the NKG-parametrisation (dashed) as a function of radial distance from the shower centre. Values were normalised to unity at r = 60 m.

3.8.3 Comparison with theoretical calculations

We now compare the results of our MC simulations of a fully integrated 10^{17} eV vertical air shower with the theoretical calculations performed in chapter 2. Fig. 3.37 shows the spectral dependence of the emission in direct comparison. The MC results again produce somewhat lower levels of radiation. Scaling down the theoretical results by the systematic factor of two introduced in section 3.7.4, the agreement is much better, as shown in Fig. 3.38. Considering the huge differences in the two calculations, the agreement is quite remarkable.

In chapter 2 we compared the theoretical results with the available historical data. As discussed there in detail, the absolute values of the historical experimental data are very uncertain and largely discrepant between the different groups. Additional uncertainty arises from ambiguities in the exact definition of the historical values denoted as ϵ_ν and their conversion to the theoretical quantity $|\boldsymbol{E}(\boldsymbol{R},\omega)|$, which we performed via the relation

$$\epsilon_\nu = \sqrt{\frac{128}{\pi}}\,|\boldsymbol{E}(\boldsymbol{R},\omega)| \approx 6.4\,|\boldsymbol{E}(\boldsymbol{R},\omega)|\,. \tag{3.17}$$

To deal with the discrepant sets of data we decided to take the well documented Allan (1971) data as our reference and rescale the spectral data of Prah (1971) and Spencer (1969) to be consistent with the Allan data at $\nu = 55$ MHz. In this work, we use the identically rescaled data for comparison with our new MC spectra. While the absolute values of the spectral data are therefore somewhat arbitrary, they at least allow an evaluation of the qualitative spectral dependence. The spectral data are over-plotted in Fig. 3.38. The agreement with the spectral dependence in the centre region of the shower is very good.

In Fig. 3.39 we compare the radial dependence of the emission as calculated by our MC code with the earlier theoretical results and the Allan (1971) data. The scaled-down theoretical results again show good agreement with the MC results in the centre region. Overall, the MC predicts a somewhat steeper decrease of the emission levels to higher distances. It was, however, expected that the theoretical calculations overestimate the coherence and thus emission levels at high distances. The absolute level of the emission also agrees with the Allan data within the uncertainties.

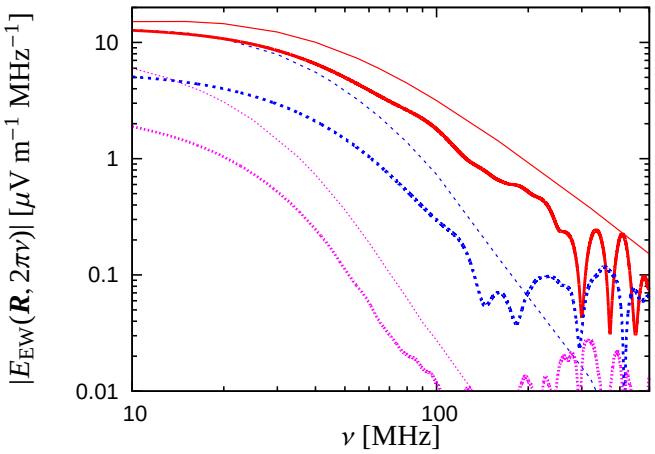

FIGURE 3.37—Spectra emitted by a complete 10^{17} eV vertical air shower with maximum at 4 km height, broken power-law particle energy distribution, statistically distributed particle trajectories with 40 g cm^{-2} mean path length and 70° inclined 0.5 Gauss magnetic field. Thin lines: analytic calculations from chapter 2, thick lines: these MC simulations. Solid: shower centre, dashed: 100 m, dotted: 250 m to north from shower centre.

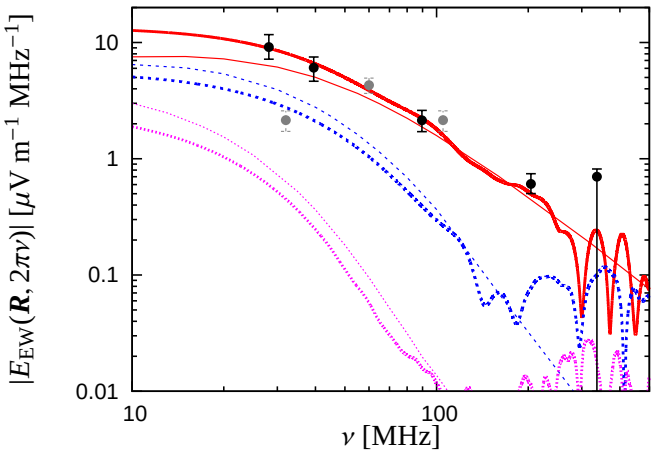

FIGURE 3.38—Same as Fig. 3.37 but scaling down the analytic results by a factor of two. Data from Prah (1971) (gray) and Spencer (1969) (black) were rescaled to be consistent with the Allan (1971) data at $\nu = 55$ MHz.

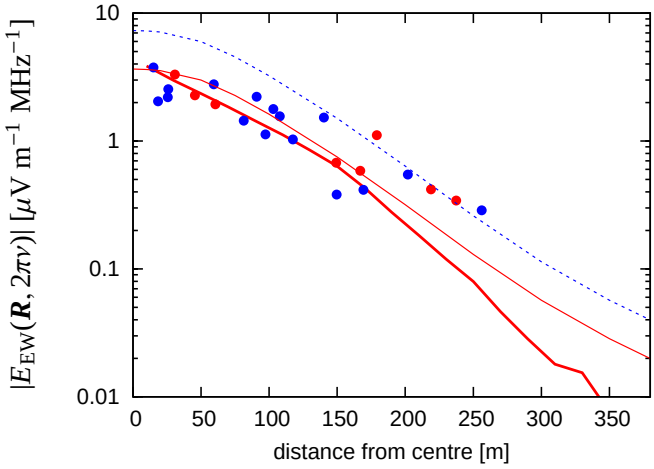

FIGURE 3.39—Radial dependence of the emission at $\nu = 55$ MHz for the same scenario as in Fig. 3.37. Dashed: analytic calculations from chapter 2. Solid: analytic calculations from chapter 2 scaled down by a factor of two (thin line) in comparison with these MC simulations (thick line). Data from Allan (1971). Distance is to north from shower centre.

3.9 Discussion

With the design and implementation of our MC simulation, we have taken the logical next step in the development of our geosynchrotron radiation model for radio emission from cosmic ray air showers. The MC technique provides an independent cross-check on our earlier theoretical works and allows us to model the emission from the air shower with much higher precision based on a much more realistic air shower model.

To make these simulations feasible on standard "off-the-shelf" computer hardware, we conceived and implemented a number of intelligent concepts. In particular, the smart sampling of the particle trajectories in conjunction with the automatic inactivation of ground-bins and the adaptive collection of the time-series data provide the necessary cut-down on computation time compared to a simple "brute-force" approach. At the same time, high precision is retained in the results as demonstrated by the detailed consistency checks presented in section 3.6. The calculation of a typical vertical 10^{17} eV air shower with realistic shower properties and $25,000,000$ particles combined with automatic ground-bin inactivation at very high precision takes about 400 seconds per ground-bin on a standard PC of the 1.6 GHz class. A very detailed calcu-

lation with 800 ground-bins (25 radial, 32 azimuthal), parallelised on 4 PCs, thus takes about one day.

A major new result of our MC simulations is the profound influence of edge effects arising from the finite lengths of the particle trajectories. These could not be taken into account in the theoretical calculations. In combination with the dependence of the individual particle emission on the magnetic field strength, the edge effects associated with the statistical distribution of track lengths wash out the asymmetries originally introduced into the total field strength emission pattern by the geomagnetic field to a high degree. Once the integration over the shower evolution as a whole is carried out, the asymmetry is gone completely. The absence of asymmetries in the total field strength emission pattern from an integrated shower is somewhat unfortunate, as a prominent asymmetry would have allowed an easy, yet unambiguous test of the geomagnetic emission mechanism via the statistics of radio pulse total field strengths alone.

The decomposition of the electric field into north-south, east-west and vertical polarisation components, however, shows that the emission is indeed highly polarised in the direction perpendicular to the shower axis and the magnetic field direction, as predicted by our theoretical calculations. Polarisation-dependent radio measurements such as the ones carried out by LOPES could therefore still unambiguously establish the geomagnetic emission mechanism.

The MC results show good consistency with the theoretical spectra and radial dependences — apart from a systematic factor of two in emission strength which is plausible considering the implicit assumption of symmetric trajectories in the analytic calculations. Such good agreement between the theoretical and MC calculations is remarkable considering the inherent differences in the two approaches. In particular, the integration over the shower evolution as a whole is carried out in a much more sophisticated way in the MC simulations as compared to the analytical works. As mentioned above, the polarisation characteristics of the emission are exactly as inferred in the theoretical calculations.

The spectra and radial dependences predicted by our MC code also agree well with the historical data of Allan (1971) and the data of Prah (1971) and Spencer (1969) scaled to the absolute level of the Allan data. The necessary rescaling, however, demonstrates that the historical data themselves are largely discrepant with absolute values reaching up to an order of magnitude lower than the Allan data (see chapter 2 for a detailed discussion). It is therefore still imperative to gather independent data with good absolute calibration with

new experiments such as LOPES (Horneffer et al. 2003). For air showers of energies around 10^{17} eV this should be well feasible as the predicted absolute levels of emission $|\boldsymbol{E}(\boldsymbol{R},\omega)|$ around a few μV m^{-1} MHz^{-1} at 55 MHz are well above the Galactic noise limit of $\sim 0.4/0.15/0.05$ μV m^{-1} MHz^{-1} for a 3σ detection with 1/10/100 LOPES antenna(s) (see chapter 2). In areas with high radio-frequency interference levels such as the site of the KASCADE array, the noise levels are a factor of a few higher.

3.10 Conclusions

We have successfully advanced our modelling of radio emission from cosmic ray air showers with elaborate Monte Carlo simulations in the time-domain. Our MC code takes into account the important air shower characteristics such as lateral and longitudinal particle distributions, particle energy and track length distributions, a realistic magnetic field geometry and the evolution of the air shower as a whole. The calculation retains the full polarisation information and does not employ any far-field approximations.

We predict emission patterns, radial and spectral dependences for an exemplary 10^{17} eV vertical air shower and find good agreement with our earlier theoretical works and the historical data available.

A major result that could not be obtained by analytic calculations alone is that asymmetries introduced into the total field strength emission pattern by the magnetic field direction are washed out completely in the radiation from an integrated air shower. Statistics of total field strengths alone can therefore not establish the geomagnetic emission mechanism. The clear polarisation dependence on the magnetic field direction, on the other hand, allows a direct test of the geomagnetic emission mechanism through polarisation-sensitive experiments such as LOPES.

After having documented the implementation details and having demonstrated the correctness and robustness of our MC simulations, our code is now in a stage where we can explore the dependence of the radio emission on a number of parameters such as shower axis direction, primary particle energy, depth of shower maximum and the like. Consequently, this will be our next step.

Once these dependences are established, measurements of radio emission from cosmic ray air showers can be related directly to the underlying characteristics of the observed air showers. Due to the regularity and robustness of the modelled emission patterns, even a sparse sampling of the radiation pattern with a limited number of antennas would probably suffice for such an analysis.

Furthermore, our code provides a solid basis for the inclusion of additional effects such as Askaryan-type (Askaryan 1962, 1965) Čerenkov radiation and an interfacing to the MC air shower simulation code CORSIKA.

Appendix: Trajectory

Consider first a simple magnetic field geometry

$$\tilde{\boldsymbol{B}} = B \begin{pmatrix} 0 \\ 0 \\ 1 \end{pmatrix}. \tag{3.18}$$

The (unperturbed) trajectory of a charged particle in a homogeneous magnetic field is a helix. Aligning the helix along the z-axis, it can be written as

$$\tilde{\boldsymbol{r}}(t) = \begin{pmatrix} -R_B \cos\left[\omega_B (t - t_0)\right] \\ +R_B \sin\left[\omega_B (t - t_0)\right] \\ v \cos\alpha \; (t - t_0) \end{pmatrix}, \tag{3.19}$$

where

$$R_B = \frac{v \sin\alpha}{\omega_B} \tag{3.20}$$

denotes the radius of the projected circular motion and

$$\omega_B = \frac{qeB}{\gamma m_e c} \tag{3.21}$$

is the gyration frequency of the particle with charge q times the elementary charge unit e and velocity

$$v = \beta\, c = \sqrt{1 - \frac{1}{\gamma^2}}\; c. \tag{3.22}$$

The pitch-angle α is given by the (constant) angle between the direction of the particle velocity vector and the magnetic field vector.

To derive the general form of this trajectory, we first rotate the coordinate system such that the B-field points in the desired direction. Afterwards, we adjust the phase t_0 such that the particle's initial velocity has the desired direction as specified by the initial velocity vector $\boldsymbol{V}$. In the last step we shift the trajectory so that at $t = 0$ it coincides with the desired starting position $\boldsymbol{R}$.

We want to transform the simple geometry field $\tilde{\boldsymbol{B}}$ to the desired geometry

$$\boldsymbol{B} = B \begin{pmatrix} \cos\theta \sin\varphi \\ \sin\theta \sin\varphi \\ \sin\theta \end{pmatrix}, \tag{3.23}$$

where $\varphi \in [0, 2\pi[$ and $\theta \in [0, \pi]$ are the azimuth and zenith angles known from spherical coordinates. This transformation is achieved by applying a rotation matrix

$$\begin{aligned} \mathbf{D} &= \begin{pmatrix} \cos\varphi & -\sin\varphi & 0 \\ \sin\varphi & \cos\varphi & 0 \\ 0 & 0 & 1 \end{pmatrix} \cdot \begin{pmatrix} \cos\theta & 0 & \sin\theta \\ 0 & 1 & 0 \\ -\sin\theta & 0 & \cos\theta \end{pmatrix} \\ &= \begin{pmatrix} \cos\theta\cos\varphi & -\sin\varphi & \sin\theta\cos\varphi \\ \cos\theta\sin\varphi & \cos\varphi & \sin\theta\sin\varphi \\ -\sin\theta & 0 & \cos\theta \end{pmatrix}, \end{aligned} \tag{3.24}$$

so

$$\boldsymbol{B} = \mathbf{D}\tilde{\boldsymbol{B}} \tag{3.25}$$

and, inversely,

$$\tilde{\boldsymbol{B}} = \mathbf{D}^{-1}\boldsymbol{B}. \tag{3.26}$$

Applying the same rotation to the trajectory (3.19) yields

$$\boldsymbol{r}(t) = \mathbf{D}\, \tilde{\boldsymbol{r}}(t). \tag{3.27}$$

To infer the phase t_0 corresponding to a given initial velocity $\boldsymbol{V}$, we rotate back $\boldsymbol{V}$ to the simple geometry,

$$\tilde{\boldsymbol{V}} = \mathbf{D}^{-1}\boldsymbol{V}. \tag{3.28}$$

The x- and y-component of $\tilde{\boldsymbol{V}}$ then directly determine t_0 through the relation

$$\omega_B t_0 = \mp \arctan\left(\pm \frac{\tilde{V}_x}{\tilde{V}_y}\right), \tag{3.29}$$

with the upper sign for $q > 0$ and the lower for $q < 0$ and where one has to take into account the correct quadrant for the arctan operation. In terms of the

components of $\boldsymbol{V}$ this yields

$$t_0 = \mp \arctan\left(\frac{\pm\left[(V_x\cos\varphi + V_y\sin\varphi)\cos\theta - V_z\sin\theta\right]}{V_y\cos\varphi - V_x\sin\varphi}\right)/\omega_B. \tag{3.30}$$

The last operation that has to be employed is a translation

$$\boldsymbol{r}_{\mathrm{abs}}(t) = \boldsymbol{R}_0 + \boldsymbol{r}(t) \tag{3.31}$$

of the trajectory such that

$$\boldsymbol{r}_{\mathrm{abs}}(t=0) = \boldsymbol{R}_0 + \boldsymbol{r}(t=0) = \boldsymbol{R}, \tag{3.32}$$

which yields

$$\begin{aligned}\boldsymbol{R}_0 &= \boldsymbol{R} + v\cos\alpha\; t_0 \begin{pmatrix} \sin\theta\cos\varphi \\ \sin\theta\sin\varphi \\ \cos\theta \end{pmatrix} \\ &+ R_B \begin{pmatrix} \cos\theta\cos\varphi\cos[\omega_B t_0] - \sin\varphi\sin[\omega_B t_0] \\ \cos\theta\sin\varphi\cos[\omega_B t_0] + \cos\varphi\sin[\omega_B t_0] \\ -\sin\theta\cos[\omega_B t_0] \end{pmatrix}.\end{aligned} \tag{3.33}$$

The resulting trajectory $\boldsymbol{r}_{\mathrm{abs}}(t)$ is thus fully defined for a given set of parameters $\boldsymbol{R}$ and $\boldsymbol{V}$. The time-dependence of particle velocity and acceleration are then easily derived as the time-derivatives of $\boldsymbol{r}_{\mathrm{abs}}(t)$.

4

Simulation Results

4.1 Introduction

In chapter 3 we described details of the design and implementation of our Monte Carlo simulations of radio emission from cosmic ray air showers in the scheme of coherent geosynchrotron radiation. These simulations are based on analytic parametrisations of the air shower characteristics and constitute a precursor to our upcoming full-fledged Monte Carlo simulations of radio emission from extensive air showers based on precise air shower modeling with CORSIKA (Heck et al. 1998).

In this article, we present the results inferred so far from the simulations performed with our code. After a short description of the underlying simulation parameters in section 4.2, we describe important characteristics of the radio emission in general such as the radial dependence, the spectral dependence, the curvature of the radio front and the polarisation characteristics of the radiation (which play an important role in experimentally verifying the dominant emission mechanism) in section 4.3. We analyse the dependence of these characteristics on the associated air shower parameters such as the shower geometry (zenith and azimuth angle), the primary particle energy, the depth of the shower maximum and the magnetic field in a qualitative way in section 4.4. Afterwards, we parametrise the emission's dependence on the various observer and shower parameters in a number of individual formulas for our reference shower (section 4.5) before generalising the parametrisations to arbitrary shower geometries and piecing together an overall parametrisation incorporating all dependences in section 4.6. We discuss our results in section

4.7 and conclude the chapter in section 4.8.

4.2 Simulation parameters

All simulations presented here were done with the Monte Carlo code described in chapter 3. In this section we specify the simulation strategy as well as the parameters and configuration options that were used throughout this work.

Obviously, we cannot perform a true *n*-dimensional analysis of the parameter space in question. We therefore choose a vertical 10^{17} eV air shower as a reference and change only one of the shower parameters at a time to analyse its effect on the radio emission. This implies that the effects introduced by changes of the different parameters are well-separable. We pay special attention in cases where this is obviously not true (e.g., primary particle energy and depth of the shower maximum).

Our reference air shower is calculated with a primary particle energy of 10^{17} eV, developing to its maximum at an atmospheric depth of 631 g cm^{-2} as originally adopted in chapter 2. This corresponds to a distance of ~ 4 km to the ground in case of a vertical air shower.

The following settings are kept throughout all simulations if not explicitly stated otherwise (for definitions of the terms in quotation marks see chapter 3): The particle track lengths are distributed following an exponential probability distribution with mean track length of 36.7 g cm^{-2} for both electrons and positrons. The particle energies are set to follow a broken power-law distribution peaking at $\gamma = 60$ as described in chapter 2. The magnetic field is chosen with a strength of 0.5 Gauss and an inclination of 70°, which approximately corresponds to the configuration present in central Europe. Calculations are done on a "simple grid" of 1 ns resolution with "smart trajectory sampling" enabled. "Automatic ground-bin inactivation" is used with a precision goal of 0.25% in 4 consecutive blocks of 10,000 particles each up to a maximum of 25,000,000 particles. A total of 800 bins (32 in azimuth; 25 in radius, up to a distance of 1000 m) is calculated in each simulation.

4.3 General characteristics

First, we present the general characteristics of the radio emission from a prototypical 10^{17} eV vertical air shower, which we take as the reference shower in this work.

4.3.1 Spectral dependence

In Fig. 4.1 we present the spectral dependence of the emission from a 10^{17} eV vertical air shower at various distances from the shower centre. The spectra show a steep decline towards higher frequencies due to the coherence diminishing as the wavelengths become shorter and thus comparable to the scales present in the shower "pancake". The field strength reaches a first interference minimum at a distance-dependent frequency. Afterwards, we see a quickly alternating series of maxima and minima that are insufficiently sampled in this calculation and therefore give rise to the unphysically seeming features at high frequencies. A realistic modelling of the emission in this incoherent regime would need a more detailed air shower model taking into account the inhomogeneities that are known to be present in the shower cascade. This cannot be achieved with the currently used analytic parametrisations of air shower properties, but will be accomplished once our code is interfaced to the air shower simulation code CORSIKA.

The higher the distance from the shower centre, the steeper the spectral dependence of the emission. In other words, coherence is much better up to high distances at lower frequencies as compared with higher frequencies: while the emission is coherent to large distances of > 500 m for the 10 MHz frequency component, it already becomes incoherent at ~ 300 m for the 55 MHz frequency component.

Figure 4.2 shows the spectra of the same 10^{17} eV vertical air shower plotted in a νS_ν diagram, illustrating that most of the power is emitted at frequencies around 20–30 MHz. (The conversion from electric field frequency component $E(\omega)$ to the frequency-domain equivalent of the Poynting vector S_ν is performed according to eq. (2.14), page 27.)

These two effects strongly point to low frequencies as the most promising regime for observation of cosmic ray air showers with radio techniques.

To demonstrate the differences for emission at low and high frequencies, we compare some of the results presented in the following sections for the two prototypical frequencies of 10 MHz (good coherence up to high distances as desirable for experimental measurements) and 55 MHz (frequency band used in the historical works and LOPES, cf. Horneffer et al. (2004), but coherence only up to medium distances).

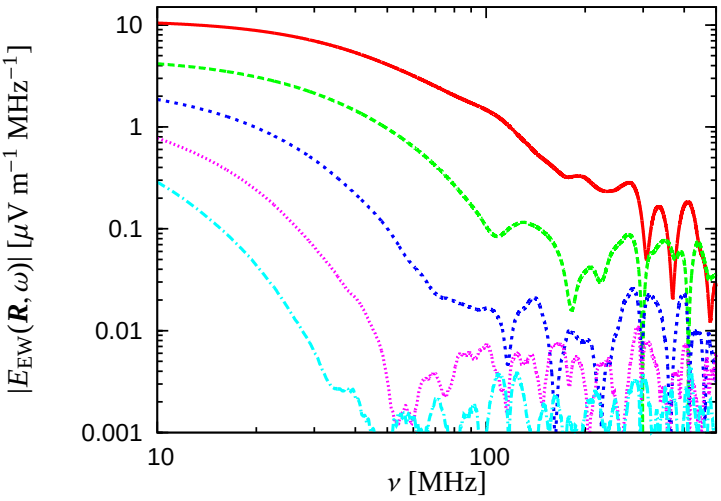

FIGURE 4.1—Spectra of the emission from a vertical 10 ^{17} eV air shower at various distances to the north. From top to bottom: 20 m, 140 m, 260 m, 380 m and 500 m.

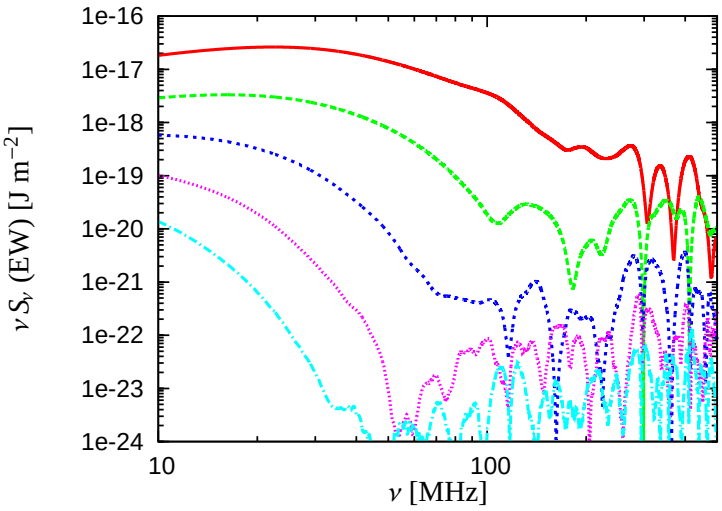

FIGURE 4.2—Same spectra as in fi gure 4.1 plotted in a νS_ν diagram.

4.3.2 Radial dependence and emission pattern

Fig. 4.3 shows the 10 MHz component of the electric field strength in the individual linear polarisation directions “north-south”, “east-west” and “vertical”. The total field strength pattern is remarkably symmetrical in spite of the intrinsic asymmetry of the geomagnetic emission mechanism. A more quantitative view of the radial dependence of the emission is depicted in Fig. 4.4.

Please note that we can equivalently use the east-west polarisation component or the total field strength in many of the following analyses as there is no flux in the north-south (let alone vertical) polarisation component along the north-south direction from the shower centre for air showers coming from the south.

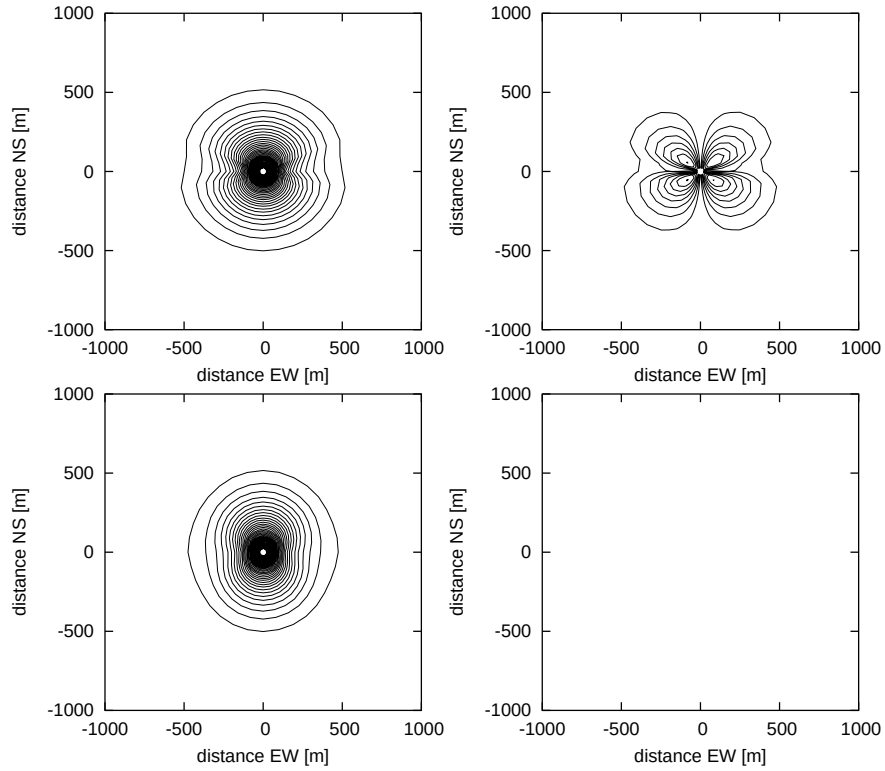

FIGURE 4.3—Contour plots of the 10 MHz field strength for emission from a 10^{17} eV vertical air shower. From top left to bottom right: total field strength, north-south polarisation component, east-west polarisation component, vertical polarisation component. Contour levels are 0.25 μV m^{-1} MHz^{-1} apart. There is no significant flux in the vertical component.

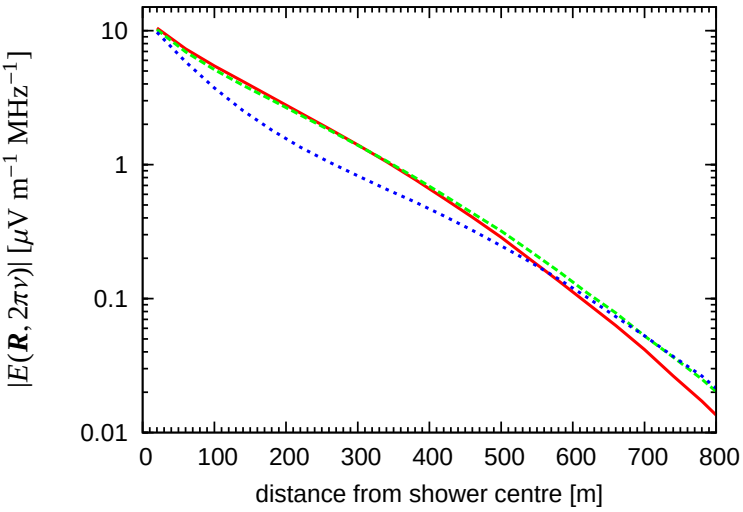

FIGURE 4.4—Radial dependence of the 10 MHz emission from a 10^{17} eV vertical air shower. Solid: to the north, dashed: to the north-west, dotted: to the west.

4.3.3 Wavefront curvature

The radio wavefront arriving at the ground is not planar. As demonstrated in Fig. 4.5, the pulses systematically lag behind at higher distances from the shower centre. The curvature of the wavefront can be approximated by a spherical surface with a given radius. At distances beyond a few hundred metres, this approximation, however, breaks down. (Additionally, the curvature radius derived from the timestamps of the maximum filtered pulse amplitudes depends on the specific filter used.) The scatter seen in the plot is not of statistical nature, but rather represents the slight time-shift in the pulses' peak amplitude as a function of azimuth angle.

The curvature of the radio wavefront plays an important role for the beamforming performed in digital radio interferometers and has indeed been confirmed by LOPES measurements (Horneffer, private communication).

4.3.4 Linear polarisation

The radio emission generated by the geosynchrotron mechanism is intrinsically linearly polarised. Figure 4.6 shows the raw (unfiltered) pulses arriving at a distance of 200 m to the north-west from the centre of a 10^{17} eV vertical air

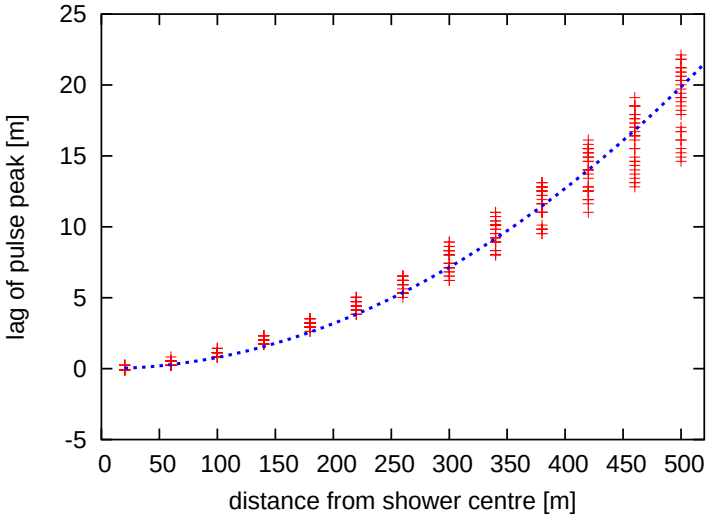

FIGURE 4.5—Radio wavefront curvature given by the time-lag of the east-west polarisation raw pulses emitted by a vertical 10^{17} eV air shower. Dotted line: curvature given by a spherical surface with 6,500 m radius.

shower. The north-south and east-west polarisation components are of similar strength and arrive almost synchronously. The vertical polarisation-component is negligible.

Figure 4.7 shows the same data (neglecting the vertical component) visualised as a scatter plot. For each time-step of the simulated pulse, a point specifying the north-south versus east-west field strength component is drawn. In other words, the series of points directly illustrates the evolution of the (projected) electric field vector. The very narrow "loop" performed by the vector in the upper-left quadrant of the diagram demonstrates that the emission is indeed linearly polarised to a very high degree, even at the already moderate distances presented here. (In case of perfect linear polarisation, the series of points would all lie on a straight line, whereas for perfect circular polarisation, the polarisation vector would follow a full circle around the origin.)

In the centre regions where the emission is strongest, the radiation is almost perfectly linearly polarised. In these regions, the polarisation vector points in the direction perpendicular to the air shower and magnetic field axes, as predicted in chapter 2, cf. section 4.4.2.

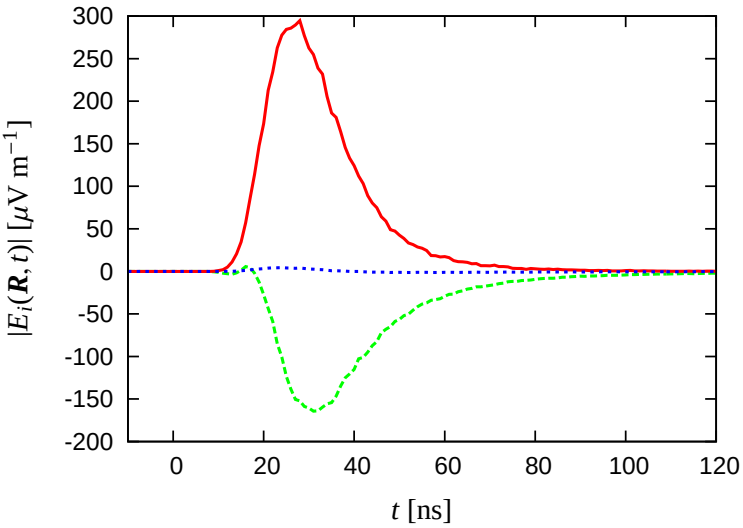

FIGURE 4.6—Raw (unfiltered) pulses in the individual linear polarisation components at 200 m distance to the north-west from the centre of a 10^{17} eV vertical air shower. Solid: east-west component, dashed: north-south component, dotted: vertical component.

4.4 Qualitative dependence on shower parameters

In the following subsections, we present a number of dependences of the radio emission on specific air shower parameters in a qualitative way.

4.4.1 Shower zenith angle

An interesting question is that of the radio emission's dependence on the air shower geometry. Fig. 4.8 shows the radial dependence of the 10 MHz frequency component for air showers coming from the south with different zenith angles. It is well visible that the radial dependence in the north (i.e., shower axis) direction becomes much flatter with increasing zenith angle.

A broadening of the emission pattern in the shower axis direction could be intuitively expected from projection effects occurring when the air shower is inclined. One can remove these projection effects by changing the coordinate system from the ground-based "distance to the shower centre" to the shower-based "(perpendicular) distance to the shower axis". (The electric field vector, however, is still denoted with the ground-based north-south, east-west and vertical components which thus do not change in strength. This method of

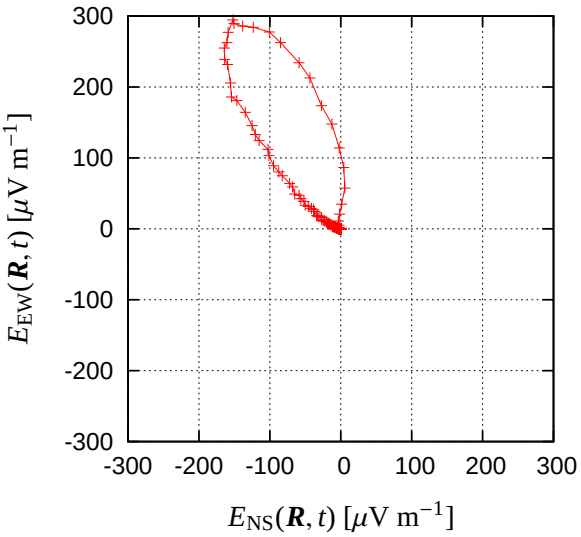

FIGURE 4.7—Scatter plot of the north-south and east-west polarisation components shown in Fig. 4.6. The emission is linearly polarised to a high degree.

"back-projection" is not the same as an inclination of the full ground-plane.) Fig. 4.9 shows the back-projected radial dependences for the 10 MHz emission. It is obvious that the flattening is still present and thus cannot simply be caused by projection, but is an intrinsic feature of the emission. The emission pattern broadens as a whole (even in the direction perpendicular to the shower axis) as can be seen when comparing the back-projected patterns for a 45° inclined air shower depicted in Fig. 4.13 with that of a vertical shower shown in Fig. 4.3.

The overall broadening of the emission pattern is due to the fact that the air shower maximum for inclined showers is much further away from the ground than for vertical showers. This effect was already predicted from geometrical/qualitative arguments by Gousset et al. (2004). It makes inclined air showers an especially interesting target for observation with radio techniques.

The slight deviation of the 15° zenith angle curve from the trend seen in Fig. 4.8 is explained by the shower's very small angle of only 5° to the 70° inclined geomagnetic field. The weakness of this deviation alone demonstrates that the dependence of the emission on the strength and orientation of the geomagnetic field is very slight — except regarding the polarisation effects analysed in Sec. 4.4.2. Consequently, the same diagram for air showers coming

from the north (not shown here) looks very similar.

Fig. 4.10 shows the zenith angle dependence for the 55 MHz frequency component. The overall trend is the same as in the 10 MHz case, but the coherence losses cut off the emission pattern at a zenith angle dependent distance of a few hundred metres. At zenith angles $\gtrsim 30°$, however, the coherence begins to hold up to high distances. This is confirmed by the spectra of a 45° inclined 10^{17} eV air shower shown in Fig. 4.11. The spectra are much flatter up to high distances when compared with the vertical case in Fig. 4.1.

Inclined air showers thus not only offer significantly broader emission regions on the ground, but provide the advantage that the larger "finger-print" even extends to significantly higher frequencies.

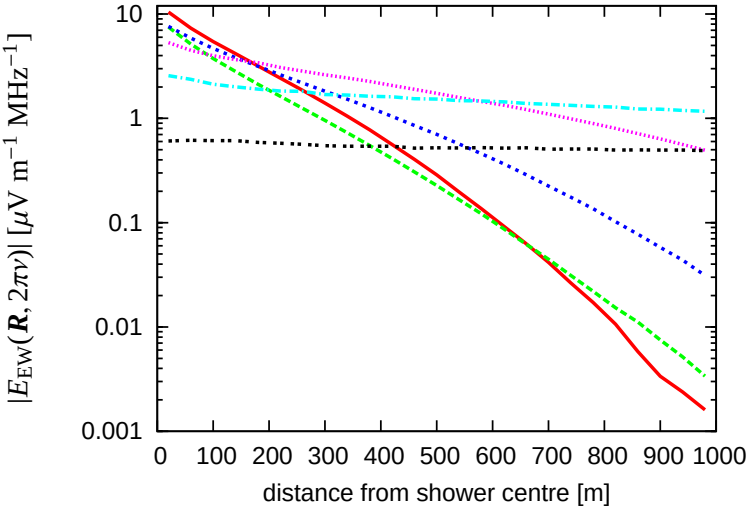

FIGURE 4.8—Dependence of the 10 MHz east-west electric field component emitted by a 10^{17} eV air shower coming from the south for different shower zenith angles as a function of distance to the north. Red/solid: vertical shower, green/dashed: 15°, blue/dotted: 30°, violet/short dotted: 45°, turquois/dash-dotted: 60°, black/double-dotted: 75° zenith angle.

4.4.2 Shower azimuth angle and polarisation

A very important trait of the radio emission is its predicted polarisation, which is directly related to the shower azimuth angle. Knowledge of this dependence is imperative for the planning and interpretation of experimental measurements.

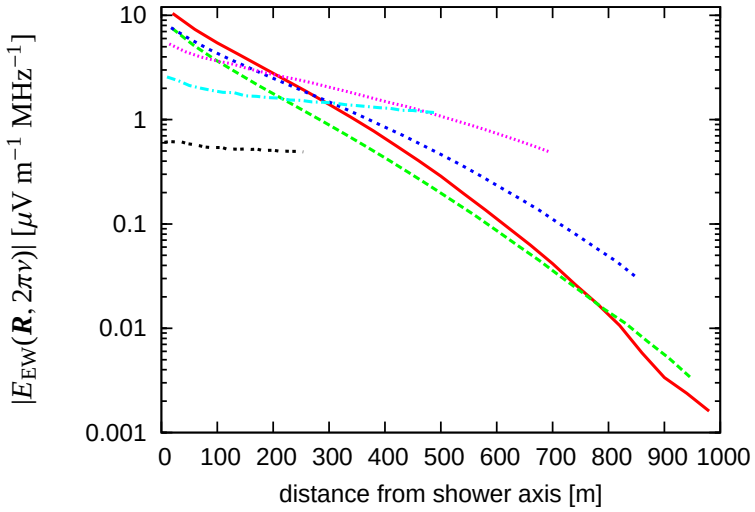

FIGURE 4.9—Same as Fig. 4.8 back-projected to the shower-based coordinate system (see text).

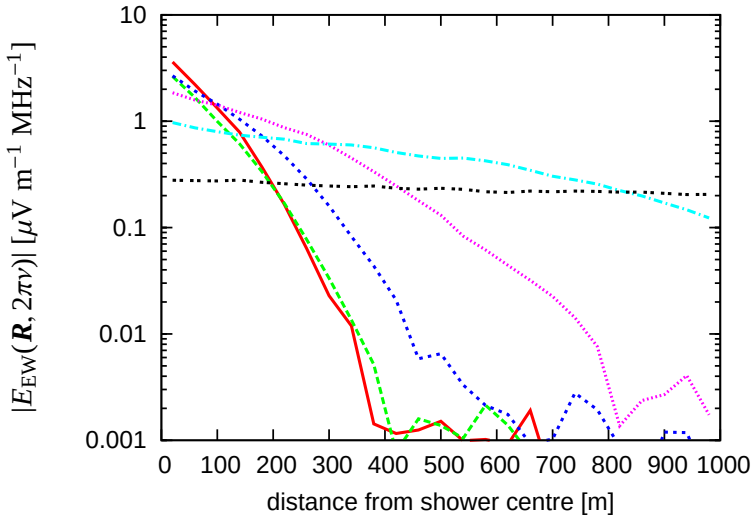

FIGURE 4.10—Same as Fig. 4.8 for the 55 MHz frequency component.

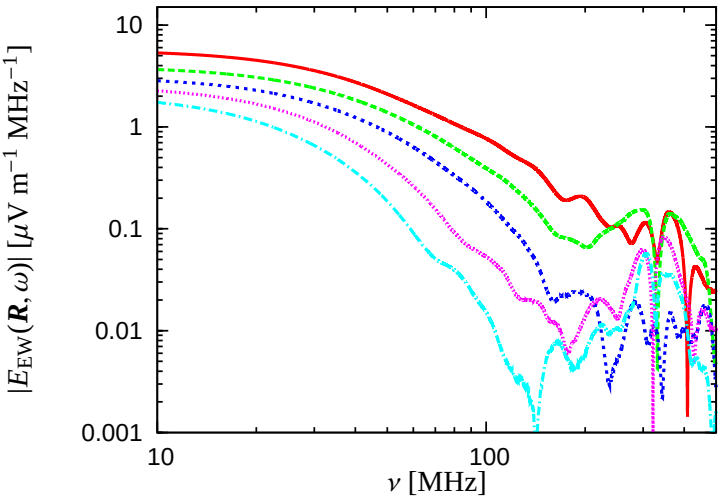

FIGURE 4.11—Spectra of the emission from a 10^{17} eV air shower with 45° zenith angle at various distances to the north. From top to bottom: 20 m, 140 m, 260 m, 380 m and 500 m.

Fig. 4.12 shows a comparison of the emission at 10 MHz from 10^{17} eV air showers with 45° zenith angle as a function of azimuth angle. The total field strength pattern is elongated due to the projection effects arising at high shower zenith angles (cf. section 4.4.1). Taking out the pure projection effects leads to the patterns depicted in Fig. 4.13. The patterns are much more circular, but retain a significant intrinsic ellipticity and asymmetry.

The total field strength pattern of the emission (left column) simply rotates as a function of azimuth angle. (Deviations from a pure rotation are caused by the symmetry-breaking due to the magnetic field and shower axes — the emission pattern is no longer supposed to be truly symmetric.) In other words, no significant information associated to the geomagnetic field direction is present in the signal. As a direct consequence, it is not possible to verify the geomagnetic origin of the emission with an experiment measuring only the total field strength (or only one circular polarisation component) of the emission. Furthermore, because the air showers arrive isotropically from all azimuthal directions, there will not be any azimuthal dependence of the measured pulse amplitudes in statistical samples of measured total field strength pulses. It will therefore not be possible to confirm air showers as the source of measured radio pulses from statistics of total field strength data alone. In this case, inde-

pendent information about the simultaneous arrival of cosmic rays, e.g. from particle detectors, would be necessary.

The situation is different when one looks at the individual linear polarisation components. (As demonstrated in section 4.3.4, the emission is polarised linearly to a very high degree.) It is visible from the right three columns of Fig. 4.12 that the field strength in the different polarisation directions has a direct dependence on the geomagnetic field direction: the signal is linearly polarised mainly in the direction perpendicular to the air shower and magnetic field axes, at least in the central regions of high emission. The non-zero contributions in the vertical polarisation direction arise from the 70° inclination of the geomagnetic field. Fig. 4.14 illustrates the polarisation characteristics of the central emission region in a more intuitive way through indicators denoting the ratio of north-south to east-west polarisation component overplotted over the total field strength contours.

Due to these polarisation characteristics, experiments which measure the polarisation characteristics of the emission can therefore directly verify the geomagnetic origin of the radio emission from cosmic ray air showers.

4.4.3 Magnetic field

As discussed in section 4.4.2, the magnetic field has important influence on the polarisation characteristics of the radio emission. The influence on the total electric field strength, however, is very weak.

In Fig. 4.15 we compare the 10 MHz total field strength and polarisation characteristics of vertical 10^{17} eV air showers in four different magnetic field configurations: fields of 0.3 Gauss and 0.5 Gauss strength with horizontal and 70° inclined geometry. A 0.3 Gauss horizontal magnetic field is present in the equatorial region, whereas a 0.5 Gauss $\sim 70°$ inclined magnetic field is present in central Europe.

The change from a horizontal magnetic field to a 70° inclined magnetic field introduces a number of effects. First, a small north-south asymmetry arises. Second, the overall emission level drops only very slightly — although the projected magnetic field that the vertical air shower sees drops by a factor of $\cos^{-1}(70°) \approx 3$. This demonstrates the very weak effect of the magnetic field on the total emission field strength. The most prominent change is visible in the polarisation characteristics along the east-west direction from the shower centre.

Increasing the field strength from 0.3 Gauss to 0.5 Gauss mainly boosts the flux in the east-west direction from the shower centre in case of a horizon-

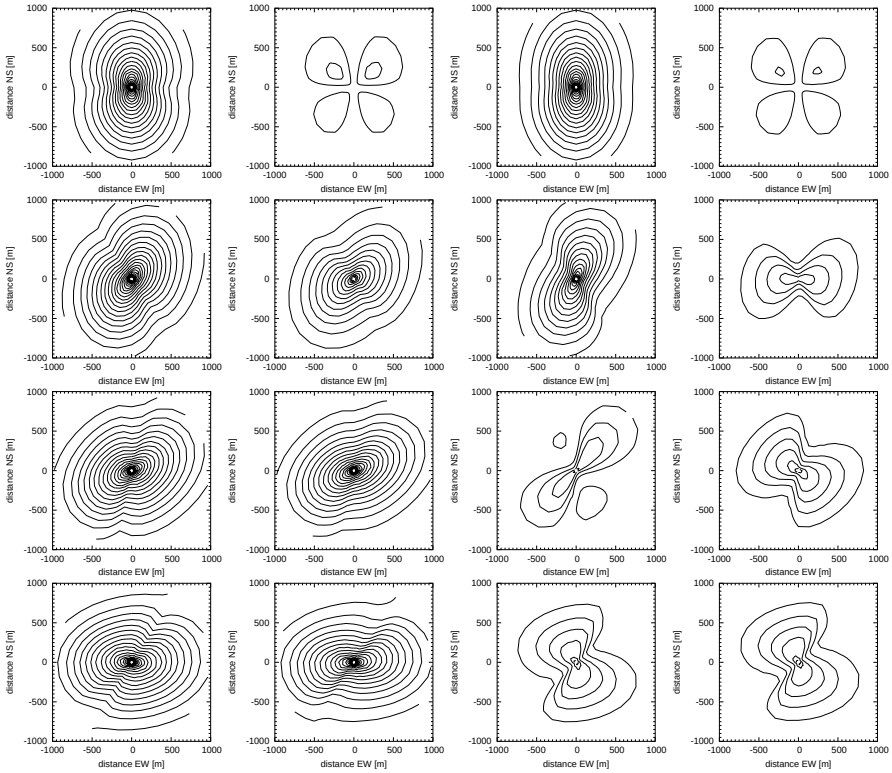

FIGURE 4.12—Contour plots of the 10 MHz emission from a 10^{17} eV air shower with 45° zenith angle as a function of shower azimuth. Columns from left to right: total field strength, north-south, east-west and vertical polarisation component. Lines from top to bottom: 0°, 30°, 60° and 90° azimuth angle. Contour levels are 0.25 μV m^{-1} MHz^{-1} apart.

tal magnetic field. In case of a 70° inclined magnetic field, the changes are minimal.

4.4.4 Primary particle energy

Another important characteristic of the radio emission is its dependence on the primary particle energy. In Fig. 4.16 we present the dependence of the 10 MHz frequency component at various distances from the centre of a vertical air shower as a function of primary particle energy. Although the depth of the shower maximum obviously depends on the primary particle energy, it is kept constant in these calculations to assess the influence of the primary particle

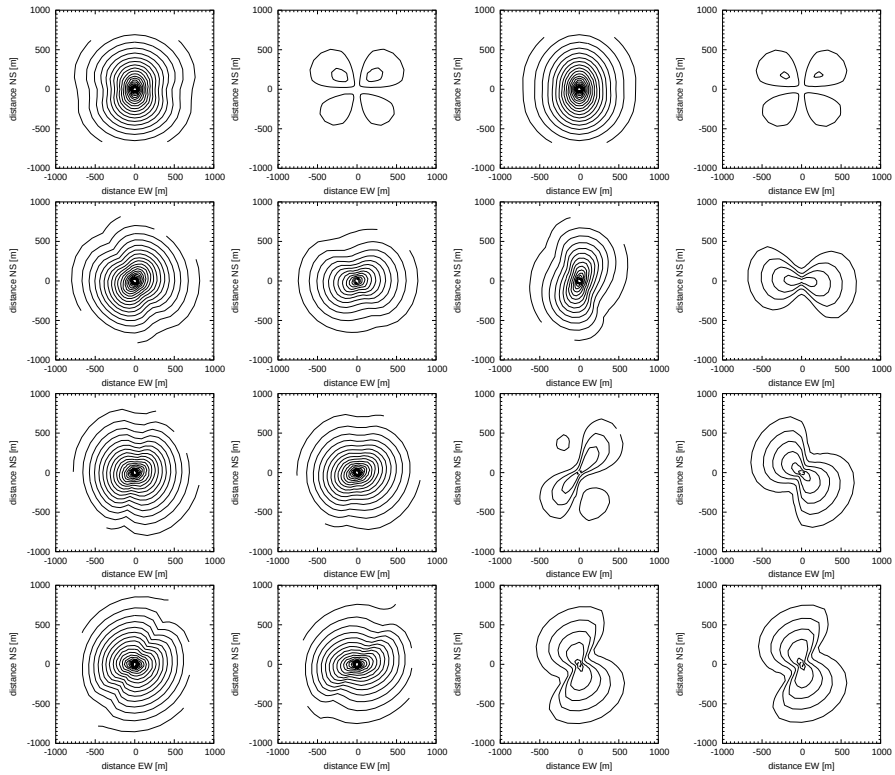

FIGURE 4.13—Same as Fig. 4.12 but back-projected to the shower-based coordinate system (distances are measured perpendicularly from the shower axis).

energy alone. (For a combined dependence see section 4.5.4).

The scaling of the field strength with primary particle energy is approximately linear, following a power-law $\propto E_{\mathrm{p}}^{0.96}$. For 55 MHz, the diagram is very similar until the curves again cut off at distances of a few hundred metres due to coherence losses (not shown here). The spectra do not change significantly in comparison with the 10^{17} eV case except for an overall change in amplitude as demonstrated in Fig. 4.17 in comparison with Fig. 4.1.

An approximate linear scaling of the emission with primary particle energy is to be expected for coherent emission. In the coherent regime, the field strength directly scales with the number of emitting particles. (The emitted power consequently scales as the number of particles squared.) Since the number of particles grows approximately linearly with primary particle energy in

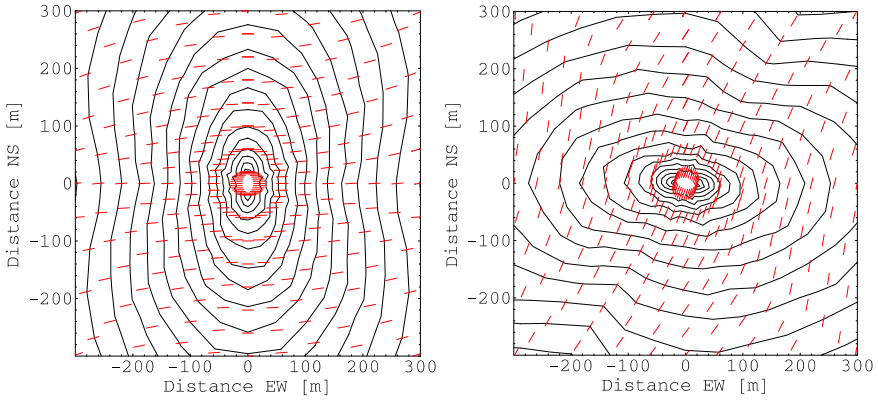

FIGURE 4.14—Contour plot of the total 10 MHz electric field component emitted by a 10^{17} eV 45° inclined air shower with overplotted indicators denoting the ratio of east-west to north-south polarisation. Left: azimuth of 0°, right: azimuth of 90°. Contour levels are 0.25 μV m^{-1} MHz^{-1} apart.

the parametrisations at the basis of our simulations (see chapter 3), the linear scaling directly translates to a linear scaling of the field strength with primary particle energy.

4.4.5 Depth of shower maximum

The depth of the air shower maximum is directly related to the nature and energy of the primary particle (cf., e.g., Pryke 2001). Additionally, it is one of the parameters that undergoes strong fluctuations between individual showers with otherwise identical parameters. It is therefore interesting to evaluate the dependence of the emission on this parameter.

As can be seen in Fig. 4.18, there is a significant dependence of the emission on the depth of the air shower maximum. The deeper penetrating the air shower, the steeper becomes the radial emission pattern. This is especially important for extremely high-energy air showers $\gtrsim 10^{20}$ eV, where the shower maximum can develop close to sea-level. The effect is the same as that visible in the zenith angle dependence (cf. section 4.4.1), where it is much more pronounced because the (spatial) distance of the shower maximum from the ground grows very rapidly with increasing zenith angle for a given value of $X_{\max}$.

The effect is very similar at 55 MHz, except for the cutoffs due to the loss

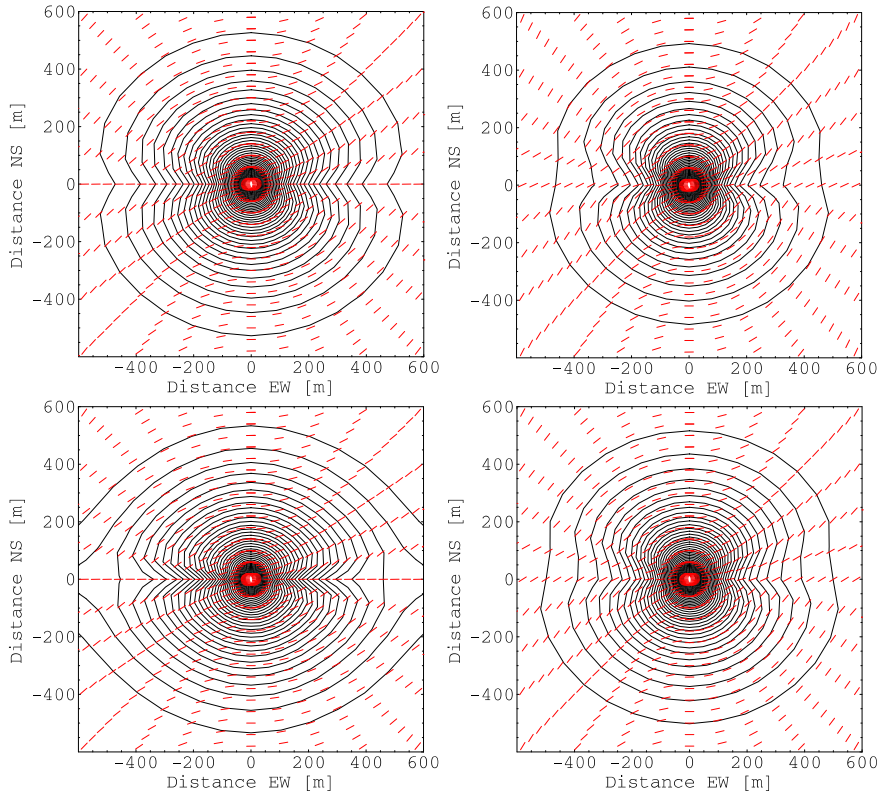

FIGURE 4.15—Contour plots of the total 10 MHz electric field emitted by a 10^{17} eV vertical air shower with overplotted indicators denoting the ratio of east-west to north-south polarisation. Top: 0.3 Gauss magnetic field, bottom: 0.5 Gauss magnetic field, left: magnetic field horizontal, right: magnetic field 70° inclined. Contour levels are 0.25 μV m^{-1} MHz^{-1} apart.

of coherence at distances above a few hundred metres.

4.5 Parametrisations for vertical showers

Having analysed the qualitative dependences of the radio emission on various air shower and observer parameters, constructing a parametrisation of these dependences would be very useful. In a first step, we therefore quantify the dependences in a simple manner for vertical geometry. Afterwards, we generalise these dependences to an arbitrary geometry and piece together an overall parametrisation taking into account the parameters simultaneously.

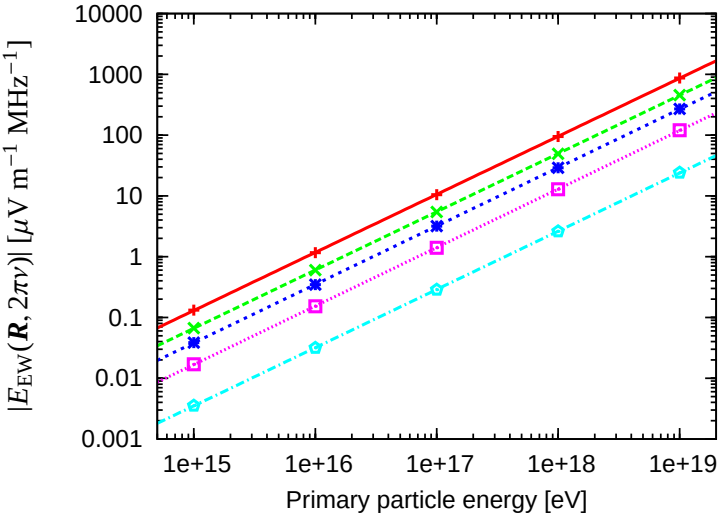

FIGURE 4.16—Scaling of the 10 MHz east-west electric field component emitted by a vertical air shower as a function of primary particle energy E_{p}. From top to bottom: 20 m, 100 m, 180 m, 300 m and 500 m from the shower centre. The data follow a power-law $\propto E_{\mathrm{p}}^{0.96}$.

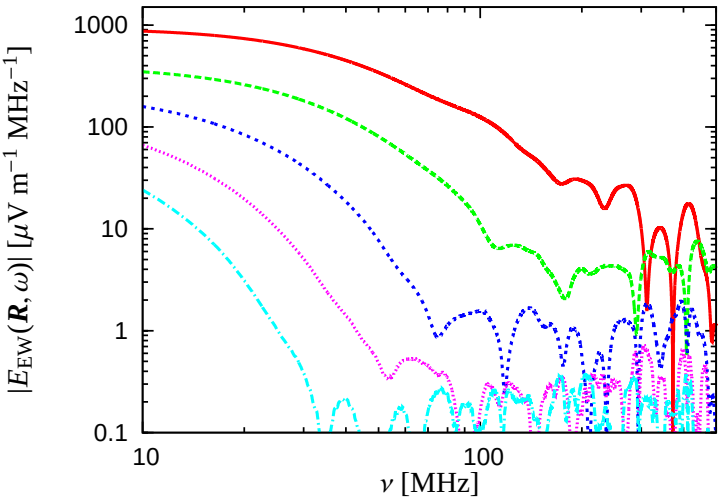

FIGURE 4.17—Spectra of the emission from a vertical 10^{19} eV air shower at various distances to the north. From top to bottom: 20 m, 140 m, 260 m, 380 m and 500 m.

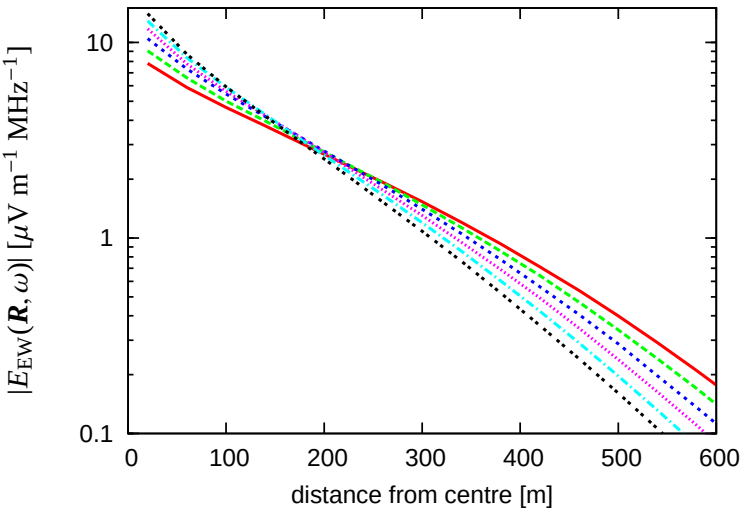

FIGURE 4.18—Radial dependence of the 10 MHz component from a vertical 10^{17} eV air shower with various depths of the shower maximum X_{max}. Red/solid: X_{max} = 560 g cm^{-2}, green/dashed: X_{max} = 595 g cm^{-2}, blue/dotted: X_{max} = 631 g cm^{-2}, violet/short dotted: X_{max} = 665 g cm^{-2}, turquois/dash-dotted: X_{max} = 700 g cm^{-2}, black/double-dotted: X_{max} = 735 g cm^{-2}.

As there is no direct error estimate for the underlying Monte Carlo results, we neither specify any χ^2 values nor make any error estimates for the derived fit parameters in the following sections. We specify our fit parameters with a high number of significant digits, knowing that the parameters are not determined with such high precision. Nevertheless, this allows an overall better representation of the Monte Carlo results with the fit functions. To verify the quality and estimate the deviation of our parametrisation from the Monte Carlo data, we then make a direct comparison of our overall parametrisation and the corresponding Monte Carlo results for a sample of test parameter sets in section 4.6.5.

4.5.1 Radial dependence

The radial dependence of the emission on distance r from the shower centre can be fit with an exponential decay,

$$|\boldsymbol{E}(r, 2\pi\nu)| = E_0 \ \exp\left[-\frac{r}{r_0}\right]. \tag{4.1}$$

Fig. 4.19 shows the simulated 10 MHz and 55 MHz total field strength components as a function of distance to the north from the shower centre with the associated exponential fits. For the 10 MHz component, we fit one exponential in the central 500 m and a second in the outer 500 m region. This increases the quality of both fits very significantly. For the 55 MHz component, we use only the values up to 380 m, as the emission becomes incoherent at higher distances. We do not take any asymmetry of the emission pattern (cf. Fig. 4.3) into account in this parametrisation.

ν [MHz]	E_0 [μV m^{-1} MHz^{-1}]	r_0 [m]	valid r [m]
10	12.3	135.3	0–500
10	84.4	90.44	500–1000
55	7.85	51.36	0–380

TABLE 4.1—Parameters for the radial fits according to eq. (4.1) depicted in Fig. 4.19.

4.5.2 Spectral dependence

The spectral dependence in the coherent regime can also be parametrised well with an exponential decay. The dependence in the incoherent regime at high

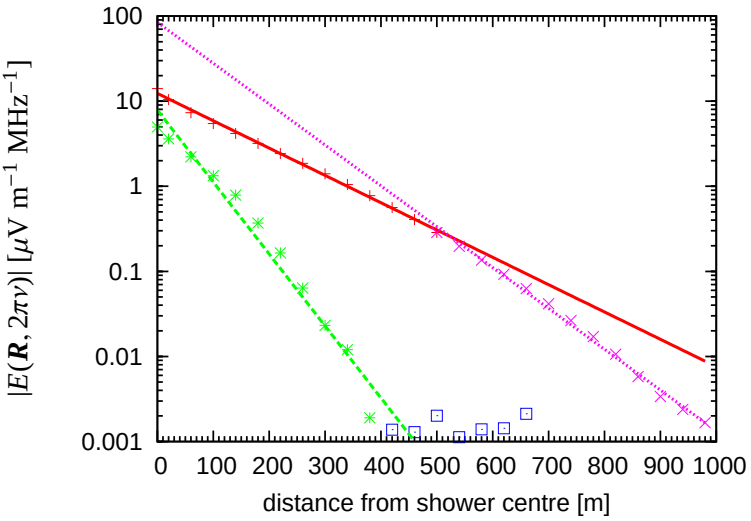

FIGURE 4.19—Exponential radial dependence of the 10 MHz emission in the central 500 m (solid), 10 MHz emission in the outer 500 m (dotted) and 55 MHz emission (dashed) from a 10^{17} eV vertical air shower with corresponding Monte Carlo simulated data.

frequencies is not well determined by the Monte Carlo simulations performed so far. It is, however, probably flatter than an exponential decay as demonstrated from the analytical calculations, where the functional form converges towards a power-law (cf. Fig. 2.16). Outside the valid ν-regime, the parametrisation therefore is bound to underestimate the real flux. We fit the function

$$|\boldsymbol{E}(r, 2\pi\nu)| = E_0 \ \exp\left[-\frac{(\nu - 10\ \text{MHz})}{\nu_0}\right] \tag{4.2}$$

to spectra at various distances r from the shower centre to the north. The parameter E_0 in this case directly represents the total field strength at 10 MHz. Only data in the coherent regime is used for the fitting procedure. The data range used is indicated in Fig. 4.20 together with the resulting fit functions. The associated fit parameters are listed in Table 4.2.

4.5.3 Polarisation characteristics

In the centre region, the emission is almost purely linearly polarised in the direction perpendicular to the magnetic field and air shower axes (cf. Fig. 4.14),

r [m]	E_0 [μV m^{-1} MHz^{-1}]	ν_0 [MHz]	valid ν [MHz]
20	10.01	46.501	10–180
140	4.693	24.382	10–110
260	1.867	14.020	10–80
380	0.7942	8.0787	10–50
500	0.2858	5.2633	10–32

TABLE 4.2—Parameters for the spectral fits according to eq. (4.2) depicted in Fig. 4.20.

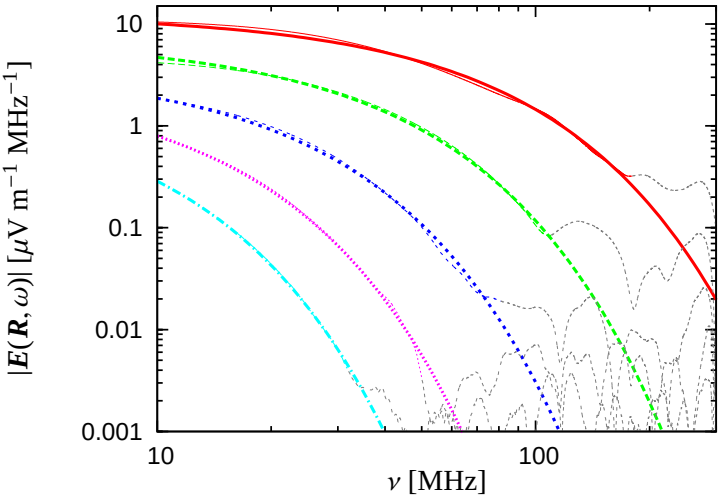

FIGURE 4.20—Fit of exponential functions to spectra from a 10^{17} eV vertical air shower at various distances to the north. From top to bottom: 20 m, 140 m, 260 m, 380 m and 500 m. Only the data in the coherent regime is used for the fit, as indicated by the colours.

in good agreement with the analytic calculations. In particular, the electric field vector points into the direction

$$\hat{\boldsymbol{E}}(\theta,\varphi,\vartheta_\mathrm{B}) = \frac{\begin{pmatrix} \sin\theta\ \sin\vartheta_\mathrm{B}\ \sin\varphi \\ \cos\theta\ \cos\vartheta_\mathrm{B} - \cos\varphi\ \sin\theta\ \sin\vartheta_\mathrm{B} \\ \cos\vartheta_\mathrm{B}\ \sin\theta\ \sin\varphi \end{pmatrix}}{\sqrt{(\cos\theta\ \cos\vartheta_\mathrm{B} - \cos\varphi\ \sin\theta\ \sin\vartheta_\mathrm{B})^2 + \sin^2\theta\ \sin^2\varphi}}, \quad (4.3)$$

where θ denotes the shower zenith angle, φ is the shower azimuth angle with respect to the magnetic north and ϑ_B specifies the inclination angle (i.e., complement of the zenith angle) of the magnetic field.

Multiplication of an $\left|\boldsymbol{E}(r, 2\pi\nu, E_\mathrm{p})\right|$-value with the unit polarisation vector $\hat{\boldsymbol{E}}(\theta, \varphi, \vartheta_\mathrm{B})$ then directly yields the estimated north-south, east-west and vertical linear polarisation components (in this order).

The complex dependences at higher distances from the shower centre cannot be easily parametrised at this stage.

4.5.4 Combined E_p and X_max dependence

We have discussed the radio emission's dependence on the primary particle energy and the depth of the shower maximum separately in earlier sections. Here, we parametrise the combined dependence on primary particle energy and appropriately adjusted depth of shower maximum reflecting the deeper atmospheric penetration of higher energy air showers. (We set X_max to 500, 560, 631, 700 and 770 g cm^{-2} for E_p values of 10^{15}, 10^{16}, 10^{17}, 10^{18} and 10^{19} eV, respectively, see Pryke 2001; Knapp et al. 2003). The steepening of the radial dependence for increasing X_max discussed in section 4.4.5 in this case leads to a radius-dependent steepening or flattening of the energy dependence (originally $\propto E_\mathrm{p}^{0.96}$ as shown in section 4.4.4) in the central and outer regions, respectively. However, the combined dependence is still well-described by a power-law of the type

$$\left|\boldsymbol{E}(r, 2\pi\nu, E_\mathrm{p})\right| = E_0 \left(\frac{E_\mathrm{p}}{10^{17}\ \mathrm{eV}}\right)^{\kappa(r)} . \tag{4.4}$$

The associated fit parameters are listed in Table 4.3.

r [m]	E_0 [μV m^{-1} MHz^{-1}]	κ	valid E_p [eV]
20	10.18	1.057	10^{15}–10^{19}
100	5.188	1.004	10^{15}–10^{19}
180	2.995	0.965	10^{15}–10^{19}
300	1.315	0.907	10^{15}–10^{19}
500	0.265	0.808	10^{15}–10^{19}

TABLE 4.3—Parameters for the combined primary particle energy and depth of shower maximum dependence according to eq. (4.4) depicted in Fig. 4.21.

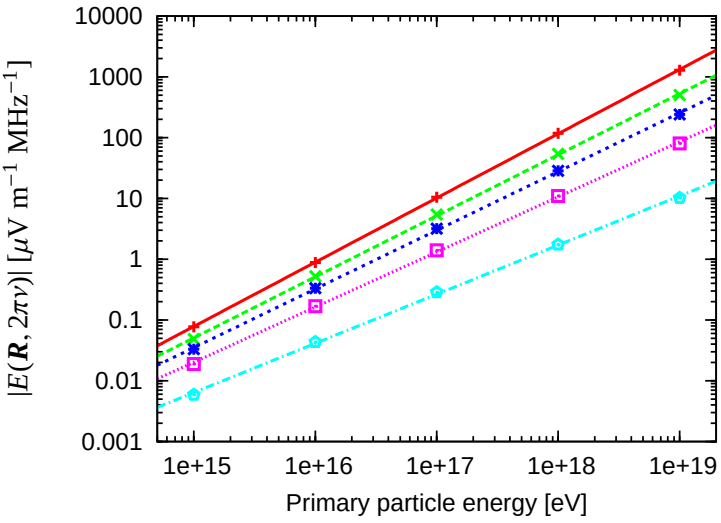

FIGURE 4.21—Scaling of the 10 MHz electric field emitted by a vertical air shower as a function of primary particle energy E_p with appropriately changing depth of shower maximum X_max. From top to bottom: 20 m, 100 m, 180 m, 300 m and 500 m to the north from the shower centre.

4.6 Parametrisations for arbitrary geometry

We now generalise our parametrisations of the radio emission as a function of air shower and observer parameters to an arbitrary shower geometry. As our final result, we piece the individual parametrisations together to an overall parametrisation incorporating all major parameters.

4.6.1 Radial dependence

The emission pattern becomes increasingly asymmetric with increasing zenith angle (cf. Fig. 4.12). As discussed in section 4.4.1, most of this asymmetry is caused by projection effects that can be taken into account by changing from a ground-based coordinate system (distance r from the shower centre) to a shower-based coordinate system (perpendicular distance l from the shower axis), cf. Fig. 4.13. The remaining intrinsic asymmetries in the emission pattern we do not take into account in our parametrisation.

The back-projection from the ground-based to the shower-based coordi-

nate system is given by

$$l(r) = r\sqrt{1 - \cos^2(\varphi_o - \varphi)\sin^2(\theta)}, \tag{4.5}$$

when φ and θ specify the shower azimuth and zenith angle and r and φ_o denote the observer distance from the shower centre and the observer azimuth angle (azimuth angles being measured with respect to the north). The 10 MHz back-projected radial dependence can then be well fit as

$$|\boldsymbol{E}(l)| = E_\theta \ \exp\left[-\frac{l}{l_\theta}\right]. \tag{4.6}$$

The fitting is performed as described in section 4.5.1 for each zenith angle θ individually. We restrain ourselves to the inner 500 m (back-projected) radius to increase the accuracy of the parametrisation. We also base the fits on air showers coming from the north rather than the south to exclude the deviation for the 15° zenith angle case arising from the only 5° angle to the geomagnetic field in case of an air shower coming from the south. The resulting fits are depicted in Fig. 4.22, and the corresponding parameters are listed in table 4.4.

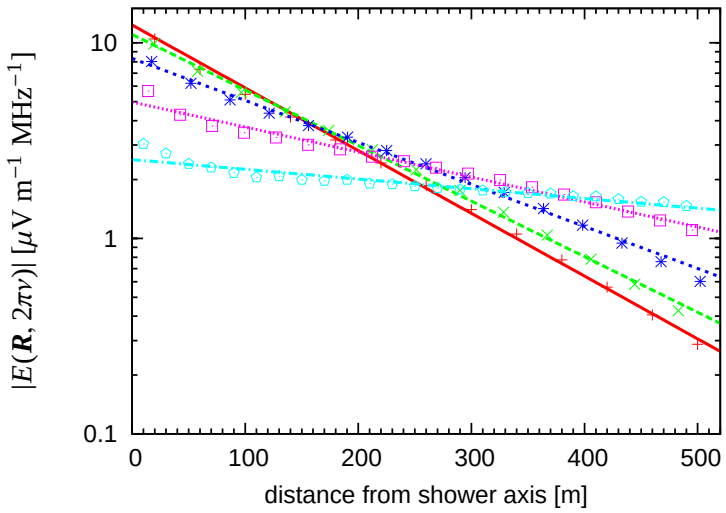

FIGURE 4.22—Radial dependence to the north for the 10 MHz emission from a 10^{17} eV air shower with corresponding exponential fits. Red/solid: vertical shower, green/dashed: 15°, blue/dotted: 30°, violet/short dotted: 45°, turquois/dash-dotted: 60° zenith angle.

θ	E_θ [μV m^{-1} MHz^{-1}]	l_θ [m]	valid l [m]
0°	12.33	135.30	0–500
15°	11.04	152.80	0–500
30°	8.33	202.09	0–500
45°	4.98	339.71	0–500
60°	2.53	873.54	0–500

TABLE 4.4—Parameters for the radial fits according to eq. (4.6) depicted in Fig. 4.22.

4.6.2 Spectral dependence

Similarly as for the radial dependence, we now generalise our parametrisation for the spectral dependence of the reference shower to an arbitrary shower geometry using the same exponential fits as adopted in section 4.5.2. Again, for each shower zenith angle individually, we fit a number of spectra at different distances l from the shower axis using the function

$$|\boldsymbol{E}(l, 2\pi\nu)| = E_\theta(l)\ \exp\left[-\frac{(\nu - 10\ \text{MHz})}{\nu_\theta(l)}\right]. \tag{4.7}$$

We do not show the individual fits explicitly here. The resulting parameters $E_\theta(l)$ and $\nu_\theta(l)$ are tabulated in table 4.5. The dependence of ν_θ on the distance to the shower axis l can in turn be parametrised with an exponential function

$$\nu_\theta(l) = a_\theta\ \mathrm{e}^{-l/b_\theta}. \tag{4.8}$$

In fact, the parameter a_θ can be fixed to the same value for all cases of θ analysed here at only minor loss of precision. The fits with a_θ fixed to a value of 47.96 MHz are shown in Fig. 4.23. The associated parameters for b_θ are listed in table 4.6.

4.6.3 Dependence of radial scale factor on $X_{\max}$

To factor the influence of the (vertical equivalent) depth of shower maximum into the parametrisation, we have to parametrise the flattening of the emission's radial dependence with increasing $X_{\max}$. To achieve this, we fit the radial dependences calculated for vertical 10^{17} eV showers with various values of $X_{\max}$ (shown in Fig. 4.18) with exponential functions in the central 500 m (not shown here). As can be seen in Fig. 4.18, the curves overlap at a distance

θ	l [m]	E_θ [μV m^{-1} MHz^{-1}]	ν_θ [MHz]	valid ν [MHz]
0°	20.0	10.01	46.501	10–180
0°	140.0	4.693	24.382	10–110
0°	260.0	1.867	14.020	10–80
0°	380.0	0.7942	8.0787	10–50
0°	500.0	0.2858	5.2633	10–32
15°	19.3	9.594	45.000	10–180
15°	135.2	4.805	26.705	10–110
15°	251.1	2.591	14.138	10–80
15°	367.1	1.183	8.2633	10–50
15°	483.0	0.433	5.8116	10–32
30°	17.3	8.185	44.532	10–110
30°	155.9	4.210	26.770	10–110
30°	259.8	2.596	17.131	10–70
30°	363.7	1.563	10.416	10–50
30°	502.3	0.582	7.0933	10–32
45°	14.1	6.145	40.824	10–110
45°	127.3	3.583	36.512	10–110
45°	212.1	2.653	21.487	10–100
45°	381.1	1.948	13.550	10–60
45°	495.0	1.245	8.866	10–50
60°	10.0	3.251	43.881	10–100
60°	130.0	2.285	39.652	10–100
60°	250.0	2.032	34.980	10–100
60°	370.0	1.964	25.318	10–80
60°	490.0	1.657	19.828	10–70

TABLE 4.5—Parameters for the spectral fits of 10^{17} eV air showers with arbitrary geometry according to eq. (4.7). (The arbitrary-seeming values for l are due to calculation of the air shower in the ground-based coordinate system with subsequent conversion to the shower-based coordinate system.)

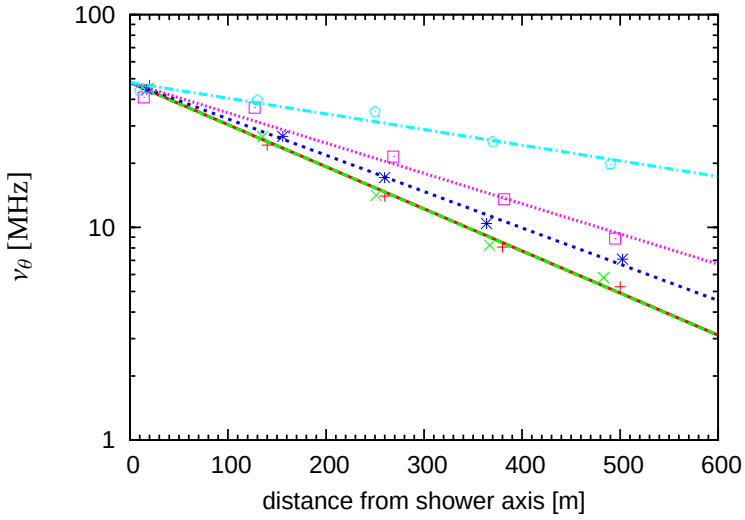

FIGURE 4.23—Parametrisation of ν_θ as a function of distance to the shower axis l according to eq. (4.8). Red/solid: vertical shower, green/dashed: 15°, blue/dotted: 30°, violet/short dotted: 45°, turquois/dash-dotted: 60° zenith angle.

θ	b_θ [m]
0°	219.41
15°	219.16
30°	254.23
45°	305.17
60°	590.03

TABLE 4.6—Parameters for the parametrisation of $\nu_\theta(l)$ according to eq. (4.8).

of $l = r \sim 200$ m. Taking this point as a reference, the effect of changing $X_{\max}$ can be reduced to a pure change of the slope, i.e., the scale factor l_θ of the exponential. We can then quantify the change of this scale factor by the ratio

$$\alpha(X_{\max}) = \frac{l_\theta(X_{\max})}{l_\theta(631 \text{ g cm}^{-2})} \tag{4.9}$$

of the scale factor for a given $X_{\max}$ and the scale factor of our reference shower. Figure 4.24 shows α as a function of $X_{\max}$ and a fit of this dependence using a power-law

$$\alpha(X_{\max}) = 1.00636 \left(\frac{X_{\max}}{631 \text{ g cm}^{-2}} \right)^{-1.50519} . \tag{4.10}$$

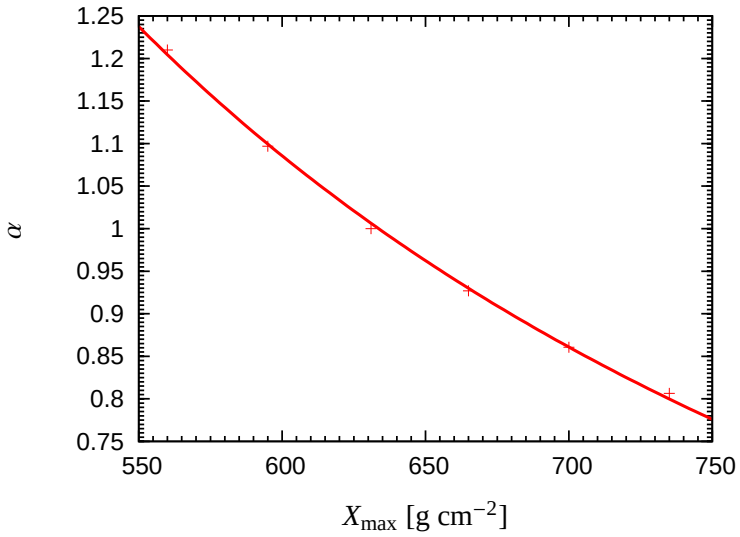

FIGURE 4.24—Ratio α of the scale factor for a given $X_{\max}$ to the scale factor of the reference shower as a function of $X_{\max}$ and corresponding power-law fit.

4.6.4 Overall parametrisation

We now piece the individual parametrisations together to an overall formula. This implies that the different effects are independent of each other and therefore can be separated in an easy way, which need not be true in all cases. Nevertheless, such an overall parametrisation can be a useful basis for comparisons of experimental data with theoretical predictions as long as one keeps

the limitations of the parametrisation in mind. We therefore provide a formula similar to the parametrisation first given by Allan (1971) and further enhanced by Falcke & Gorham (2003). The associated sets of parameters are given for each zenith angle individually.

At the heart of the parametrisation is the radial dependence for arbitrary geometry as described in section 4.6.1. This we combine with the spectral dependence derived in section 4.6.2 and get

$$|\boldsymbol{E}(r,\varphi_\mathrm{o},\nu)| = E_\theta \, \exp\left[-\frac{l(r,\varphi_\mathrm{o})}{l_\theta}\right] \exp\left[-\frac{\nu/\mathrm{MHz} - 10}{47.96 \, \exp\left[-l(r,\varphi_\mathrm{o})/b_\theta\right]}\right] \tag{4.11}$$

with the parameters as listed in table 4.7. Additionally, we can factor in the

θ	E_θ [μV m^{-1} MHz^{-1}]	l_θ [m]	b_θ [m]
0°	12.33	135.30	219.41
15°	11.04	152.80	219.16
30°	8.33	202.09	254.23
45°	4.98	339.71	305.17
60°	2.53	873.54	590.03

TABLE 4.7—Parameters for the overall parametrisation of the air shower emission according to eq. (4.12).

primary particle energy dependence (cf. 4.4.4) and the dependence of the radial scale factor on the (vertical shower equivalent) depth of the shower maximum derived in section 4.6.3. For the latter, we have to take into account the change of the field strength in the shower centre associated with the steepening of the scale factor l_θ calculated from the reference point at $l = 200$ m. The resulting overall parametrisation is then given by

$$\begin{aligned} \left|\boldsymbol{E}(r,\varphi_\mathrm{o},\nu,E_\mathrm{p},X_\mathrm{max})\right| &= E_\theta \left(\frac{E_\mathrm{p}}{10^{17}\ \mathrm{eV}}\right)^{0.96} \\ &\times \exp\left[-\frac{200\,\mathrm{m}\,(\alpha(X_\mathrm{max})-1) + l(r,\varphi_\mathrm{o})}{\alpha(X_\mathrm{max})\, l_\theta}\right] \\ &\times \exp\left[-\frac{\nu/\mathrm{MHz} - 10}{47.96 \, \exp\left[-l(r,\varphi_\mathrm{o})/b_\theta\right]}\right] \end{aligned} \tag{4.12}$$

with $\alpha(X_\mathrm{max})$ defined in eq. (4.10), $l(r,\varphi_\mathrm{o})$ given by eq. (4.5) and the values for E_θ, l_θ and b_θ taken from table 4.7. To calculate the field strength for the

individual linear polarisation components, one can then multiply the result of eq. (4.12) with the unit polarisation vector given in eq. (4.3).

4.6.5 Quality and validity of the overall parametrisation

To verify the quality of our parametrisation, we take a sample of observer parameters testing the different regimes of the parametrisation and compare the result of eq. 4.12 with the result from the Monte Carlo simulation. As can be seen in table 4.8, the deviations are acceptably small: most of the time the error is below 10%, and only in cases where the parametrisation is expected to degrade (e.g. in the east-west direction of heavily inclined air showers, where the intrinsic asymmetries in the emission pattern become relevant) it grows beyond 20%. This is a very satisfactory result.

θ [°]	E_p [eV]	X_max [g cm^{-2}]	r [m]	φ_o [°]	ν [MHz]	$\lvert E_\mathrm{param}\rvert$ $\left[\frac{\mu\mathrm{V}}{\mathrm{m\ MHz}}\right]$	$\lvert E_\mathrm{MC}\rvert$ $\left[\frac{\mu\mathrm{V}}{\mathrm{m\ MHz}}\right]$	deviation [%]
0	10^{17}	631	0	0	10	12.22	14.07	-13.21
0	10^{17}	631	0	0	44.43	5.96	6.58	-9.51
0	10^{17}	631	100	0	10	5.86	5.45	7.47
0	10^{17}	631	420	45	10	0.56	0.59	-5.93
0	10^{17}	631	0	0	55	4.78	4.98	-4.1
0	10^{17}	560	20	0	10	8.49	7.82	8.57
0	10^{17}	735	60	0	55	2.99	2.55	17.01
0	10^{17}	735	260	0	10	1.62	1.53	5.73
0	10^{18}	700	20	0	10	120.28	118.13	1.81
0	10^{19}	631	220	45	10	172.41	199.45	-13.55
15	10^{17}	631	60	45	55	2.18	2.24	-2.42
30	10^{17}	631	100	0	55	1.45	1.59	-9.19
45	10^{17}	631	20	0	10	4.76	5.67	-16.01
45	10^{17}	631	180	0	10	3.42	3.42	0.03
60	10^{17}	631	300	0	10	2.13	1.99	6.89
60	10^{17}	631	300	45	10	1.93	2.09	-7.67
60	10^{17}	631	300	0	55	0.64	0.73	-12.59
60	10^{17}	631	300	45	55	0.47	0.66	-28.56

TABLE 4.8—Quality check of the overall parametrisation given by eq. (4.12).

One must of course be careful not to leave the parameter regimes for which the parametrisation was created. Specifically, the back-projected radial dis-

tance l was limited to 500 m in the underlying radial fits. The frequency limits for the spectral fits can be estimated from table 4.5 as a function of l. As explained earlier, the parametrisation is bound to severely underestimate the flux at higher frequencies. The polarisation characteristics given by eq. (4.3) are only valid for the central region as illustrated by Fig. 4.14. At significant zenith angles, the intrinsic asymmetries of the emission pattern which were not taken into account in the parametrisation lead to a growing deviation from the Monte Carlo results. Finally, special caution should be used when changing the depth of shower maximum $X_{\max}$ for significantly inclined air showers, as the underlying parametrisation of $\alpha(X_{\max})$ was derived for vertical air showers only and the projection effects associated with inclined showers greatly enhance the depth of shower-maximum effects.

4.6.6 Comparison with Allan-parametrisation

Allan (1971) provided a parametrisation of their experimental data which has in turn been generalised by Falcke & Gorham (2003) to the form

$$\begin{aligned} \epsilon_\nu &= 13\,\mu\text{V m}^{-1}\,\text{MHz}^{-1} \left(\frac{E_\text{p}}{10^{17}\,\text{eV}}\right) \left(\frac{\sin\alpha\,\cos\theta}{\sin 45^\circ\,\cos 30^\circ}\right) \\ &\times \exp\left[\frac{-r}{r_0(\nu,\theta)}\right] \left(\frac{\nu}{50\,\text{MHz}}\right)^{-1}, \end{aligned} \tag{4.13}$$

where α denotes the angle between shower axis and magnetic field, θ is the shower zenith angle and r_0 is a scale factor of about 110 m. To compare this with our results, we have to convert the experimentally motivated ϵ_ν values to our theoretically derived $E(\omega)$ values. For the conversion we use the relation

$$\epsilon_\nu = \sqrt{\frac{128}{\pi}}\,|\boldsymbol{E}(\boldsymbol{R},\omega)| \approx 6.4\,|\boldsymbol{E}(\boldsymbol{R},\omega)| \tag{4.14}$$

as derived in chapter 2. The conversion results in

$$\begin{aligned} |\boldsymbol{E}(\boldsymbol{R},\omega)| &= 2\,\mu\text{V m}^{-1}\,\text{MHz}^{-1} \left(\frac{E_\text{p}}{10^{17}\,\text{eV}}\right) \left(\frac{\sin\alpha\,\cos\theta}{\sin 45^\circ\,\cos 30^\circ}\right) \\ &\times \exp\left[\frac{-r}{r_0(\nu,\theta)}\right] \left(\frac{\nu}{50\,\text{MHz}}\right)^{-1}. \end{aligned} \tag{4.15}$$

Our parametrisation yields a value of 3.6 μV m^{-1} MHz^{-1} for the 50 MHz emission in the centre of a 30° zenith angle 10^{17} eV air shower, which is not far

off the Allan-value of $2\,\mu\mathrm{V\,m^{-1}\,MHz^{-1}}$. The radial dependence in both cases is given by an exponential decay, and the resulting scale-factor in our parametrisation indeed corresponds to ~ 110 m for the aforementioned set of parameters. The linear scaling with primary particle energy is identical. Apart from these similarities, there are of course some differences: The frequency dependence in the Allan-formula is specified as ν^{-1}. This is obviously very different from the exponential decay in our parametrisation. However, the extrapolated frequency dependence for the Allan-formula rests on rather sparse and uncertain data, some of which lie in the incoherent regime not included in our parametrisation. The dependence on shower zenith angle is much more complex than a simple $\cos(\theta)$ trend in our parametrisation and is therefore difficult to compare with the Allan-formula. Furthermore, we do not predict any significant dependence of the total field strength on the angle between shower axis and magnetic field (denoted α in the Allan-formula). If, however, one looks only at a certain polarisation component, this could well introduce a $\sin\alpha$-dependence, e.g. on the azimuth angle to the magnetic field (cf. eq. (4.3)).

Overall, our parametrisation shows many similarities to the historic Allan-parametrisation. The discrepancies, e.g. regarding the frequency dependence, are significant, but considering the sparse experimental data on which the Allan-formula is founded, these discrepancies should not be over-interpreted. In this context one should also remember that later experiments measured significantly lower values for ϵ_ν, a discrepancy that is yet unsolved, but most probably due to calibration issues.

On the one hand, we therefore urgently need new, reliable, well-calibrated experimental data. On the other hand, the modelling efforts have to continue. In particular, we will improve our simulation by basing it on a more realistic air shower model as given by the CORSIKA code. This will automatically resolve the two major shortcomings of our current model: an unrealistic particle pitch-angle distribution and the assumption of a totally homogeneous air shower development. Taking into account these effects most likely will redistribute flux in such a way that the emission levels in the centre region become smaller, making them more consistent with the historical data.

4.7 Discussion

Our analysis of the Monte Carlo simulation results with regard to the underlying air shower parameters for the first time establishes a number of experimentally relevant features of the radio emission.

One major result is the predicted polarisation characteristics of the emis-

sion generated in the geomagnetic emission scenario. With this knowledge, polarisation-sensitive experiments should be able to directly verify that a major part of the radio emission indeed stems from the geomagnetic mechanism. The overall weak intrinsic asymmetries in the emission pattern (except for those associated to projection effects) on the other hand make experimental setups measuring only the total field strength or one circular polarisation component seem less desirable.

Another important insight is provided by the effects arising in air showers with high zenith angles. The intrinsic broadening of the emission pattern associated to the increasing distance of the air shower maximum in combination with projection effects and a flattening of the spectral dependence makes highly inclined air showers an especially interesting target for detection with radio techniques.

Other useful results of our simulations are the predicted wavefront curvature (useful for beam-forming procedures in phased arrays and indeed confirmed by LOPES-measurements), the expected quasi-linear scaling of the field strengths in the coherent regime, the very weak dependence of the total field strength on the specific geomagnetic field geometry and strength and the changes to the radial dependence as a function of changing depth of shower maximum.

The successful incorporation of a significant number of air shower and observer parameters into a single parametrisation as achieved in this work demonstrates that the emission is overall "well-behaved" and yields a well-interpretable signal. As a solid estimate, the parametrisation can be a useful tool for the interpretation of experimental data and the planning of experimental setups. Additionally, there are remarkable similarities between the parametrisation of our Monte Carlo results and the historic Allan-formula.

Our current results represent the most sophisticated simulation of radio emission from cosmic ray air showers carried out to date. In the future, we will switch from analytic parametrisations of air shower characteristics as the basis of our simulations to a full-fledged air shower model based on the CORSIKA simulation code, further improving the modelling accuracy.

4.8 Conclusions

This work presents the cumulative result of our major effort at a realistic modelling of the radio emission from cosmic ray air showers in the scheme of coherent geosynchrotron radiation. For the first time, we now have a solid understanding and a quantitative description of the important emission character-

istics and their dependences on important air shower and observer parameters. In particular, the emission pattern, spectral dependence, polarisation characteristics, primary particle energy dependence, magnetic field dependence and the dependence on air shower geometry and depth of shower maximum for geosynchrotron emission are now theoretically determined. This information is imperative for the interpretation and planning of concrete experiments. In the near future, on the other hand, experiments such as LOPES will provide well-calibrated, reliable data that will allow a direct comparison with our theoretical predictions for the first time. A direct verification of the geomagnetic emission mechanism will then be possible.

Having reached this important milestone in the modelling of radio emission from cosmic ray air showers, the next step will be an interfacing of our code to CORSIKA (Heck et al. 1998), delivering a full-fledged realistic Monte Carlo simulation of radio emission from cosmic ray air showers. Additionally, we will incorporate further possible emission mechanisms such as Askaryan-type Čerenkov radiation in our model.

5

Conclusions

We have performed a detailed analysis of radio emission from cosmic ray air showers in the scheme of coherent geosynchrotron radiation. The properties of the radiation generated by the geomagnetic emission mechanism — which is assumed to be dominant — have been established with unprecedented accuracy. Our analysis has been performed in three steps.

First, we have carried out an analytic calculation of the radio emission from an average vertical 10^{17} eV air shower (chapter 2). The air shower itself has been modelled using a set of analytic parametrisations, taking into account the most important shower properties such as longitudinal and lateral particle distributions, the particle energy distribution and a simplified integration over the air shower evolution as a whole. The geosynchrotron emission has been calculated in the frequency domain, based on well-known synchrotron theory. While this approach has only limited precision, it allows to gain a solid understanding of the coherence effects arising from the different physical scales present in the air shower. Our model has predicted the radial and spectral dependences of the radio emission and identified the major effects shaping the emission. The spectral dependence is mostly governed by the coherence effects associated with the longitudinal particle distributions, whereas the radial emission dependence is dominated by the intrinsic beaming of the geosynchrotron emission in combination with coherence effects arising from the lateral structure of the air shower and the integration over the shower as a whole. The predicted emission strengths are consistent with the (sparsely) available experimental data and should be high enough for LOPES to easily measure 10^{17} eV air showers.

After having gained a solid understanding of the important effects shaping the emission, we have continued our modelling with the conception and implementation of a sophisticated Monte Carlo simulation (chapter 3). To retain comparability with the analytic results, our Monte Carlo model has been based on the same analytically parametrised air shower model as used in the analytic calculations. The Monte Carlo technique, however, allows a much more precise integration of the radio emission from the totality of the particles in the air shower. In particular, no far-field approximations had to be applied, the full polarisation characteristics of the emission are retained, the full 2-d emission pattern on the ground can be calculated and the integration over the air shower evolution as a whole has been incorporated in a sophisticated way. Additionally, track length effects that could not be taken into account in the analytical calculations, have been treated with great care. Their inclusion has led to the important insight that the total field strength emission pattern is indeed remarkably symmetrical in spite of the asymmetry introduced by the geomagnetic field. It is therefore necessary to measure polarisation data in order to verify the geomagnetic origin of the emission. Apart from having demonstrated and thoroughly tested the concepts envisaged to allow the calculation of the radio emission with high precision on standard PC hardware, we have compared the Monte Carlo results directly with the earlier analytical calculations of a vertical 10^{17} eV air shower. Overall, the agreement is very good, with a mild systematic deviation originating from the treatment of trajectories as always symmetric in the analytical model. In particular, the emission strengths are still at levels that should allow easy detection with LOPES. As the time-domain Monte Carlo simulation pursues a very different approach than the frequency-domain analytical calculations, the good agreement between the two methods gives us solid confidence in our calculations.

Having demonstrated the correctness and robustness of our Monte Carlo code, we have then performed extensive simulations of a huge set of air showers in order to establish the radio emission's dependence on the air shower geometry and specific air shower parameters such as the primary particle energy, the depth of the air shower maximum and the magnetic field configuration (chapter 4). Major results are the predicted polarisation characteristics, the intrinsic broadening of the emission pattern as a function of zenith angle due to the increasing distance of the shower maximum and the confirmation of a quasi-linear scaling of the emission strength with primary particle energy. Apart from a qualitative discussion of these and other important effects, we have successfully incorporated the analysed dependences into an overall

parametrisation. This easy-to-use formula will facilitate the comparison of experimental data and theoretically predicted emission properties significantly. Furthermore, it allows for the first time to relate important air shower parameters directly to specific characteristics of the radio emission. The parametrisation summarises the cumulative modelling effort performed in this thesis and thus represents a very useful tool for the study of radio emission from cosmic ray air showers.

In the course of this thesis, we have built a solid theoretical foundation for the interpretation of current and future experimental data of radio emission from cosmic ray air showers. The next interesting step will be to directly compare the theoretical predictions with experimental data, especially regarding the polarisation characteristics, which allow a direct verification of the geomagnetic emission mechanism. Additionally, our model constitutes a solid basis for further development. In particular, we will substitute the air shower model based on analytic parametrisations with an interfacing to the air shower simulation code CORSIKA, yielding a full-fledged Monte Carlo simulation of radio emission from cosmic ray air showers. Furthermore, we will include additional emission mechanisms such as Askaryan-type Čerenkov radiation in our model.

With these advances in the theoretical modelling of the emission and upcoming results from experimental projects such as LOPES, radio emission from cosmic ray air showers thus has made great advances on the way towards being established as an additional observing technique for cosmic ray research.

List of Figures

List of Tables

Bibliography

Abu-Zayyad, T., Belov, K., Bird, D. J., et al. 2001, Astropart. Physics, 16, 1

Agnetta, G., Ambrosio, M., Aramo, C., et al. 1997, Astropart. Physics, 6, 301

Aharonian, F. A., Akhperjanian, A. G., Aye, K.-M., et al. 2004, Nature, 432, 75

Alkhofer, O. C. 1975, Introduction to cosmic radiation (Verlag Carl Thiemig München)

Allan, H. R. 1971, Prog. in Element. part. and Cos. Ray Phys., Vol. 10, 171

Allan, H. R., Clay, R. W., & Jones, J. K. 1970, Nature, 227, 1116

Allan, H. R., Clay, R. W., Jones, J. K., Abrosimov, A. T., & Neat, K. P. 1969, Nature, 222, 635

Allan, H. R., Jones, J. K., Mandolesi, N., Prah, J. H., & Shutie, P. F. 1971, in Proc. of the Twelfth Intern. Cosmic Ray Conf., Hobart, Vol. 3, 1102

Allan, H. R., Neat, K. P., & Jones, J. K. 1967, Nature, 215, 267

Allan, H. R., Shutie, P. F., Sun, M. P., & Jones, J. K. 1973, in Proc. Thirteenth Intern. Cosmic Ray Conf., Denver, Vol. 4, 2407

Allan, H. R., Sun, M. P., & Jones, J. K. 1975, in Proc. Fourteenth Intern. Cosmic Ray Conf., München, Vol. 8, 3082

Aloisio, R. & Blasi, P. 2002, Astropart. Physics, 18, 183, astro-ph/0201310

Alvarez-Muñiz, J., Vázquez, R. A., & Zas, E. 2000, Phys. Rev. D, 62, 63001

ANTARES collaboration. 1999, A Deep Sea Telescope for High Energy Neutrinos, Tech. rep., astro-ph/9907432

Antoni, T., Apel, W. D., Badea, F., et al. 2003, Nucl. Instr. Meth., 513, 490

Antoni, T., Apel, W. D., Badea, F., et al. 2001, Astropart. Physics, 14, 245

Askaryan, G. A. 1962, Soviet Phys. JETP, 14, 441

Askaryan, G. A. 1965, Soviet Phys. JETP, 21, 658

Atrashkevich, V. B., Vedeneev, O. V., Allan, H. R., et al. 1978, Sov. J. Nucl. Phys., 28, 366

Atrashkevich, V. B., Vedeneev, O. V., & Khristiansen, G. B. 1975, in Proc. Fourteenth Intern. Cosmic Ray Conf., München, Vol. 8, 3086

Auger, P., Ehrenfest, P., Maze, R., Daudin, J., & Fréon, R. A. 1939, Reviews of Modern Physics, 11, 288

Balkanov, V. A., Belolaptikov, I. A., Bezrukov, L. B., et al. 1999, in Dark matter in Astrophysics and Particle Physics, 805–+

Belletoile, A., Ardouin, D., Charrier, D., et al. 2004, in Proc. of the SF2A 2004, astro-ph/0409039

Bergman, D.R. for the High Resolution Fly's Eye Collaboration. 2003, in Proceedings of the 28th ICRC, Tsukuba, Japan, ed. T. Kajita, Y. Asaoka, A. Kawachi, Y. Matsubara, & M. Sasaki, Vol. 1 (Universal Academy Press, Inc. - Tokyo, Japan), 397

Biermann, P. L. & Strittmatter, P. A. 1987, ApJ, 322, 643

Bird, D. J., Corbato, S. C., Dai, H. Y., et al. 1995, ApJ, 441, 144

Buniy, R. V. & Ralston, J. P. 2002, Phys. Rev. D, 65, 16003

Bury, K. V. 1975, Statistical Models in Applied Science (John Wiley & Sons, New York), 299

Castagnoli, C., Silvestro, G., Picchi, P., & Verri, G. 1969, Nuovo Cimento, 63B, 373

Catalano, O., Maccarone, M. C., Santangelo, A., Scarsi, L., & The Euso Collaboration. 2003, in Astronomy, Cosmology and Fundamental Physics, 427–+

Cheng, K. S., Ho, C., & Ruderman, M. 1986, ApJ, 300, 500

Colgate, S. A. 1967, J. Geophys. Res., 72, 4869

Dova, M. T., Epele, L. N., & Mariazzi, A. G. 2003, Astropart. Physics, 18, 351

Dova, M. T., Fanchiotti, H., Garcia-Canal, C., et al. 1999, in Proceedings of the 26th ICRC, Utah, USA, ed. D. Kieda, M. Salamon, & B. Dingus, Vol. 1, 514

Elbert, J. W. & Sommers, P. 1995, ApJ, 441, 151

Erlykin, A. & Wolfendale, A. 1987, J. Phys. G: Nuclear and Particle Physics, 23, 979

Falcke, H. & Gorham, P. W. 2003, Astropart. Physics, 19, 477

Fermi, E. 1949, Physical Review, 75, 1169

Fog, A. 2003, http://www.agner.org/random/randomc.htm

Fuji, M. & Nishimura, J. 1969, in Proc. 11th Internat. Conf. on Cosmic Rays, Budapest, Vol. 3, 709

Gaisser, T. K. 1990, Cosmic Rays and Particle Physics (University Press, Cambridge)

Gousset, T., Ravel, O., & Roy, C. 2004, in , astro-ph/0402426

Green, K., Rosner, J. L., Suprun, D. A., & Wilkerson, J. F. 2003, Nucl. Instr. Meth., 498, 256, astro-ph/0205046

Greisen, K. 1956, Prog. Cosmic Ray Phys., Vol. 3, 1

Greisen, K. 1960, Ann. Rev. Nucl. Sci., Vol. 10, 63

Greisen, K. 1966, Phys. Rev. Lett., 16, 748

Halzen, F. 1999, New Astron. Rev., 42, 289

Harding, A. K. & Gaisser, T. K. 1990, ApJ, 358, 561

Heck, D., Knapp, J., Capdevielle, J. N., Schatz, G., & Thouw, T. 1998, Forschungszentrum Karlsruhe Report FZKA 6019

Hess, V. F. 1912, Z. Phys., 13, 1084

Horneffer, A., Antoni, T., Apel, W. D., et al. 2004, in Astronomical Telescopes and Instrumentation 2004: Gravitational Wave and Particle Astrophysics Detectors, Proceedings of the SPIE, Vol. 5500, 129

Horneffer, A., Falcke, H., Haungs, A., et al. 2003, in Proceedings of the 28th ICRC, Tsukuba, Japan, ed. T. Kajita, Y. Asaoka, A. Kawachi, Y. Matsubara, & M. Sasaki, Vol. 2 (Universal Academy Press, Inc. - Tokyo, Japan), 969

Huege, T. & Falcke, H. 2002, in Proceedings of the 6th European VLBI Network Symposium, ed. P. R. Z. J. Ros, E., MPIfR Bonn, Germany, 25

Huege, T. & Falcke, H. 2003, A&A, 412, 19

Huege, T. & Falcke, H. 2004a, A&A, in press

Huege, T. & Falcke, H. 2004b, Astropart. Phys., in preparation

Jackson, J. D. 1975, Classical Electrodynamics, 2nd edn. (John Wiley & Sons, New York)

Jelley, J. V., Fruin, J. H., Porter, N. A., et al. 1965, Nature, 205, 327

Kahn, F. D. & Lerche, I. 1966, in Proc. Roy. Soc., Vol. A-289, 206

Kamata, K. & Nishimura, J. 1958, Prog. Theoret. Phys. Suppl., Vol. 6, 93

Kampert, K.-H., Antoni, T., Apel, W. D., et al. 2004, in Proceedings of the Cosmic Ray International Seminar 2004: GZK and Surroundings, to be published, astro-ph/0410559

Knapp, J., Heck, D., Sciutto, S. J., Dova, M. T., & Risse, M. 2003, Astropart. Physics, 19, 77, astro-ph/0206414

Kravchenko, I., Frichter, G. M., Seckel, D., et al. 2003, Astroparticle Physics, 19, 15

Kulikov, G. V. & Khristiansen, G. B. 1959, Soviet Phys. JETP, 35, 441

Lagage, P. O. & Cesarsky, C. J. 1983, A&A, 118, 223

Linsley, J. 1986, J. Phys. G: Nucl. Phys., 12, 51

Maier, G. 2003, PhD thesis, Universität Karlsruhe

Matsumoto, M. & Nishimura, T. 1998, ACM Trans. on Modeling and Computer Simulation, Vol. 8, No. 1, 3

Matthews, J. & Pierre Auger Observatory Collaboration. 2004, AAS/High Energy Astrophysics Division, 8

Nerling, F., Engel, R., Guerard, C., Perrone, L., & Risse, M. 2003, in Proceedings of the 28th ICRC, Tsukuba, Japan, ed. T. Kajita, Y. Asaoka, A. Kawachi, Y. Matsubara, & M. Sasaki, Vol. 2 (Universal Academy Press, Inc. - Tokyo, Japan), 611

Nikolsky, S. I. 1995, Nucl. Phys. B. (Proc. Suppl.), 39, 228

Prah, J. H. 1971, Master's thesis, University of London

Pryke, C. L. 2001, Astropart. Physics, 14, 319

Ptuskin, V. S., Rogovaya, S. I., Zirakashvili, V. N., et al. 1993, A&A, 268, 726

Rachen, J. P. & Biermann, P. L. 1993, A&A, 272, 161

Rohlfs, K. & Wilson, T. L. 1996, Tools of Radio Astronomy, 2nd edn. (Springer Verlag, Berlin)

Röttgering, H., de Bruyn, A. G., Fender, R. P., et al. 2003, in Texas in Tuscany. XXI Symposium on Relativistic Astrophysics, 69–76

Rybicki, G. B. & Lightman, A. P. 1979, Radiative Processes in Astrophysics (John Wiley & Sons, New York), 167–194

Saltzberg, D., Gorham, P., Walz, D., et al. 2001, Physical Review Letters, 86, 2802

Sciutto, S. J. 1999, astro-ph/9911331, see also http://www.fisica.unlp.edu.ar/auger/aires

Shaviv, N. J. 2004, in Proceedings of the 19th European Cosmic Ray Symposium, in preparation

Sigl, G. 2003, Annals Phys., 303, 117

Sigl, G., Schramm, D. N., & Bhattacharjee, P. 1994, Astroparticle Physics, 2, 401

Sokolsky, P. 2003, in Particle Astrophysics Instrumentation. Edited by Peter W. Gorham. Proceedings of the SPIE, Volume 4858, pp. 103-114 (2003)., 103–114

Spencer, R. E. 1969, Nature, 222, 460

Sun, M. P. 1975, PhD thesis, University of London

Suprun, D. A., Gorham, P. W., & Rosner, J. L. 2003, Astropart. Physics, 20, 157

Takeda, M., Hayashida, N., Honda, K., et al. 1999, ApJ, 522, 225

The AGASA collaboration. 2004, http://www-akeno.icrr.u-tokyo.ac.jp/AGASA

The Pierre Auger Collaboration. 1996, The Pierre Auger Project Design Report, http://www.auger.org

Ulrich, H. 1997, Diploma thesis, Universität Karlsruhe

Ulrich, H. 2003, PhD thesis, Universität Karlsruhe

Watson, G. N. 1944, Theory of Bessel Functions (University Press, Cambridge)

Wefel, J. P. 1991, in NATO ASIC Proc. 337: Cosmic Rays, Supernovae and the Interstellar Medium, 29–+

Zas, E., Halzen, F., & Stanev, T. 1992, Phys. Rev. D, 45, 362

Zatsepin, G. & Kuzmin, V. 1966, Zh. Eksp. Teor. Fiz., 4, 114

6

Danksagung

Eine Doktorarbeit ohne die Hilfe und Unterstützung Anderer zu schreiben, dürfte geradezu unmöglich sein. Auch an meiner Dissertation haben viele Menschen Anteil gehabt.

Besonderer Dank gebührt meinem Betreuer Heino Falcke, der mein Interesse für die Forschung am MPIfR bereits vor Beginn meines Master-Studiums in Cambridge weckte. Er gab mir mit diesem spannenden Promotionsthema eine einmalige Chance. Ohne die vielen Diskussionen, für die er sich immer Zeit nahm, ohne seine Ratschläge und die Motivation, die seine Begeisterung immer wieder in mir weckte, hätte ich diese Dissertation so nicht fertigstellen können. Meinem Koreferenten Peter Schneider möchte ich für seine Hilfe und seine vielen Ideen, die mir oft neue Lösungsansätze aufzeigten, ebenfalls sehr herzlich danken.

Trotz seiner vielfältigen Verpflichtungen als geschäftsführender Direktor des MPIfR verfolgte und begleitete Anton Zensus meine Arbeit und meine Zukunftsplanung immer mit großem Interesse. Dies habe ich immer sehr zu schätzen gewusst. Auch Arno Witzel hatte stets ein offenes Ohr für meine Belange und half mir beim Umschiffen diverser Klippen. Die Unterstützung durch die International Max-Planck Research School (IMPRS) gab mir die Möglichkeit des Besuchs von Konferenzen und Sommerschulen, die mir einen “Blick über den Tellerrand” erlaubten und mir ermöglichten, wichtige Kontakte zu knüpfen.

Die freundliche Atmosphäre in der VLBI-Gruppe trug entscheidend dazu bei, daß mir meine Arbeit trotz der obligatorischen Tiefs immer Freude machte. Von den Mitarbeitern des MPIfR möchte ich besonders Thomas

Beckert hervorheben, der mir maßgeblich bei der Einarbeitung in die Theorie der Synchrotronstrahlung half und auch bei späteren Problemen immer ein wertvoller Ansprechpartner war. Auch Peter Biermann verfolgte meine Arbeit mit besonderem Interesse und machte darüber hinaus unermüdlich Werbung für meine Ergebnisse. Daneben gab es natürlich viele Menschen ausserhalb des MPIfR, die mir in Diskussionen, mit Ratschlägen oder sonstiger fachlicher Unterstützung geholfen haben. Besonders hervorheben möchte ich hier John Ralston, Ralph Engel und Andreas Haungs.

Ohne die vielen Studenten der VLBI-Gruppe wäre die tägliche Arbeit sicher langweilig gewesen. Ich hatte mit Andreas Brunthaler, Elmar Körding und Andreas Horneffer über die Jahre viel Spaß in unserem Büro. Darüber hinaus haben mir alle drei oft beim Lösen kleinerer und grösserer Probleme sehr geholfen. Ganz besonders möchte ich Elmar dafür danken, daß er immer dazu bereit war, mit mir über knifflige Probleme zu diskutieren — das hat mich wirklich oft entscheidend weitergebracht. Das tägliche Mitagessen mit Uwe Bach und Enno Middelberg, bei dem wir zusammen die kulinarischen Köstlichkeiten unserer damaligen Kantine genossen, war ebenfalls immer ein Highlight.

Martin Stumpe werde ich zum Dank dafuer, daß er meine Arbeit Korrektur gelesen hat und auch sonst immer ein wirklich guter Freund war, bei einem Computerspiel seiner Wahl einmalig gewinnen lassen. Meinen Eltern und meinen Brüdern danke ich für ihre bedingungslose Unterstützung und dafür, daß sie immer für mich da waren. Ganz besonders bedanken möchte ich mich bei Kathrin, die mein Leben und mein Studium über so viele Jahre bereichert und begleitet hat.

Zu guter Letzt danke ich meiner Freundin Tatjana, die für mich ein ganz besonderer Mensch ist und mit ihrer unbändigen Lebensfreude auch mein Leben mit so viel Freude und Zuversicht erfüllt.

Publications

The contents of this thesis have been published in the following refereed journal articles:

- Chapter 2: *"Radio emission from cosmic ray air showers: Coherent geosynchrotron radiation"*
  Huege, T., Falcke, H., 2003, A&A 412, 19–34
- Chapter 3: *"Radio emission from cosmic ray air showers: Monte Carlo simulations"*
  Huege, T., Falcke, H., 2004, A&A in press, astro-ph/0904223
- Chapter 4: *"Radio emission from cosmic ray air showers: Simulation results"*
  Huege, T., Falcke, H., Astropart. Physics, in preparation